Collectivity in Ti isotopes towards $N = 40$
中性子数 **40** 近傍の **Ti** 同位体における集団性の変遷

Asahi Kohda
甲田 旭

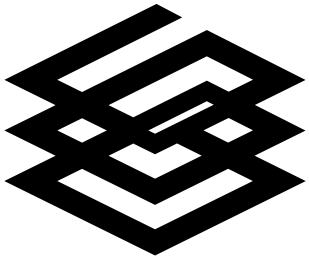

Doctoral Dissertation

Experimental Nuclear Physics Division,
Research Center for Nuclear Physics, The University of Osaka

大阪大学核物理研究センター 核物理実験研究部門

September 5, 2025

令和 7 年 9 月 5 日

Abstract

We aimed to discuss the evolution of collectivity in Ti isotopes toward $N = 40$. To this end, we studied the isotopes ^{56}Ti and ^{58}Ti by Coulomb excitation from the ground 0^+ state to the first 2^+ excited state, in order to investigate the possible magicity at $N = 40$. The neutron number $N = 40$ is a magic number for the harmonic oscillator potential. In real nuclei, however, this shell closure is weakened due to spin-orbit interactions, and the degree of magicity depends on the proton number. In ^{68}Ni ($Z = 28$, $N = 40$), where protons fill the $f_{7/2}$ orbital, collectivity is reduced compared to its neighbors and exhibiting the characteristics of a magic nucleus. As proton number decreases along $N = 40$, collectivity increases from ^{68}Ni to ^{66}Fe and $^{64}_{24}Cr_{40}$, located in the center of the $f_{7/2}$ shell, large deformation appears. As the proton number decreases further toward the next magic number $Z = 20$, it is important to clarify whether magic-like behavior emerges. Some theoretical models predict that such a magic-like nature may indeed appear. Other models suggest that the collectivity would remain low even at $Z = 20$, since the shell gap responsible for the reduced collectivity in ^{68}Ni is already diminished around $Z = 24$. This contrast highlights the significance of studying nuclei near ^{60}Ca. Since experiments on ^{60}Ca, which lies far from the stability line, are challenging, this study focuses on the neighboring Ti isotopes to investigate changes in the magicity of $N = 40$ in the neutron-rich region through Coulomb excitation experiments of ^{56}Ti and ^{58}Ti.

The experiment was performed at the RI Beam Factory at the RIKEN Nishina Center. Coulomb excitation was performed by irradiating a gold (^{197}Au) target with high-intensity ^{56}Ti and ^{58}Ti beams obtained at the RI beamline BigRIPS. The final state was identified by measuring the de-excitation gamma rays in coincidence with the outgoing particles using the ZeroDegree Spectrometer. The gamma rays were observed using the HiCARI array, consisting of 12 Ge detectors with 39 crystals, including a gamma-ray tracking detector developed at RCNP. This detector uses waveform analysis to accurately determine the incident position, enabling precise determination of the reaction point of the gamma ray and high-resolution Doppler

shift correction. The reduced electric quadrupole transition probabilities B(E2) were determined from the Coulomb excitation cross sections. The values were found to be 12.6 (15) and 10.3 (18) [W.u.] for ^{56}Ti and ^{58}Ti, respectively. These values serve as direct indicators of nuclear collectivity. Comparing these results with shell model calculations, it is suggested that excitations beyond the shell gap of $N = 40$ are likely to occur in Ti isotopes, and that the magicity is weak.

Contents

Chapter 1

Scientific Background

The structure of atomic nuclei is strongly influenced by the numbers of protons and neutrons they contain, with certain "magic numbers" leading to particularly stable configurations. These magic numbers manifest themselves in characteristic excitation energies and reduced collectivity. In nuclei with the semi-magic neutron number $N = 40$, the structure changes very sensitively with the proton number Z. For example, ^{68}Ni, which has 28 (magic number) protons, has a higher first 2^+ energy than neighboring isotopes and exhibits magic-like characteristics. This behavior has been accurately reproduced by several theoretical models. However, predictions differ for nuclei below $Z = 22$, where experimental data are not yet available, so there is a need to perform experiments to clarify the nuclear structure in this region.

1.1 Shell model and magic numbers

1.1.1 Magic numbers

It is well known that the structure of atomic nuclei plays a crucial role in their stability. In particular, nucleons (protons and neutrons) tend to occupy discrete energy levels, forming shell structures. A nucleus is especially stable when the number of protons Z or neutrons N corresponds to fully filled shells; these numbers, known as “magic numbers,” are 2, 8, 20, 28, 50, 82, or 126.[*1)] The enhanced stability associated with these magic numbers is supported primarily by the following measurements:

(i) Neutron or proton separation energy

(ii) Energy of the first 2^+ excited level in even-even nuclei

[*1)] Some people claim “6” is also a magic number, but we won’t discuss it here.

(iii) Excitation level density

(iv) Number and abundance of stable isotopes

As an example, Fig. 1.1 shows even-even nuclei whose first 2^+ excitation energy, $E(2_1^+)$, is higher than that of its surrounding nuclei. In fact, they are found to be abundant where the proton or neutron numbers are magic numbers.

In stable nuclei, these features generally appear at fixed magic numbers (2, 8, 20$\cdots$) with few exceptions. However, as experimental techniques for short-lived unstable nuclei have been developed, it was found that some conventional magic numbers disappear in neutron-rich nuclei, such as ^{32}Mg with $N = 20$ [1]. This observation led to the identification of new magic numbers, $N = 16$ and 34 [2, 3], showing that the traditional understanding of magic numbers is not universally valid.

These changes are interpreted as a gradual evolution of the nuclear shell structure —that is, the arrangement and energy spacing of single-particle orbitals—as one moves away from stability, which can alter the number of nucleons forming closed shells [4].

We now briefly review the shell model, which successfully accounts for the traditional magic numbers.

1.1.2 Shell model

The shell model is a theoretical framework in nuclear physics that describes the structure of the nucleus by assuming that nucleons occupy discrete energy levels,

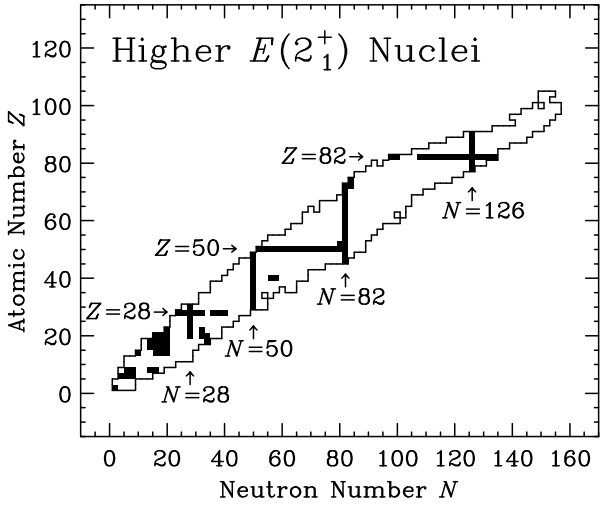

Figure 1.1: Nuclei whose first 2^+ excitation energy satisfies $E(2_1^+) > 7/\sqrt{Z}$ MeV in even-even nuclei are represented by ■. The reason is that the larger the Z, the smaller the $E(2_1^+)$ tends to be. We multiply $E(2_1^+)$ by $\sqrt{Z}$ to compensate for the general trend and highlight the magic numbers. We can see that there are many nuclei with high $E(2_1^+)$ at the magic numbers 28, 50, 82, and 126.

called shells, similar to electrons in atoms, and was described by Mayer and Jensen in 1949 [5–10]. They were awarded the Nobel Prize in Physics in 1963 for their work on the nuclear shell model.

In reality, nucleons interact strongly with each other through the nuclear force. However, the shell model approximates these interactions by assuming that each nucleon moves independently in an average potential created by all other nucleons. This is known as the independent-particle approximation.

Each orbital can fill a specific number of nucleons, determined by its quantum numbers, and when the maximum number of particles is filled into a "shell" consisting of multiple orbitals with similar energy levels, it is called a "closed shell". The number of nucleons that form a closed shell, the total number corresponds to a magic number, which represents particularly stable configurations.

So how is the number of nucleons that form a closed shell determined? It is determined by the one-body potential mentioned earlier. In conclusion, it is known that by adopting a Woods-Saxon type potential that incorporates the effect of spin-orbit coupling interactions, it is possible to reproduce the actual magic numbers 2, 8, 20...

The reason why the shell structure with magic numbers emerges can be understood by solving the Schrödinger equation for nucleons moving inside the nucleus. First, the Schrödinger equation in three-dimensional space that depends only on the central force potential $V(r)$ is :

$$\left\{-\frac{\hbar^2}{2M}\nabla^2 + V(r)\right\}\psi(r) = E\psi(r) \tag{1.1}$$

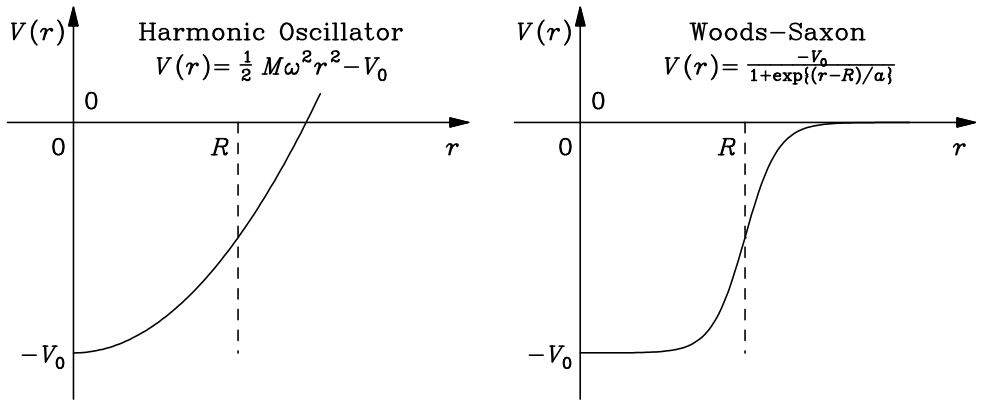

Figure 1.2: Overview of harmonic oscillator and Woods-Saxon potentials.

Now, if $V(r)$ is a three-dimensional Woods-Saxon potential, then :

$$V(r) = \frac{-V_0}{1 + \exp\{(r - R)/a\}} \tag{1.2}$$

Here, R is the radius of the nucleus, and a is a diffuseness parameter. The shape of this potential is shown on the right side of Figure 1.2.

The Woods-Saxon potential shown here best reproduces the experimental results, but it cannot be solved analytically and requires numerical calculations using a computer. However, the Woods–Saxon potential cannot be solved analytically and requires numerical calculations. To illustrate the basic structure of single-particle levels in a transparent way, we instead adopt a three-dimensional harmonic oscillator potential,

$$V(r) = \frac{1}{2}M\omega^2 r^2 - V_0 \tag{1.3}$$

which allows an analytical solution. Although this potential is only a rough approximation of the nuclear mean field, it is particularly useful for light nuclei where surface effects are relatively small, and serves as a pedagogical model to explain how magic numbers such as 2, 8, and 20 arise.

Substituting (1.3) into (1.1), expressing $\psi(r)$ as the product of the radial wave function $R_{n\ell}(r)$ and the spherical harmonic function $Y_{\ell m}(\theta, \phi)$, and separating each into two equations and solving them, we obtain the energy eigenvalue $E_{n\ell}$:[*1)]

$$E_{n\ell} = -V_0 + \frac{3}{2}\hbar\omega + \{2(n - 1) + \ell\}\hbar\omega \tag{1.4}$$

Here, $n = 0, 1, 2, \ldots$ is the harmonic oscillator quantum number, which counts the number of radial nodes (sometimes referred to as a principal quantum number in the harmonic oscillator case), and the orbital angular momentum quantum number is $\ell = 0, 1, 2, \ldots$. By defining $N = 2n + \ell$, N is always a non-negative integer. Therefore, the energy levels appear at equal intervals of $\hbar\omega$.

Here, if $N = 2$ or greater, there are two or more possible combinations of n, ℓ. Using the conventional spectroscopic notation for ℓ (s, p, d, f, g, h, i, ...), the combination for $N = 0$ is $n\ell = 1$s, and for $N = 1$ it is $n\ell = 1$p, each of which has only one possible configuration. In contrast, for $N = 2$ there are multiple possible combinations, such as $n\ell = 1$d or $n\ell = 2$s.

How many nucleons can be filled into each level depends on the degeneracy of the

[*1)] See section 5.1.2 in the textbook [11].

orbital characterized by ℓ. For a given orbital angular momentum quantum number ℓ, the magnetic quantum number m can take $2\ell + 1$ values, corresponding to the possible orientations of the orbital angular momentum. Including the two possible spin states for each m, the maximum number of nucleons that can occupy a single orbital with angular momentum ℓ is therefore $2(2\ell + 1)$.

Taking this into consideration, $N = 0$ has 2 nucleons in the 1s orbital, $N = 1$ has 6 nucleons in the 1p orbital, $N = 2$ has 12 nucleons in total in the 1d and 2s orbitals... When nucleons are filled successively from the lowest level, once the numbers 2, 8, 20, $\cdots$ are reached, the filling continues into the next shell. These numbers 2, 8, and 20 correspond to magic numbers. However, in this model, the number after 20 is not 28 but 40. Although 40 is not generally considered a magic number, it plays a special role in nuclear structure and is often referred to as a "semi-magic number" in this study.

Next, to express "general" magic numbers such as 28 and 50, it is necessary to introduce the spin-orbit coupling potential:

$$V_{\mathrm{so}} = v(r)\, \boldsymbol{\ell} \cdot \boldsymbol{s} \tag{1.5}$$

Here, $\boldsymbol{s}$ denotes the intrinsic spin angular momentum of the nucleon, with magnitude $|\boldsymbol{s}| = 1/2$. The operator $\boldsymbol{\ell} \cdot \boldsymbol{s}$ takes different expectation values depending on whether $\boldsymbol{s}$ is parallel or antiparallel to $\boldsymbol{\ell}$, leading to a positive or negative contribution to the potential energy. The difference between these two cases can be expressed as

$$\Delta V_{\mathrm{so}} = \frac{1}{2} v(r)(2\ell + 1) \tag{1.6}$$

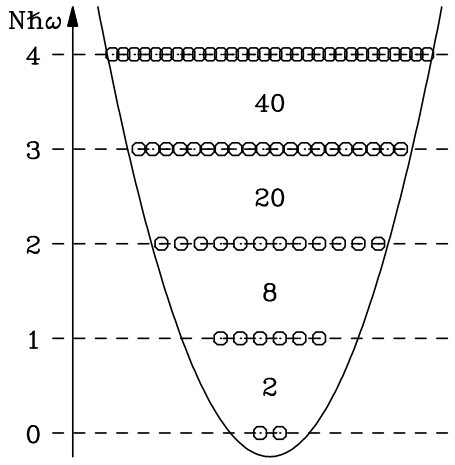

Figure 1.3: In a model using a three-dimensional harmonic oscillator potential, the magic numbers arising from the shell gaps are 2, 8, 20, 40, ...

and the larger ℓ, the wider it becomes. In addition, if we define the total angular momentum $\boldsymbol{j} = \boldsymbol{\ell} + \boldsymbol{s}$, $j = \ell \pm s$. The plus sign in $j = \ell \pm s$ corresponds to the case where $\boldsymbol{\ell}$ and $\boldsymbol{s}$ are parallel, while the minus sign corresponds to the antiparallel case. When $\ell = 0$, it is always positive because there is no direction of $\boldsymbol{\ell}$. The levels separated by the spin direction are represented as $n\ell_j$, and written as $1s_{1/2}$, $1p_{3/2}$, $1p_{1/2}$ .... For levels with the same $n\ell$, the larger j is the lower energy level. For $\ell = 3(\mathrm{f})$ and above, the energy level difference due to the difference in j becomes large, and the magic numbers 28 and 50 are reproduced. In addition, the $1g_{9/2}$ level at $N = 4$ degenerates to $2p_{1/2}$ at $N = 3$ due to the effect of the spin-orbit coupling potential, and the shell gap at 40, which corresponded to a magic number in the harmonic oscillator, is reduced and is no longer regarded as a magic number.

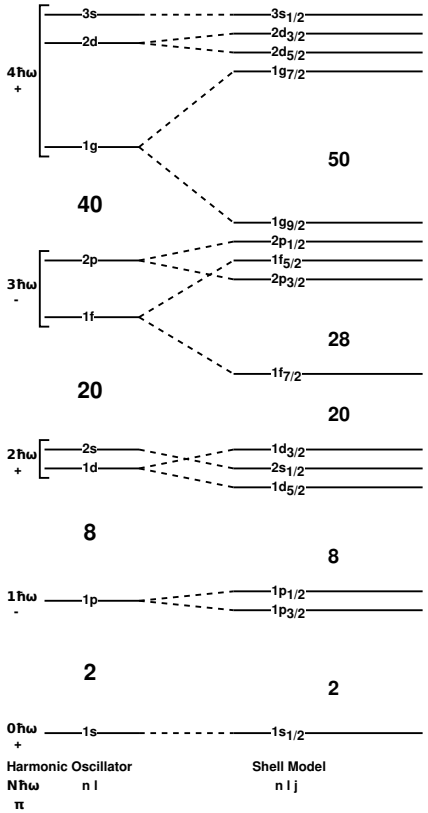

Figure 1.4: Magic numbers in the harmonic oscillator model and shell model (Woods-Saxon type + spin-orbit coupling potential). The magic numbers are the same for 2, 8, and 20 regardless of whether or not there is a spin-orbit coupling potential, but the magic number 40 disappears because the shell gap is narrowed by the effect of spin-orbit coupling. Instead, a new number 28 is created.

1.1.3 Nuclear spin and parity

The total angular momentum (nuclear spin) $\boldsymbol{I}$ of a nucleus is defined as the vector sum of the total angular momenta $\boldsymbol{j}_i = \boldsymbol{\ell}_i + \boldsymbol{s}_i$ of all individual nucleons:

$$\boldsymbol{I} = \sum_{i=1}^{A} \boldsymbol{j}_i, \tag{1.7}$$

where A is the number of nucleons in the nucleus. The magnitude I of $\boldsymbol{I}$ takes integer values (in units of $\hbar$) when A is even, and half-integer values when A is odd.

The parity π of an entire atomic nucleus is determined by the product of the parities associated with the single-particle orbitals occupied by the nucleons. Each orbital contributes a parity that depends on the orbital angular momentum quantum number ℓ, given by $\pi = (-1)^{\ell}$, i.e., positive for even ℓ and negative for odd ℓ.

It is also known that the ground state of a nucleus with an even number of protons and neutrons (even-even nuclei) is always nuclear spin parity $I^{\pi} = 0^{+}$. This is because the pairing interaction of the nuclear force favors configurations in which two nucleons in the same orbital couple with opposite spins. As a result, nucleons tend to form pairs that share the same orbital angular momentum and parity. In contrast, Hund's rules, which govern the electron configuration in atomic structure, specify that the ground state corresponds to the configuration maximizing the total angular momentum. This prescription is opposite to the nuclear case, where repulsive electron–electron forces are replaced by attractive nucleon–nucleon interactions.

1.2 Excited states of atomic nuclei

1.2.1 First 2^{+} excitation level

The first excited state of even-even nuclei is almost always $I^{\pi} = 2^{+}$, where I denotes the nuclear spin and π the parity, with a few exceptions. This is not simply because nuclei are quadrupole deformed; rather, several mechanisms can lead to a 2^{+} first excited state. In nuclei with quadrupole-deformed ground states, the lowest excitation is typically the 2^{+} member of a rotational band. For spherical nuclei, the first 2^{+} state often arises from quadrupole vibrational excitation. In semi-magic nuclei, the first 2^{+} state can be understood as a seniority-2 state, corresponding to the excitation of two nucleons across a shell gap. Thus, the appearance of a 2^{+} first excited state is a common feature of even-even nuclei, but its underlying origin

depends on the nuclear structure.

1.2.2 2_1^+ level and magic numbers

The first 2^+ state (hereafter referred to as the 2_1^+ state) provides important information about nuclear structure, particularly the degree of quadrupole collectivity and the presence of shell closures (magic numbers). In nuclei whose proton or neutron numbers correspond to magic numbers, the quadrupole deformation is nearly zero and the nuclei are essentially spherical. As a result, the excitation energy of the 2_1^+ state generated by quadrupole collective motion is very high. In such cases, the lowest excited level may be dominated by other types of excitation. Thus, the 2_1^+ state serves as an indicator of how small the quadrupole collectivity is, and by examining its energy, one can infer the degree of nuclear deformation and the presence of magic numbers.

1.2.3 Quadrupole deformation and collectivity

So far, we have discussed that quadrupole-deformed nuclei make electric quadrupole collective motion. Collective motion in nuclei arises when an excited level is formed by the coherent superposition of many-nucleon configurations (protons in this case). Collectivity refers to the number of nucleons involved in the excitation. As we will formulate later, nuclei with a large deformation generally exhibit strong collectivity, meaning that many nucleons participate in the excitation. Conversely, if the deformation is small, only a few nucleons are involved, and the excitation can be considered essentially a single-particle excitation rather than a collective motion.

1.2.4 (Aside) Nuclei with first excited level other than 2^+

Although it is not related to the content of this paper, for reference, we will introduce an example of an even-even nucleus whose first excited level is other than 2^+ and the reason why.

In ^{16}O, an alpha cluster structure consisting of four α particles appears in the first excited level, resulting in 0^+ being the first excited state [12]. In addition, in ^{208}Pb, the 3^- produced by the octupole collective motion appears at a lower position, resulting in the first excited state [13]. When there are magic numbers of protons or neutrons (or both), as in these nuclei, the quadrupolar collectivity is very small, so that 2^+ is very high and a level other than 2^+ can be the lowest energy level. In fact, cases where only one type of nucleon (protons or neutrons) has a magic number and the

first excited state is not 2^+ are extremely rare. Examples include ^{72}Ge and possibly ^{68}Ni. These nuclei are considered to exhibit a tendency of double magicity.

1.3 Indicators of quadrupole collectivity – $B(\mathrm{E2})$

1.3.1 What is $B(\mathrm{E2})$?

This value is called the Reduced Electric Quadrupole Transition Probability. Because it is too long, in this thesis we use the commonly used symbol $B(\mathrm{E2})$. This value can be directly measured experimentally and can be used to evaluate the number of nucleons involved in the collective excitation using the Weisskopf unit described below, and is therefore considered to be the most accurate indicator for evaluating collectivity.

1.3.2 Derivation of $B(\mathrm{E2})$ from $2^+ \to 0^+$ transition lifetime

We denote the lifetime[*1)] of the first 2^+ state as $\tau(2^+ \to 0^+)$. The inverse of the lifetime is defined as the transition probability, written as $T(2^+ \to 0^+)$. These relationships can be expressed as the following formula:

$$T(\mathrm{E2}; 2^+ \to 0^+) = \frac{1}{\tau(\mathrm{E2}; 2^+ \to 0^+)} \tag{1.8}$$

The reduced transition probability can be defined not only for decay, but also for photonuclear absorption processes, where the nucleus is excited from 0^+ to 2^+ by absorbing a gamma ray through an E2 transition. In such cases, it is more appropriate to describe the process using the reduced transition probability $B(\mathrm{E2}; 0^+ \to 2^+)$, because the dependence on the photon field (e.g., the E_γ^5 factor) is removed in the definition of $B(\mathrm{E2})$. The relation between the absorption and emission processes is then given by

$$B(\mathrm{E2}; 0^+ \to 2^+) = 5 \times \mathrm{B}(\mathrm{E2}; 2^+ \to 0^+). \tag{1.9}$$

The reduced transition probability excluding the phase-space factor associated with the gamma-ray energy E_γ is defined as $B(\mathrm{E2}; 0^+ \to 2^+)$. Generalizing, the relationship between the transition probability and the reduced transition probability in the case of Eλ transition is [*2)]

$$T(\mathrm{E}\lambda; I_i \to I_f) = \frac{8\pi(\lambda+1)}{\hbar\lambda\{(2\lambda+1)!!\}^2} \left(\frac{E_\gamma}{\hbar c}\right)^{2\lambda+1} B(\mathrm{E}\lambda; I_i \to I_f) \tag{1.10}$$

[*1)] The relationship between lifetime and half-life is $T_{1/2} = \tau \log 2$.

From this, the relationship between $B(\mathrm{E2}; 0^+ \to 2^+)$ and the lifetime $\tau(\mathrm{E2}; 2^+ \to 0^+)$ is

$$\begin{aligned}
\frac{1}{\tau(\mathrm{E2}; 2^+ \to 0^+)} &= \frac{8\pi(2+1)}{2\hbar\{(2\cdot 2+1)!!\}^2}\left(\frac{E_\gamma}{\hbar c}\right)^{2\cdot 2+1}\frac{1}{5}B(\mathrm{E2}; 0^+ \to 2^+) && (1.11)\\
&= \frac{24\pi}{450\hbar}\left(\frac{E_\gamma}{\hbar c}\right)^5\frac{1}{5}B(\mathrm{E2}; 0^+ \to 2^+) && (1.12)\\
&= \frac{24\pi}{450}\frac{c}{137}\left(\frac{E_\gamma}{\hbar c}\right)^5\frac{1}{5e^2}B(\mathrm{E2}; 0^+ \to 2^+) && (1.13)
\end{aligned}$$

Here, we used $e^2 = \hbar c\alpha$, where α is the fine-structure constant ($\alpha \approx 1/137$).

Using $\hbar c = 197$ MeV $\cdot$ fm and $c = 3.00 \times 10^{23}$ fm, s^{-1}, if we express E_γ in units of E_γ/MeV and $B(E2)$ in $B(E2)/(e^2\mathrm{fm}^4)$,

$$\begin{aligned}
\frac{1}{\tau(\mathrm{E2}; 2^+ \to 0^+)} &= \frac{24\pi}{450}\frac{3.00\times 10^{23}}{137}\left(\frac{E_\gamma}{197}\right)^5\frac{1}{5}B(\mathrm{E2}; 0^+ \to 2^+) && (1.14)\\
&= 2.47\times 10^8\, E_\gamma^5\, B(E2; 0^+ \to 2^+)\ [\mathrm{sec}^{-1}] && (1.15)
\end{aligned}$$

$$\therefore\ \tau(\mathrm{E2}; 2^+ \to 0^+) = \frac{4.04\times 10^3}{E_\gamma^5 B(\mathrm{E2}; 0^+ \to 2^+)}\ [\mathrm{ps}] \qquad (1.16)$$

1.3.3 Weisskopf unit

It is assumed that only one nucleon is moving inside the nucleus, and that the angular momentum of that nucleon determines the spin of the entire nucleus (single particle model). If this change in the state of motion of the nucleon causes the nucleus to make an Eλ transition from j_i to j_f, the transition probability is approximately proportional to $R_0^{2\lambda}$, where R_0 is the nuclear radius. As a simple assumption, if we consider the potential distribution acting on the nucleus to be a uniform distribution inside radius R_0, the E2 transition of $0^+ \to 2^+$ can be written as :

$$B_\mathrm{w}(\mathrm{E2}; 0^+ \to 2^+) = \frac{9}{20\pi}R_0^4 \qquad (1.17)$$

Here, R_0 is expressed as follows using the general nuclear radius formula,

$$\begin{aligned}
R_0 &= r_0 \times A^{1/3}\\
(r_0 &= 1.2\ [\mathrm{fm}])
\end{aligned} \qquad (1.18)$$

*2)Please refer to the textbook [11] p124, equation (4.91), etc.

then becomes,

$$B_{\mathrm{w}}(\mathrm{E2}; 0^+ \rightarrow 2^+) = 0.297 \times A^{4/3}\ [e^2\mathrm{fm}^4] \equiv 1\ [\mathrm{W.u.}] \tag{1.19}$$

and this value is called the Weisskopf unit. The Weisskopf unit is sometimes used as a unit of magnitude of a transition probability. For example, a transition probability 10 times the Weisskopf unit is expressed as "10 W.u.". In this case, the Weisskopf value was the transition intensity involving only one nucleon, which means that approximately 10 nucleons are involved in the excitation.

From this, it can be said that the magnitude of the reduced transition probability $B(\mathrm{E}\lambda)$ strongly depends on the number of nucleons involved in the excitation, i.e., the collectivity of the nucleus.

1.3.4 $B(\mathrm{E2})$ and magic numbers

So far, we have stated that $B(\mathrm{E2})$ can be used as an indicator of collectivity, i.e., the number of nucleons involved in collective excitation. In addition, the appendix A describes the relationship between $B(\mathrm{E2})$ and the magnitude of the quadrupole deformation. A characteristic of nuclei with magic numbers of nucleons is that the energy of the 2_1^+ level is high. However, relying solely on the 2_1^+ energy can be insufficient, because it does not directly quantify the number of nucleons participating in collective motion. The reduced transition probability $B(\mathrm{E2})$, on the other hand, provides a direct measure of the collective participation of nucleons, allowing a more accurate assessment of nuclear collectivity and its relationship to magic numbers.

1.4 Magicity of $N = 40$ around Ti ($Z = 22$)

The fact that ^{68}Ni has magical nucleus-like properties was theoretically predicted in the 1980s [14, 15] and confirmed experimentally [16–19]. In fact, the $E(2_1^+)$ of ^{68}Ni is higher than that of surrounding nuclei, and the B(E2) is smaller than that of surrounding nuclei, suggesting the magic nature of $N = 40$. As mentioned in section 1.1.2 , 40 is a magic number in the harmonic oscillator model. In addition, the next orbital $1g_{9/2}$, when 40 protons or neutrons are filled, is clearly separated in energy from the adjacent orbitals in spherical nuclei [16]. As a result, when N or Z is close to a magic number, the nucleus tends toward sphericity, leading to subshell closure when the other number is 40 [16]. In addition to ^{68}Ni shown here, subshell closure at proton number $Z = 40$ has been confirmed in ^{90}Zr [20]. It has been suggested that shell closure may also occur in ^{60}Ca with proton magic number $Z = 20$, which could potentially influence the properties of the surrounding Ti isotopes. However, in the currently observed ^{62}Ti with $N = 40$, $E(2_1^+)$ is not higher than the surrounding nuclei, and no signs of this have been seen. However, the shell model calculations described in the next section predict that $E(2_1^+)$ will be lower even if $N = 40$ is a magic number. This indicates that the energy of the first 2^+ state alone may not

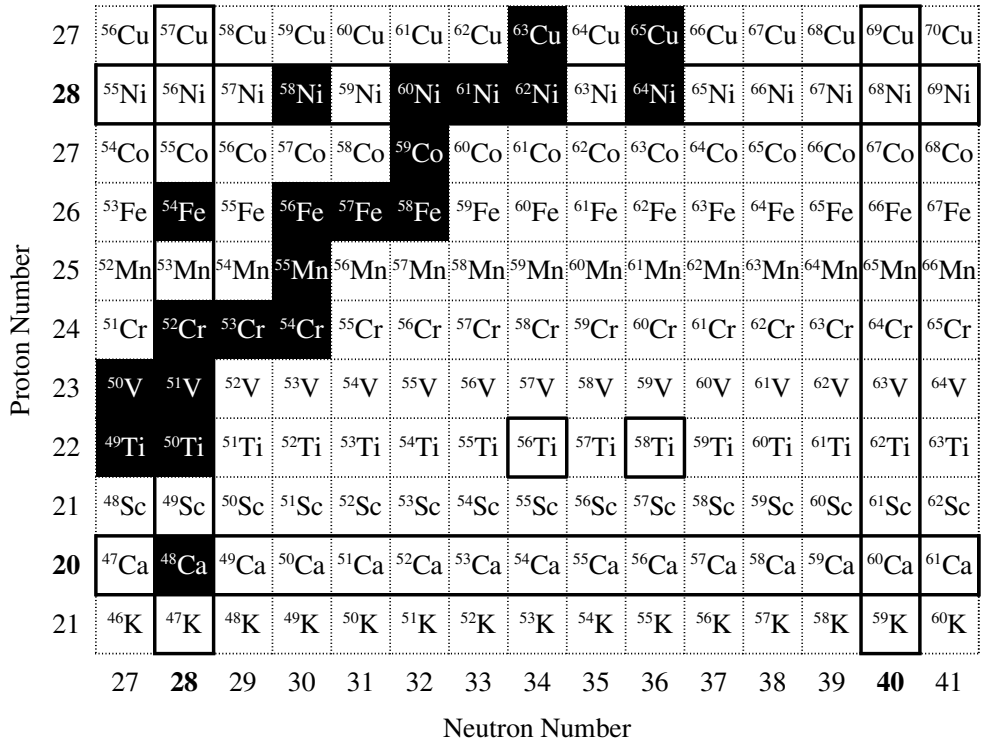

Figure 1.5: ^{56}Ti and ^{58}Ti are located between $N = 28$ and 40. Filled nuclei are stable.

clearly reflect the shell closure, and therefore the $B(\mathrm{E2})$ value, which measures the ease of quadrupole excitation, is also needed to assess whether $N = 40$ behaves as a magic number.

1.5 Experimental $B(\mathrm{E2})$ for Ti isotopes

1.5.1 Up to ^{56}Ti

The $B(\mathrm{E2})$ values have been measured up to ^{56}Ti [21]. The most neutron-rich Ti isotope with known $B(\mathrm{E2})$, ^{56}Ti was measured at NSCL using Coulomb excitation with a ^{197}Au target [22].

1.5.2 At ^{58}Ti

At ^{58}Ti, there is model-dependent $B(\mathrm{E2})$ experimental value. Suzuki et al. measured the deformation length δ of ^{58}Ti from the (p, p') scattering cross section. [23] As a result, $\delta_{p,p'} = 0.83^{+22}_{-30}$ [fm] was obtained. Obtained $B(\mathrm{E2})$ from this value using the formulas (H.1), (A.8), and (A.9), we get $B(\mathrm{E2}; 0^+ \to 2^+) = 416^{+263}_{-231}$ $[e^2\mathrm{fm}^4] = 6.3(37)$[W.u.]. It should be noted that this $B(\mathrm{E2})$ value is derived not only using the nuclear radius formula (H.1) but also under the assumption that the neutron and proton deformation lengths are equal, $\delta_n = \delta_p$. For reference, in Coulomb excitation experiments, the determination of $B(\mathrm{E2})$ similarly requires the nuclear radius R, which enters the conversion from the measured cross section to the $B(E2)$ value.

1.6 Theoretical $B(\mathrm{E2})$ values

Electric quadrupole transition probabilities, $B(\mathrm{E2})$, can be calculated unambiguously if the nuclear wave functions are known. Various theoretical frameworks,

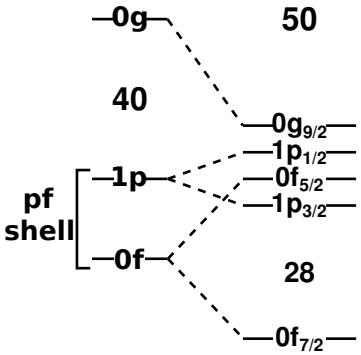

Figure 1.6: Enlarged view of the shell model level near $N = 40$.

including shell models (SM) and self-consistent QRPA models based on Skyrme energy density functionals (EDFs), can provide such wave functions and thus enable the evaluation of $B(\mathrm{E2})$ values. In this work, we focus on the shell model as a representative method, as it has been shown to reliably describe the structure of nuclei near closed shells and allows a consistent calculation of $B(\mathrm{E2})$ strengths.

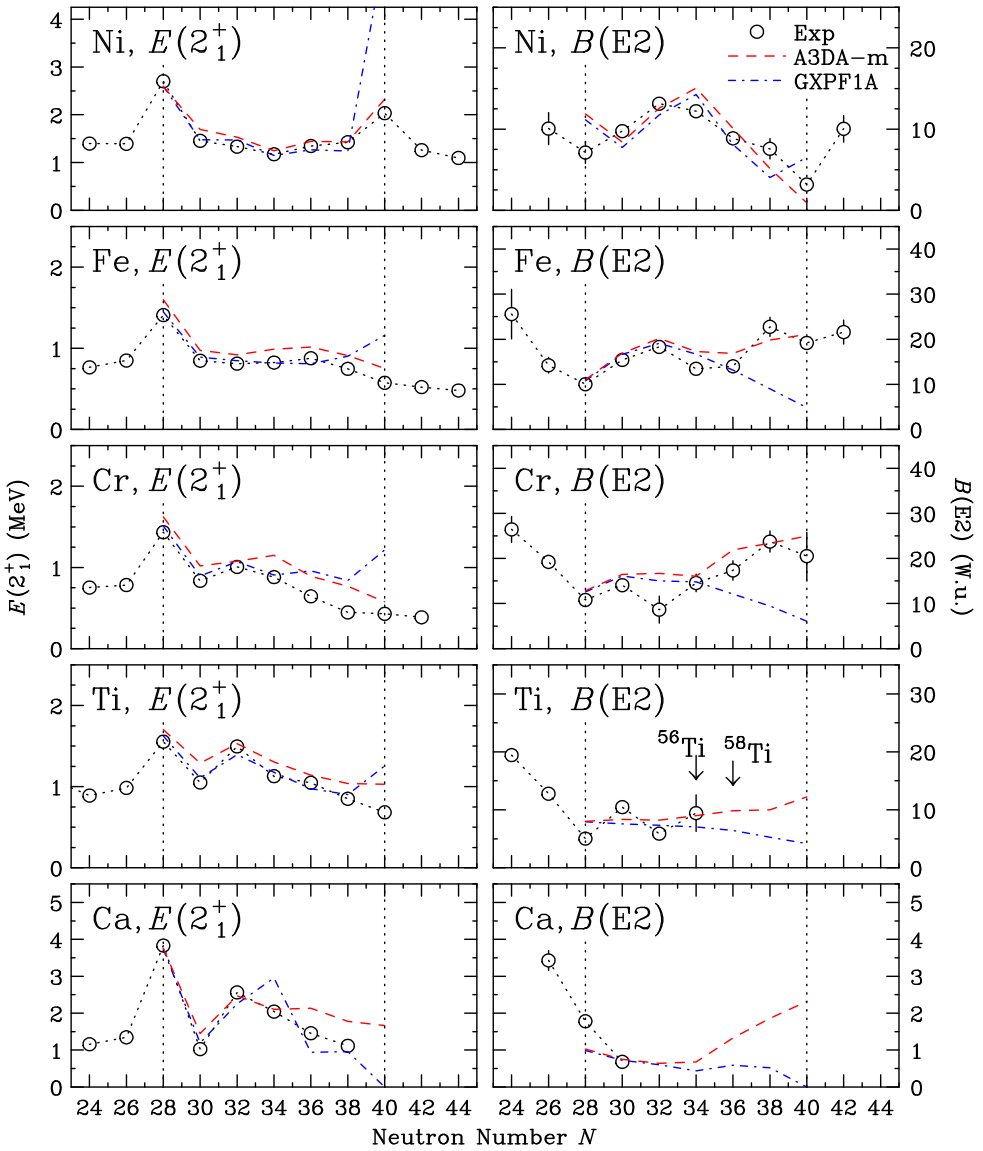

Figure 1.7: Observed energies of the first 2^+ level, $E(2_1^+)$ and $B(\mathrm{E2})$, for the even-even nuclei Ca ($Z = 20$), Ti ($Z = 22$), Cr ($Z = 24$), Fe ($Z = 26$), and Ni ($Z = 28$). At the magic number $N = 28$, $E(2_1^+)$ is high and $B(\mathrm{E2})$ is low for all elements except Ca, but at $N = 40$, this characteristic is only seen for Ni.

1.6.1 Shell models (1) – GXPF1A

GXPF1A [24,25] is a shell-model interaction defined for the "pf shell" (consisting of four orbitals: $1p_{3/2}$, $1p_{1/2}$, $0f_{5/2}$, and $0f_{7/2}$). In this framework, the model specifies the single-particle energies and the effective interactions between nucleons occupying these orbitals. Using these ingredients, the nuclear wave functions are obtained by diagonalizing the Hamiltonian within the model space, and it reproduces well nuclei in which the proton or neutron is close to the magic number 28. Unlike A3DA-m described below, the $0g_{9/2}$ orbital is not included in the calculation, so in this model, the gap to the $0g_{9/2}$ orbital is effectively treated as too large to allow excitation, and $N = 40$ is therefore regarded as having magic properties.

1.6.2 Shell models (2) – A3DA-m

A3DA-m [26] is a modified A3DA [27,28]. The calculation is performed in a model space that, in addition to the pf shell, incorporates the $0g_{9/2}$ and $1d_{5/2}$ orbitals. In this model, the gap between the pf shell and the $0g_{9/2}$ orbital is small, and excitation to the $0g_{9/2}$ orbital occurs easily. Thus, $N = 40$ is generally not treated as a closed shell in this model, although nuclei such as ^{68}Ni may still exhibit magic-like features.

1.6.3 Self-consistent QRPA models based on Skyrme EDF

We received theoretical results on Ti isotopes through private communications with Dr. Yoshida and Dr. Washiyama. The calculations are based on the Skyrme energy density functional SkM*, but employ two different frameworks. The first one, referred to as QRPA (SkM*), is the deformed Skyrme-HFB plus QRPA approach,

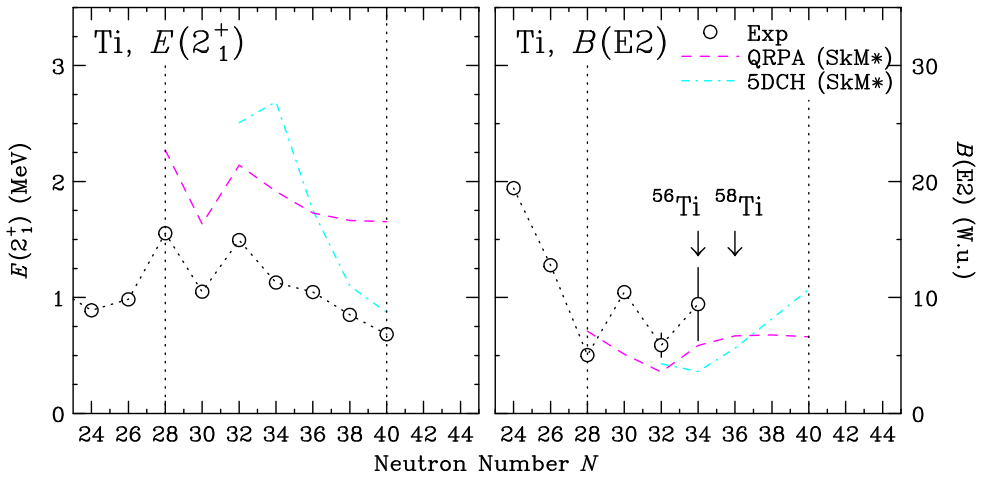

Figure 1.8: Two self-consistent QRPA models based on Skyrme EDF.

which provides a microscopic description of low-lying excitation modes on top of the mean field [29]. The second one, called 5DCH (SkM*), is the five-dimensional collective Hamiltonian formalism, where the collective potential is obtained from constrained HFB calculations and the inertial functions from local QRPA with the SkM* functional [30]. A comparison between these theoretical models and experimental data is shown in Fig. 1.8.

1.7 Purpose of this study

In recent decades, extensive studies of neutron-rich nuclei have revealed the emergence of new magic numbers as well as the disappearance of conventional ones. Such phenomena are closely linked to shell evolution and the mechanisms that govern nuclear collectivity. Around neutron number $N = 40$, a striking contrast is observed: while nuclei near ^{68}Ni exhibit signatures of magicity, isotopes of Cr and Fe show enhanced collectivity, indicating a breakdown of the $N = 40$ shell closure. In the case of Ti isotopes, however, information on quadrupole collectivity has so far been limited, as $B(\mathrm{E2})$ values beyond $N = 34$ had not been measured.

The primary objective of this study is to measure the $B(\mathrm{E2}; 0^+ \rightarrow 2^+)$ value of ^{58}Ti with $N = 36$, which serves as a crucial probe of collectivity in this region.

By obtaining this result, we aim to address two key issues. The first is to examine the "magicity" of the $N = 40$ shell gap in Ti isotopes; in this work, the magicity of $N = 40$ is defined as the extent to which excitations across the $N = 40$ shell gap are suppressed. The second is to investigate how the tensor force modifies shell gaps and thereby influences collectivity around $N = 40$.

To this end, we have measured the $B(\mathrm{E2}; 0^+ \rightarrow 2^+)$ transition strength in ^{58}Ti and compared the results with shell-model calculations.

1.8 Research method

1.8.1 Obtaining B(E2) for ^{56}Ti / ^{58}Ti

Currently, only the deformation length $\delta_{p,p'}$ has been measured for ^{58}Ti in a (p, p') experiment by H. Suzuki et al. [23]. Although B(E2) can be evaluated from this result, the conversion is model-dependent and involves a large uncertainty. Therefore, we aim to obtain B(E2) using a method that is less model-dependent and provides smaller errors than (p, p'). There are two possible methods for this:

- Measuring the lifetime τ
- Measuring the Coulomb excitation cross section σ_{coulex}

1.8.2 Measurement of lifetime τ

From the relationship in equation (1.16), if E_γ is known, B(E2) can be obtained most simply by measuring the lifetime τ. In the experiments conducted in this study, it was in principle possible to measure the lifetime using the Doppler shift attenuation method (DSAM) [31], but since the error is expected to be very large, we decided to obtain B(E2) by measuring the Coulomb excitation cross section, as described below.

1.8.3 Measurement of Coulomb excitation cross section σ_{coulex}

Coulomb excitation is the excitation of a nucleus by electromagnetic interactions when it passes near a heavy target nucleus, although historically the excitation of the target nucleus was also studied. In this work, we consider mainly the excitation of the projectile nucleus. Typical target nuclei are those with large atomic numbers, such as lead or gold, although lighter systems (e.g., oxygen) are sometimes used at lower energies.

This process can be viewed as the inverse of gamma decay: while gamma decay proceeds as $2^+ \rightarrow 0^+$ with the emission of real photons, Coulomb excitation corresponds to the $0^+ \rightarrow 2^+$ transition induced by electromagnetic interactions. Strictly speaking, this is not an exact inverse process, but through the concept of virtual photons it can be regarded as the reverse reaction.

At this time, in the range of excitation energies $\sim$ 10 MeV or less, a rough approximation is $\sigma_{\text{coulex}} \propto B(E2)$. For details, see the appendix B.

In order to actually obtain B(E2) from σ_{coulex}, one needs to estimate the number of virtual photons generated in the Coulomb field. This can be done using the so-called

virtual photon method, or alternatively by performing a reaction calculation such as the distorted wave Born approximation (DWBA). In this work, the latter approach is adopted; $B(\mathrm{E2})$ is extracted by comparing the measured Coulomb excitation cross section with the results of DWBA calculations, as described later. Therefore, $B(\mathrm{E2})$ can be obtained by measuring σ_{coulex} in an experiment.

1.8.4 How do we measure the Coulomb excitation cross section σ_{coulex}?

^{56}Ti / ^{58}Ti are neutron-rich unstable nuclei, with 6 to 8 more neutrons than ^{50}Ti, the most stable Ti isotope.

Therefore, ^{56}Ti / ^{58}Ti do not exist in nature unless they are produced in a laboratory. To do this, we first need to produce ^{56}Ti / ^{58}Ti using an accelerator. To induce Coulomb excitation, a beam of ^{56}Ti / ^{58}Ti must be irradiated onto a target made of a nucleus with a sufficiently large atomic number. In this study, we decided to use ^{197}Au. The best way to confirm Coulomb excitation is to observe the gamma rays emitted during de-excitation. To do this, gamma rays are counted by placing gamma ray detectors around the ^{197}Au target. The Coulomb excitation cross section σ_{coulex} can be obtained using the gamma ray count obtained in this way, the amount of incident ^{56}Ti / ^{58}Ti beam, and the ^{197}Au target thickness. In the next chapter, we describe the experimental principle for measuring the Coulomb excitation cross section σ_{coulex} of ^{56}Ti / ^{58}Ti.

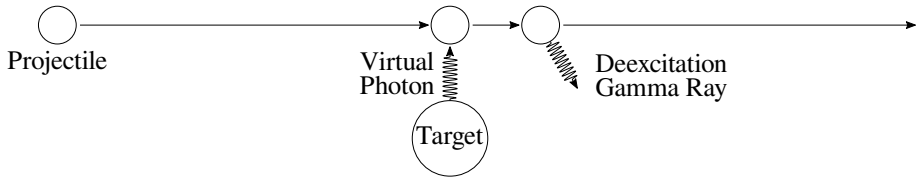

Figure 1.9: Conceptual diagram of Coulomb excitation. The change in the strong electric field that the incident particle experiences when passing near a target nucleus with a large Z is considered to be the incidence of virtual photons (electromagnetic waves), and this reaction excites the incident particle with virtual photons. The excited incident particle emits de-excited gamma rays after the gamma decay lifetime has expired.

Chapter 2

Experimental Principle and Setup

2.1 Overview of experiment

Beams of ^{56}Ti and ^{58}Ti were generated using the Superconducting Ring Cyclotron and BigRIPS beamline at the RIKEN RI Beam Factory. The ^{56}Ti/^{58}Ti beams were then directed onto a ^{197}Au target to induce Coulomb excitation. The de-excitation gamma rays from the Coulomb excitation were observed with a Ge detector array "HiCARI" and we measured the Coulomb excitation cross section.

2.2 Structure of this chapter

This chapter describes the method of generating unstable nuclear beams at the RI Beam Factory, the BigRIPS/ZeroDegree beamline for particle identification of the generated unstable nuclear beams and analysis of their trajectories and momentum, and the HiCARI array for gamma ray detection, and describes the equipment,

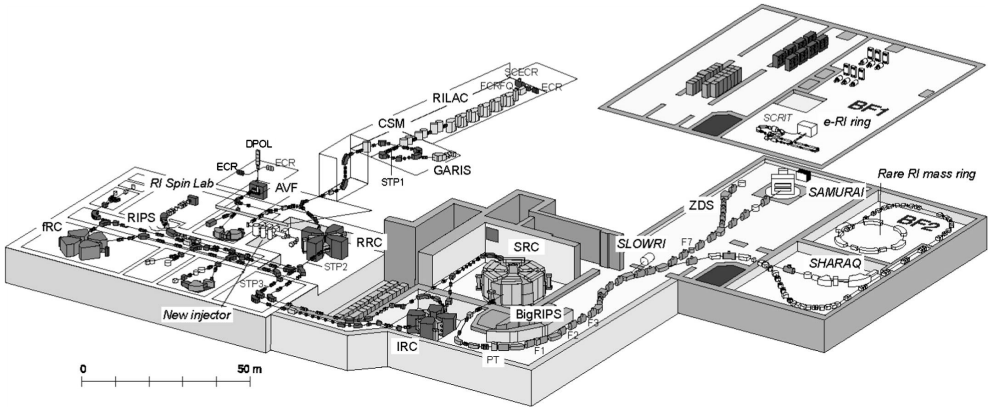

Figure 2.1: A bird's-eye view of the RIKEN RI Beam Factory. In the figure, the beam accelerated by the SRC (Superconducting Ring Cyclotron) is used to generate RI beams at the BigRIPS beamline.

measurement principle, and setup for each section.

2.3 Overview of the RI Beam Factory

The RI Beam Factory can produce RI (radioactive/unstable nuclei) beams by using a group of accelerators, including the Superconducting Ring Cyclotron (SRC), and the BigRIPS beamline [32], which generates unstable nuclei, purifies them, and identifies particles. At present, this method is the most powerful way to generate beams in the ^{56}Ti/^{58}Ti vicinity. Figure 2.1 shows a bird's-eye view of the RIBF facility, and Figure 2.2 shows a schematic diagram of the beamline after the SRC accelerator. In this study, a ^{197}Au target and a HiCARI array are installed at the F8 focal plane.

2.4 Unstable nucleus beam generation at the RI Beam Factory

RI beams are first generated by generating a primary beam using stable nuclei as an ion source, and then irradiating the target at the F0 focal plane to generate a secondary beam through nuclear spallation and fission reactions. The primary beam is accelerated to 345 MeV/u using RILAC (linear accelerator) and four cyclotrons at RRC, fRC, IRC, and SRC.

In this study, ^{70}Zn was used as the primary beam, and an attempt was made to generate a ^{56}Ti / ^{58}Ti beam by a nuclear spallation reaction.

The secondary beam generated by the nuclear spallation reaction is a cocktail beam containing many types of nuclides, which are separated/purified by utilizing the curvature when passing through a magnetic field and the difference in energy

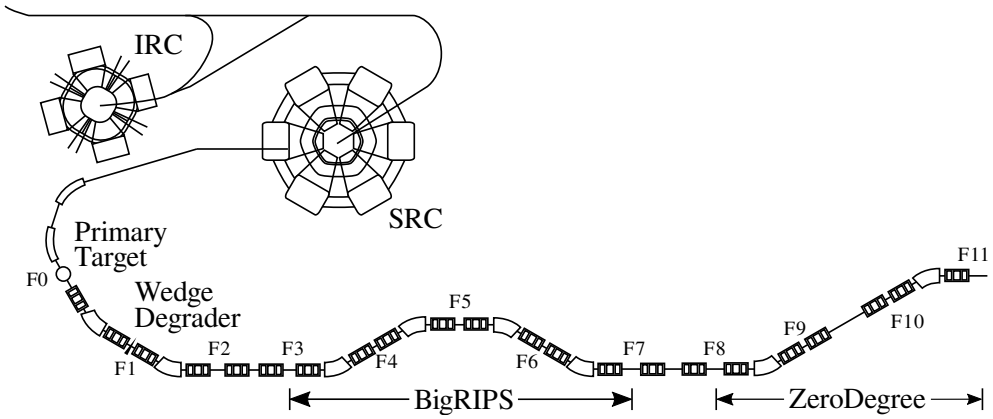

Figure 2.2: BigRIPS and ZeroDegree beamlines at the RIKEN RIBF facility. F0 - F11 in the figure are the names of the focal planes. The detectors installed at each focal plane are summarized in table 2.1.

loss when passing through a material. Purification of the secondary beam is also explained in this section.

2.4.1 Generation of unstable nuclear beams

A primary target (production target) for generating unstable nuclei is installed on the F0 focal plane. ^{7}Be is mainly used as the primary target. The original beam particles of the primary beam are destroyed by spallation and fission reactions, producing various nuclei with small mass numbers. In this study, a spallation reaction using a ^{70}Zn beam is used. The particles produced by the nuclear reaction in the primary target include particles necessary for the beam, such as ^{58}Ti in this study. However, large amounts of other particles are also produced, which become background sources during measurements. Therefore, it is necessary to remove as many particles as possible other than the desired beam particles.

2.4.2 Purification of an unstable nuclear beam by a slit

The unstable nuclear beam generated at the primary target in the F0 focal plane is bent by a dipole magnet and transported to the F1-F3 focal planes. The particle orbit, i.e., the orbit radius ρ when bent by the magnetic field B, is determined by the particle's velocity v, mass m, and charge q. The non-relativistic equation of motion for the circular motion of a charged particle orbiting in a magnetic field is :

$$m\frac{v^2}{\rho} = qvB \tag{2.1}$$

Transforming this,

$$B\rho = \frac{mv}{q} \tag{2.2}$$

can be written as follows.

In this case, the right-hand side is an index that represents the characteristics of the beam particle's "resistance to bending due to a magnetic field." For this reason, $B\rho$ is called the "magnetic rigidity modulus." If the magnetic field does not fluctuate, beam particles with the same $B\rho$ value will follow the same trajectory if the initial conditions are the same.

In reality, the beam particle velocity needs to be treated relativistically, so the momentum mv in the formula (2.2) is replaced with the momentum γmv that takes relativity into account, and using the atomic mass unit m_u, the elementary charge e,

and the velocity of light c, $m \equiv m_u A$, $q \equiv Ze$, and $v \equiv \beta c$,

$$B\rho = \frac{\beta\gamma c m_u}{e}\frac{A}{Z} \tag{2.3}$$

is obtained. Here, $\gamma \equiv \frac{1}{\sqrt{1-\beta^2}}$. If the beam particles have relatively uniform velocities β, $B\rho$ is roughly proportional to A/Z. Therefore, the trajectory that the target particle should take is restricted to some extent by the value of A/Z that the particle has. Therefore, by installing a slit in the beamline, it is possible to restrict the $B\rho$, i.e., A/Z, of the particles that can pass through it. This makes it possible to remove beam particles with $B\rho$ values that deviate significantly, and increase the purity of the secondary beam. Slits are installed in the focal planes of F1 - F3. However, this method alone still leaves a large amount of other particles with similar $B\rho$ values remaining.

2.4.3 Purification of unstable nuclear beams using a wedge-shaped damping plate

A wedge-shaped damping plate is also installed at the F1 focal plane. The wedge-shaped damping plate is installed where the beamline is bent, and is made of an aluminum plate that becomes thinner from the outside to the inside. The energy lost by beam particles when passing through a material depends on the amount of charge that the particle has, i.e., Z, so it can be used to select particles with different Z. First, for simplicity, consider a damping plate with a constant thickness. The energy loss when passing through a material is given by the Bethe-Bloch formula.

$$-\frac{dE}{dx} = \frac{4\pi}{m_e c^2}\cdot\frac{Z^2}{\beta^2}\cdot\left(\frac{e^2}{4\pi\varepsilon_0}\right)^2\cdot n\left[\ln\left(\frac{2m_e c^2\beta^2}{I(1-\beta^2)}\right)-\beta^2\right] \tag{2.4}$$

This can be simplified as follows when the change in β ($\Delta\beta$) is sufficiently small compared to the absolute value of β.

$$|\Delta E| \propto \left(\frac{Z}{\beta}\right)^2 \tag{2.5}$$

Earlier, we restricted the A/Z of beam particles by $B\rho$, but the damping plate changes the kinetic energy depending only on Z. For this reason, even if a particle has the same $B\rho$ before the F1 focal plane, if Z is different, $B\rho$ after passing through the damping plate will have a different value. As a result, the difference in $B\rho$ becomes larger at the next F2 slit, making it difficult to pass through. In this way, the beam is purified by the slits and wedge-shaped damping plate in F1 - F3. Incidentally, the reason why the damping plate is wedge-shaped rather than flat is that particles

passing outside the beamline, i.e. particles with a large $B\rho$, have a large velocity β when A and Z are the same. By passing particles with a large β through the thicker part and particles with a small β through the thinner part, the spread of β is reduced. Even if the beam is purified using the method described in this section using a slit and a wedge-shaped damping plate, it is difficult to actually create a completely pure beam of a single type of particle. In some cases, dozens of types of particles may still be included. Therefore, in the next section, we will describe a method to identify beam particles by measuring A/Z and Z for each beam particle and analytically select beam particles.

2.5 Particle Identification in BigRIPS / ZeroDegree

Particle identification in BigRIPS / ZeroDegree is performed using the $B\rho$-ΔE-TOF method. The $B\rho$-ΔE-TOF method is a method for determining the type of beam particle by measuring three physical quantities: $B\rho$ (magnetic rigidity), ΔE (energy loss when passing through a material), TOF (**T**ime **O**f **F**light, i.e. the time it takes to travel between two points). Particle identification can be determined using these physical quantities in the following way.

- First, the particle velocity β is calculated from the TOF measurement.
- Z is determined by measuring ΔE and the relationship $\Delta E \propto (Z/\beta)^2$.
- A/Q is determined by measuring $B\rho$ and the relationship $A/Q \propto B\rho/(\beta\gamma)$.

This determines the particle's Z and A/Q. Note that in reality, β decreases slightly due to energy loss when passing through a measuring device, but for now we will ignore this effect.

2.5.1 Measurement of TOF and derivation of velocity β (1)

TOF is measured as the time difference between the emission timing of two plastic scintillators installed on the beamline. The plastic scintillators are installed at F3 and F7 in BigRIPS, and at F8 and F11 in ZeroDegree. The distance between F3 and F7 is 46.566 m, and between F8 and F11 is 36.48 m. The relative velocity β to the velocity of light can be calculated using the usual velocity equation and the velocity of light c as follows:

$$\beta = \frac{L}{\mathrm{TOF} \cdot c} \tag{2.6}$$

However, this method can only be used to measure between F3 and F7, and between F8 and F11. To calculate β for a small range, such as F5 and F7, use the measured value of $B\rho$. The detailed method will be described in a later subsection (2.5.4).

2.5.2 Measurement of ΔE and derivation of atomic number Z

ΔE is measured using ion chambers called "MUSIC" installed at the F7 and F11 focal planes. The ion chambers can directly measure the energy loss ΔE when passing through the filled gas. By determining the appropriate proportionality coefficient from the proportional relationship in equation (2.5), Z/β can be obtained, so if β is known, Z can also be determined.

2.5.3 Measurement of $B\rho$ and derivation of mass-to-charge ratio A/Q

$B\rho$ is obtained from the magnetic field of a particle position detector called a PPAC and a dipole magnet. PPACs are installed at the F3, F5, F7, F8, F9, F10, and F11 focal planes, and two sets of "double PPACs" consisting of two PPACs stacked on top of each other are installed at each focal plane. Only the F8 focal plane has three sets, two sets installed upstream and one set installed downstream of the target. The PPAC can measure the (x, y) coordinates through which the beam particle passes. By analyzing multiple PPACs, the traveling direction (a, b) of the beam particle can be obtained. The transport matrix can be obtained from these to obtain $B\rho$. The derivation methods include B measured by a nuclear magnetic resonance (NMR) magnetic field measuring device and the central orbit ρ determined by the beamline design. The $B\rho$ determined by this is called $B\rho_0$. The $B\rho$ of each beam particle is

$$B\rho = B\rho_0(1 - \delta) \tag{2.7}$$

Here, if we replace mv in equation (2.2) with momentum p, the relationship holds even in relativity, so by substituting this into equation (2.7), we get

$$p = p_0(1 + \delta) \tag{2.8}$$

$$\therefore \delta = \frac{p_0 + p}{p_0} \tag{2.9}$$

The beam transport matrix is summarized in the appendix C. Returning to the point, if we have the matrix elements and the measured x_3, a_3, x_5, a_5 pairs, we can determine δ_{35} for each beam particle using equation (C.1). If we measure δ for each section using this method, we can obtain $B\rho$ for each beam particle using equation

(2.7). Now, by transforming equation (2.3),

$$\frac{A}{Z} = \frac{e}{\beta\gamma c m_u} B\rho \tag{2.10}$$

β can be calculated from the TOF, so once $B\rho$ is determined, A/Z can be determined because it is a constant.

2.5.4 Measurement of TOF and derivation of velocity β (2)

To obtain β for a small interval such as F5 - F7, the measured value of $B\rho$ can be used. As an example, assume that the TOF measurement interval is F3 - F7, and we want to obtain β for F3 - F5 and F5 - F7 in between. Let the subscripts $_{37}$, $_{35}$, and $_{57}$ represent the respective intervals. First, the sum of the TOFs for each interval is the TOF for the entire interval. This can be expressed as an equation:

$$\mathrm{TOF}_{37} = \mathrm{TOF}_{35} + \mathrm{TOF}_{57} \tag{2.11}$$

$$\therefore \frac{L_{37}}{\beta_{37} c} = \frac{L_{35}}{\beta_{35} c} + \frac{L_{57}}{\beta_{57} c} \tag{2.12}$$

Also, if there is no change in the charge state due to detectors or wedge-shaped damping plates in the beamline, or if no nuclear reactions occur, A/Q will not change. From this, the right-hand side of equation (2.10) is constant. Therefore, we obtain

$$\frac{B\rho_{35}}{\beta_{35}\gamma_{35}} = \frac{B\rho_{57}}{\beta_{57}\gamma_{57}} \tag{2.13}$$

$$\therefore \frac{B\rho_{57}}{B\rho_{35}} = \frac{\beta_{57}\gamma_{57}}{\beta_{35}\gamma_{35}} \tag{2.14}$$

In other words, the ratio of $B\rho$ becomes the ratio of $\beta\gamma$. If the ratio of $B\rho$ is known from measurements, γ is a function of β, and if we have the measured values of TOF_{37} and L_{35} and L_{57}, β_{35} and β_{57} can be found by solving the simultaneous equations.

Table 2.1: A list of detectors and other equipment installed on the BigRIPS and ZeroDegree beamlines.

Focal plane	Contents (detector)
F0	primary (generation) target
F1	Wedge Degrader
F2	-
F3	Plastic scintillator (F3PLscint) Double PPAC×2 (F3DPPAC1, F3DPPAC2)
F4	-
F5	Double PPAC×2 (F5DPPAC1, F5DPPAC2) Wedge Degrader
F6	-
F7	Double PPAC×2 (F7DPPAC1, F7DPPAC2) Ion chamber MUSIC (F7IC) Plastic scintillator (F7PLscint)
F8	Double PPAC×3 (F8DPPAC1, F8DPPAC2, F8extraDPPAC) Plastic scintillator (F8PLscint) Secondary (reaction) target and HiCARI array
F9	Double PPAC×2 (F9DPPAC1, F9DPPAC2)
F10	Double PPAC×2 (F10DPPAC1, F10DPPAC2)
F11	Double PPAC×2 (F11DPPAC1, F11DPPAC2) Plastic scintillator (F11PLscint) Ion chamber MUSIC (F11IC)

2.6 BigRIPS / ZeroDegree detector configuration (beamline detector)

First, let us explain the "Beamline Detector" installed in the BigRIPS / ZeroDegree beamline. These are used to identify particles for each event using the $B\rho$-ΔE-TOF method.

2.6.1 Plastic scintillator

They are installed in F3, F7, F8, and F11 mainly to obtain TOF. The area of the scintillator is the same for all, 120×100 mm^2. The thickness varies depending on the experimental setup and installation location. In this experiment, only F8 uses a 1.0 mm thickness, while the others use a 0.2 mm thickness.

Two photomultiplier tubes are installed on both the left and right sides, and the approximate particle passing position can be estimated from the detection time difference between the left and right sides and the relationship between the emission attenuation. The photomultiplier tube is set at a voltage of 1700 - 2000 V, and the voltage is adjusted so that the pulse height is several hundred mV depending on the size of the signal in the actual experiment. This is because when the signal is small, the discriminator used to measure the luminescence time loses its time resolution due to the walk effect and slew effect, so this is to prevent this. The final time when the particle passes is determined as the average timing of the signals from the left and right photomultiplier tubes.

2.6.2 PPAC

Parallel Plate Avalanche Counters (PPAC) [33] are a type of position-sensitive detector. It can determine the positions x, y and the angles a, b in the x and y directions. It is installed at the convergent foci F3, F7, F8, F11 and the divergent foci F5, F9. The divergent foci use a size of 240×150mm^2 to cover a wide range. The cathode output has two readouts, X1, X2, Y1, and Y2, in the x and y directions. The cathode electrodes in each direction are connected by delay cables, and the difference in the readout times of X1 and X2 (or Y1 and Y2) is proportional to the position. For example, in the x direction, if the readout times for X1 and X2 are T_{X1} and T_{X2}, then it is expressed as follows:

$$x = \alpha(T_{\mathrm{X1}} - T_{\mathrm{X2}}) + x_{\mathrm{offset}} \tag{2.15}$$

Here, α and x_{offset} are pre-calibrated with an alpha source. The anode output is not used in principle. BigRIPS/ZeroDegree uses a "double PPAC" consisting of two PPACs stacked on top of each other. The detection efficiency of a PPAC is about 90 %, but by using a double PPAC, the detection efficiency is improved to about 99 %. Two sets of double PPACs are installed on each focal plane. The angles a, b can be obtained by outputting x, y from the two double PPACs, respectively.

2.6.3 MUSIC

This ion chamber is called **MU**lti-**S**ampling **I**onization **C**hamber [34] and is used to obtain dE/dx. It is installed at the F7 and F11 focal planes.

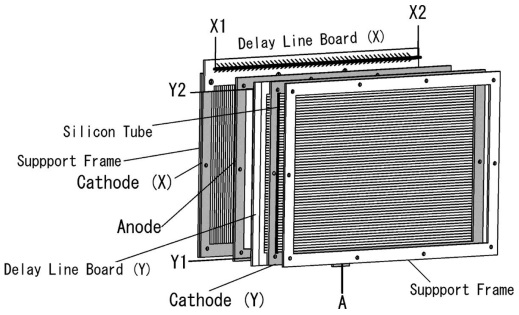

Figure 2.3: Schematic diagram of PPAC. Figure from [33].

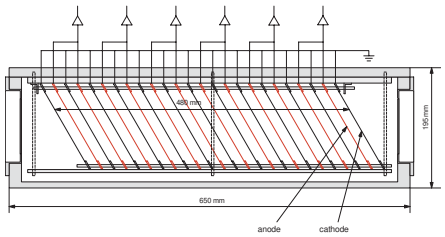

Figure 2.4: Schematic diagram of MUSIC. Figure from [35].

2.7 Principle of gamma-ray measurement

The purpose of this experiment is to measure the Coulomb excitation cross section of ^{56}Ti / ^{58}Ti. Coulomb excitation is a process in which a particle with a relatively large Z is excited by electromagnetic interaction when it passes nearby, and when the nucleus to be observed is used as the beam, Z is the target. When using this method, de-excitation gamma rays from ^{58}Ti are emitted during flight.

2.7.1 Doppler shift

Gamma rays emitted from nuclei in flight undergo a Doppler shift when viewed from the laboratory frame. If the energy actually emitted from the atomic nucleus is E_0, then in the laboratory frame, if it is emitted forward in the direction of the beam, it will have high energy, and if it is emitted backward, it will have low energy. If the gamma ray energy in the laboratory frame is E_{lab}, the gamma ray emission angle is θ_γ, and the velocity of the beam particle is β, This can be written as follows:

$$\frac{E_{\mathrm{lab}}}{E_0} = \frac{\sqrt{1-\beta^2}}{1-\beta\cos\theta_\gamma} \tag{2.16}$$

2.7.2 Doppler shift correction and measurement error

HiCARI is composed of Ge detectors, so the detector's intrinsic energy resolution is very good, at about a few keV. The measurement results of the energy resolution and detection efficiency of the gamma-ray source are described in the following section 2.10.

The energy resolution of the Doppler shift-corrected gamma-ray spectrum also depends on the angular resolution of the gamma-ray interaction point. The angular resolution is determined by the position resolution of the detector. From this, the relative energy resolution

$$\delta_E \equiv \frac{\Delta E_0}{E_0} \tag{2.17}$$

can be expressed as the angular resolution δ_θ, the beam velocity resolution δ_β, and the intrinsic resolution of the detector δ_{det},

$$\delta_E^2 = \delta_\theta^2 + \delta_\beta^2 + \delta_{\mathrm{det}}^2 \tag{2.18}$$

These can be calculated as:

$$\delta_\theta = \frac{\beta \sin\theta_\gamma \Delta\theta_\gamma}{1-\beta\cos\theta_\gamma} \tag{2.19}$$

$$\delta_\beta = \frac{(\beta-\cos\theta_\gamma)\Delta\beta}{(1-\beta^2)(1-\beta\cos\theta_\gamma)} \tag{2.20}$$

$$\delta_{\text{detector}} \propto \frac{1}{\sqrt{E_{\text{detection}}}} = \sqrt{\frac{1-\beta\cos\theta_\gamma}{E_0\sqrt{1-\beta^2}}} \tag{2.21}$$

The angular dependence of the energy resolution of in-beam gamma rays, taking into account δ_θ, δ_β, and δ_{det}, is calculated for NaI and Ge detectors, and is shown in Figure 2.5.

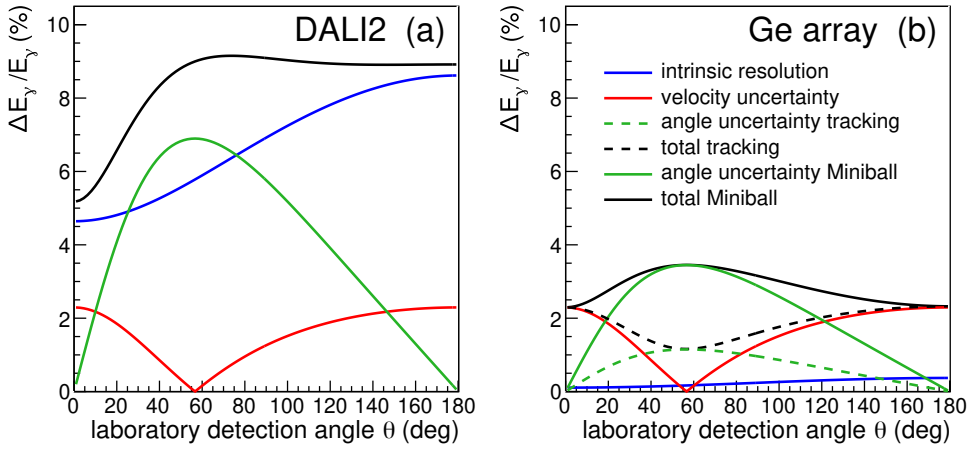

Figure 2.5: Simulated energy resolution obtained after Doppler shift correction. Comparison of resolution between DALI2 with NaI scintillator and Ge array. Ge arrays come in two types: Miniball, a common Ge detector, and Tracking type, which has improved position resolution through waveform analysis. Improved position resolution improves angular resolution δ_θ, so energy resolution after Doppler correction improves.

2.8 HiCARI (1) – Overview and each detector

2.8.1 HiCARI array/campaign overview

HiCARI (**Hi**gh-resolution **C**luster **A**rray at **RI**BF) [36] is a high-resolution gamma-ray detector array consisting of 12 Ge detectors, which consist of one RCNP Quad [37] (4 crystals), one LBNL P3 (3 crystals), six Miniball [38] (3 crystals), and four Clover (4 crystals) [39] owned by Korea IBS and China IMP. Of these, RCNP Quad and LBNL P3 are tracking detectors [40], and can derive the gamma-ray interaction position. In-beam gamma-ray nuclear spectroscopy experiments at RIBF have previously used the DALI2 [41] array, which uses NaI detectors. The HiCARI campaign experiment, which began in 2020, is the first in-beam gamma-ray nuclear spectroscopy experiment at RIBF to use a Ge detector array. Compared to NaI, Ge detectors have a much higher energy resolution, so even for very weak gamma-ray peaks, the separation accuracy (S/N ratio) against the background is high. This performance more than compensates for the low detection efficiency, which is a weakness of Ge detectors. In particular, the tracking detector has a high angular resolution used for Doppler correction, which can further increase the S/N ratio.

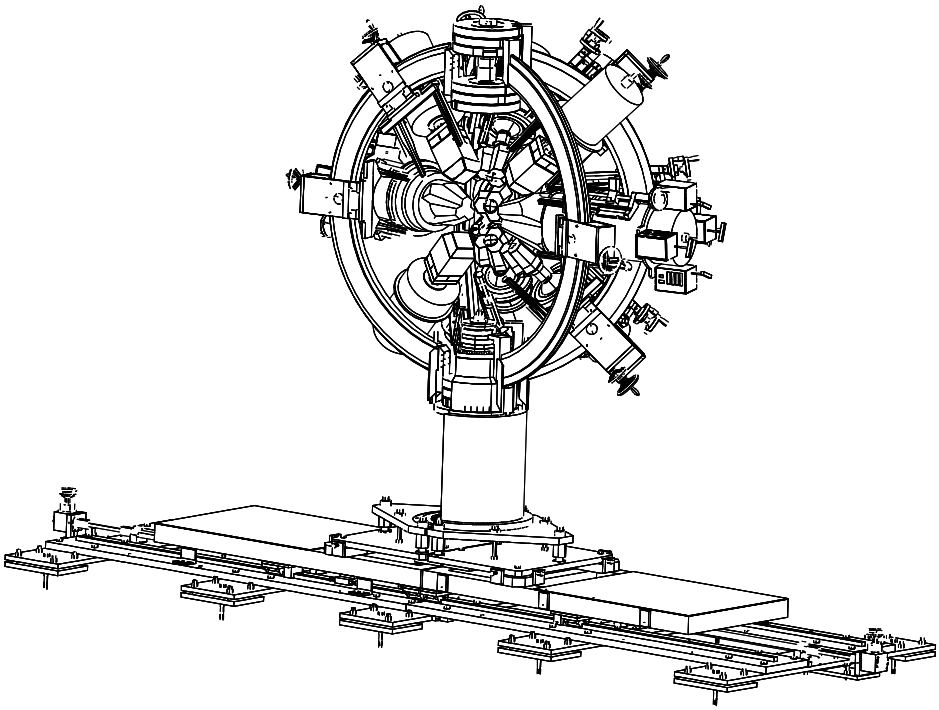

Figure 2.6: A schematic of the HiCARI array. The frame that supports the detectors was developed based on that for the Miniball.

2.8.2 Non-tracking detectors (Miniball, Clover)

The Miniball detector is a detector [42] developed for REX (Radioactive ion beam EXperiment) at ISOLDE, an online isotope separation facility at CERN, and has three coaxial Ge crystals. The readout electrode of the crystal is divided into six parts in the circumferential direction (the ϕ direction in the coaxial coordinate system). The Clover detector is a detector [43] originally developed to investigate the polarization direction of gamma rays by Compton scattering direction analysis. The Clover detector used in the HiCARI array is an improved version, with the readout electrode divided into four parts. These non-tracking detectors have the sensitive area of the crystal segmented by the electrode boundaries, so the gamma-ray detection position is treated as the segment centroid. In addition, to improve detection efficiency, a central electrode is used for energy measurement instead of the divided outer electrodes, so that Compton scattering events in adjacent segments are collected.

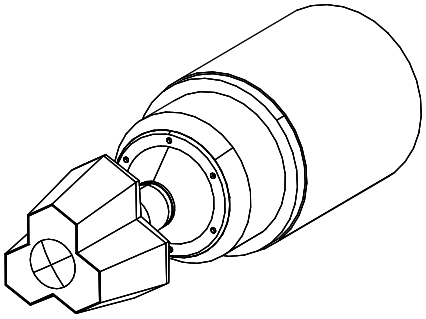

Figure 2.7: Exterior of the Miniball detector.

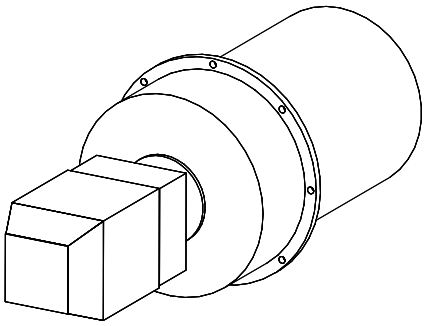

Figure 2.8: Exterior of the Clover detector.

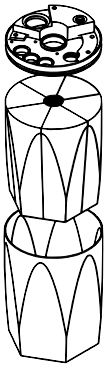

Figure 2.9: The crystal of the Miniball detector is divided into six parts in the circumferential direction. The figure is a modified version of the one in [42].

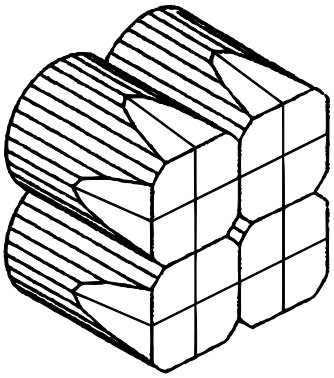

Figure 2.10: The crystal of the Clover detector is divided into four parts. The figure is a modified version of that in [43].

2.8.3 Gamma-ray tracking detector (RCNP Quad, LBNL P3)

RCNP Quad and LBNL P3 are gamma-ray tracking detectors that can determine the interaction position inside the crystal by waveform analysis. Originally, they were developed to track Compton scattering that occurs multiple times within the crystal, to distinguish whether it is a total energy absorption event or a background event that deviates outside the detector after Compton scattering, and to reduce the background ratio. In this study, the high resolution of the interaction position can improve the accuracy of gamma-ray emission angle determination compared to conventional Ge detectors. Finally, this leads to improved energy resolution after Doppler shift correction. Next, we will explain the principle of interaction position derivation in the gamma-ray tracking detector. As shown in Figure 2.13, the Ge crystal of the detector has an outer electrode divided into six parts in the circumferential and axial directions, for a total of 36 parts, and the signal from each electrode is read out. When a gamma ray interacts at a certain point in the crystal, it generates a number of electron-hole pairs proportional to the energy transferred at

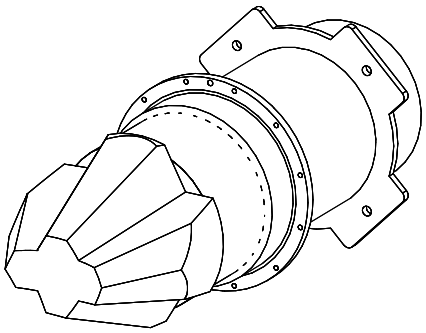

Figure 2.11: Appearance of the RCNP Quad detector.

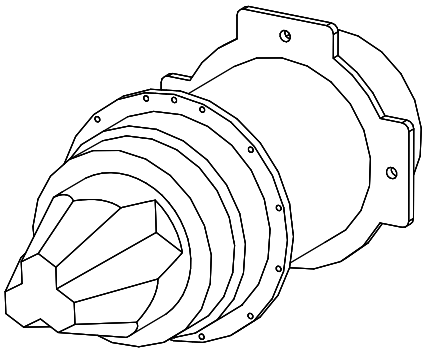

Figure 2.12: Appearance of the LBNL P3 detector.

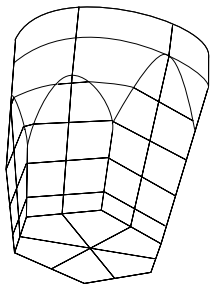

Figure 2.13: The crystals of RCNP Quad and LBNL P3 have the same design. The crystal's readout electrode is divided into 6 parts in the circumferential direction and 6 parts in the axial direction, for a total of 36 parts. The figure is a modified version of [44].

that location, and the electrons are attracted to the inner electrode and the holes to the outer electrode according to the applied electric field. A finite amount of charge is transferred to only one specific outer electrode corresponding to the interaction position. At this point, the interaction position can be narrowed down to $1/36$ of the entire crystal depending on which electrode in the crystal it is adsorbed to.

Then, waveform analysis is performed to further improve the position resolution. The radial position appears as the slope of the waveform due to the difference in the moving velocity of electrons and holes. The circumferential and axial directions appear in the waveform of adjacent electrodes, as shown in Figure 2.14.

The method for deriving the interaction position from the waveform is to prepare a data set of interaction points and waveforms generated by simulation at every point in the crystal, and perform chi-square fitting to the actual measured waveform to find an interaction point that shows a similar waveform. The interaction position is determined by taking a weighted average of several points with small chi-square values.

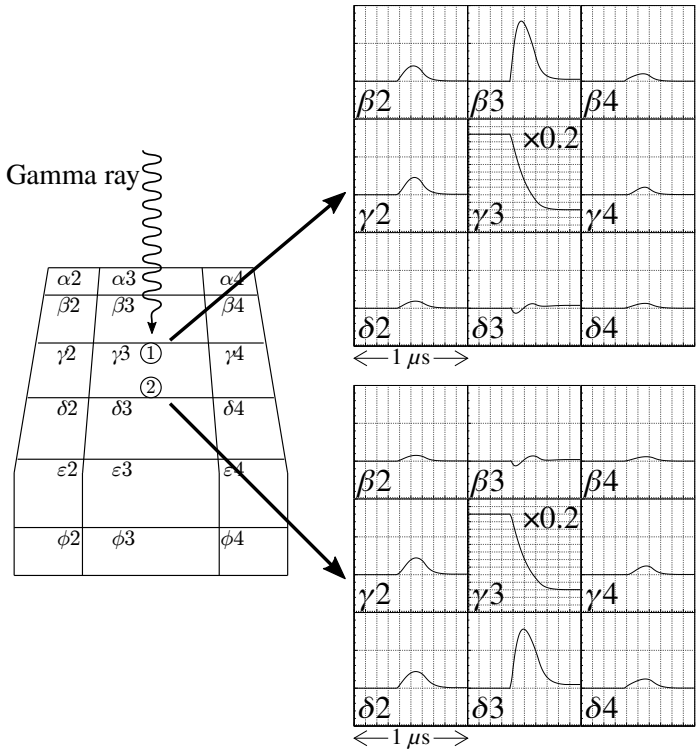

Figure 2.14: Difference in waveform depending on interaction point. In the schematic diagram of the Ge crystal on the left, the waveform output of each electrode when interacting at positions ① and ② is shown on the right. The diagram of the waveform output of each electrode shows the electrode $\gamma 3$ where energy was actually applied and the adjacent electrodes ($\beta 2$ - $\beta 4$, $\gamma 2$, $\gamma 4$, $\delta 2$ - $\delta 4$). When ①, the interaction position is closer to $\beta 3$, so the waveform height that appears at $\beta 3$ is larger. Similarly, in the case of ②, the wave height of $\delta 3$ becomes higher.

Using this method, it is possible to determine the position in three dimensions with high accuracy within the Ge crystal. Regarding RCNP Quad, our measurements [37] have shown that the x, y, and z directions can be determined with an accuracy of less than 2 mm (FWHM).

2.8.4 Recovery of unreadable crystal segments

The non-tracking detectors Miniball and Clover contained crystals containing some unreadable electrodes. As mentioned above, it is important to know which electrode absorbed the hole in order to identify the range of the gamma-ray interaction position by the electrode where the signal was induced and to use it for Doppler shift correction.

Fortunately, all crystals contained only one unreadable electrode, so the amount of energy deposition E_{B} by the missing electrode could be obtained using the value E_i of the other electrodes, and was obtained as follows:

$$E_{\mathrm{B}} = E_{\mathrm{CC}} - \sum_{i \neq \mathrm{B}} E_i \tag{2.22}$$

Here, E_{CC} is the amount of energy deposition by the central contact, which is sensitive to the energy deposition of the entire crystal, unlike the outer electrodes, which are divided into electrodes. In other words, if there are no broken crystals,

$$E_{\mathrm{CC}} = \sum_{i} E_i \tag{2.23}$$

should be true.

The unreadable electrodes of each detector are summarized in Table 2.2.

Table 2.2: List of HiCARI detectors. The number in parentheses next to the number of crystals is the number of valid crystals excluding broken ones.

Name	ID	Number of Crystals	Installation Position			Note
			r (mm)	θ (deg)	ϕ (deg)	
Minball0	0	3 (2)	270	45	-120	Cry.#2 broken
Minball1	1	3 (2)	270	45	-60	Cry.#0 broken
Minball2	2	3	280	30	180	Seg.#2 of Cry.#1 broken
Minball3	3	3	280	30	0	Seg.#4 of Cry.#1 broken
Minball4	4	3	275	45	120	Seg.#3 of Cry.#2 broken
Minball5	5	3	275	45	60	Seg.#4 of Cry.#2 broken
Clover0	6	4	300	75	-135	Seg.#3 of Cry.#3 broken
Clover1	7	4	300	75	-45	
Clover2	8	4	300	75	135	Seg.#2 of Cry.#2 broken
Clover3	9	4	270	75	45	Seg.#2 of Cry.#3 broken
Quad	10	4 (2)	195	75	180	Cry.#0,3 broken
P3	11	3	175	75	0	

2.9 Data acquisition system

There are two data acquisition systems in this study.

- Beam line DAQ
- HiCARI DAQ

Beam line DAQ is the standard DAQ used at RIBF [45–49], and was used to collect data from the beamline detectors installed at BigRIPS and ZeroDegree. HiCARI DAQ is the DAQ used to collect data from the Ge detectors that make up the HiCARI array, and is a DAQ [50] developed by the US gamma-ray tracking detector GRETINA development group adjusted for the RIBF experiment. The HiCARI DAQ hardware and software were introduced for the first time to the RIBF experiment for the HiCARI collaboration campaign. The circuit uses a digitizer (GRETINA Digitizer [51]) designed to acquire the waveform of the signal from the tracking detector. This digitizer is equipped with a 14 bit 100 MHz flash ADC that digitizes the pulse height per time, and an FPGA, which has an energy detection function using a trapezoidal filter and a timing detection function. The digitizer is inserted into a dedicated VME crate together with an IOC that controls the four digitizers. The data flow is that the analog output signal from the detector is directly input to the digitizer through a cable and A/D converted. Four digitizers are used per crystal for tracking detectors that acquire waveforms (RCNP Quad and LBNL P3), and one digitizer is used per crystal for non-tracking detectors that do not acquire waveforms (Miniball, Clover). The digital signal from the digitizer is sent to the analysis server [52] via an Ethernet cable from the IOC. The analysis server analyzes the waveform online and derives the interaction position inside the crystal of the tracking detector. The raw data sent from the digitizer and the interaction position data obtained by online analysis are then both written to the hard disk. Triggers are generated by processing the signals from both the Beam line DAQ and the HiCARI DAQ using GTO (General Trigger Operator), and distributed to each DAQ system to be used as triggers.

In addition, timestamp information created by a timestamp generation module named MyRIAD [53] is sent to each DAQ, making it possible to integrate the data acquired independently by the two types of DAQ after the experiment.

2.10 HiCARI(2) – Energy calibration, resolution, and efficiency

2.10.1 Energy calibration

Energy calibration was performed by setting appropriate conversion functions for all 12 detectors, 37 crystals, and 389 electrodes so that the raw energy values obtained from the digitizer could be expressed in energy keV units.

Assuming that a linear function relationship exists between the value obtained from the digitizer E_{raw} and the energy value E_{keV} expressed in keV units after calibration, taking into account the offset, we determined P_1, P_2 for each electrode, where

$$E_{\mathrm{keV}} = P_1 \cdot E_{\mathrm{raw}} + P_2 \tag{2.24}$$

by using free parameters P_1, P_2.

The procedure is to first roughly align using a ^{60}Co source. ^{60}Co emits two types of gamma rays, 1332.5 keV and 1173.2 keV. When this is measured with a Ge detector, two peaks appear, so we assume that the larger one is 1332.5 keV and the smaller one is 1173.2 keV, and find P_1, P_2 from the channel numbers of the respective peak positions. Since both the variable and the number of samples are 2, P_1, P_2 are uniquely determined. However, it is not possible to evaluate the error at all. Next, we look at the measurement data for ^{152}Eu. Because ^{152}Eu emits many types of gamma rays, it is difficult to tell at first glance which peak corresponds to which energy. Therefore, we perform a provisional calibration using P_1, P_2 found

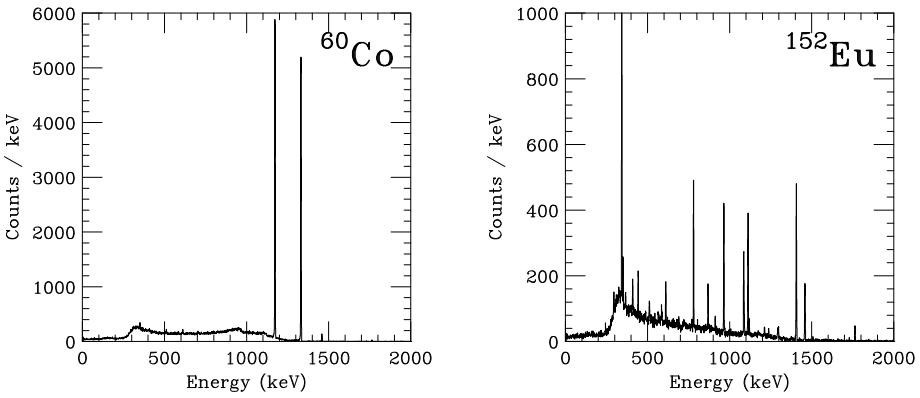

Figure 2.15: Measurement results for a ^{60}Co source (left) and a ^{152}Eu source (right). The horizontal axis of both plots is calibrated and in units of energy (keV).

with ^{60}Co. This results in a peak close to the actual gamma-ray energy of ^{152}Eu, making the correspondence between the peak and the energy clear. Of the gamma rays emitted by ^{152}Eu, eight types with high branching ratios were used for this calibration work. These are summarized in Table 2.3.

The peak position was derived by fitting with a function. Assuming that the background component is a straight line and the true peak shape is a Gaussian function, fitting was performed with

$$y = P_1 \exp\left[-\frac{1}{2}\left(\frac{x - P_2}{P_3}\right)^2\right] + P_4 x + P_5 \tag{2.25}$$

In this equation, P_2 corresponds to the peak center position. The resolution σ, which will be described later, is P_3.

Table 2.3: Gamma-ray energy and branching ratio of ^{152}Eu used to derive the efficiency.

Energy (keV)	I_γ (%)
121.782	28.58
244.697	7.583
344.279	26.5
778.904	12.942
964.079	14.605
1112.07	13.644
1408.01	21.005

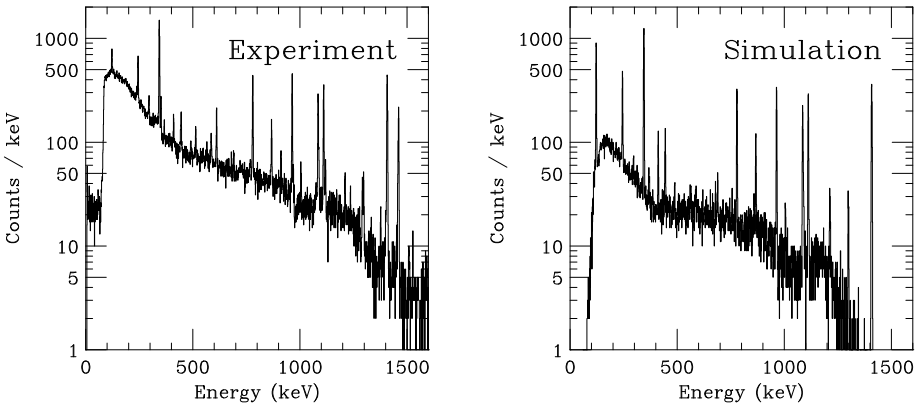

Figure 2.16: Measurement results (left) and simulation (right) of the ^{152}Eu source at crystal 1 of Miniball 1. There is a missing segment and the resolution is poor. The simulation takes into account the source energy, branching ratio, radioactivity, measurement time, the source position and detector installation position, the material between the source and detector, and the resolution characteristics of the detector.

2.10.2 Energy resolution

Assuming that the resolution σ_E of the Ge detector is a function of E,

$$\sigma_E = A\sqrt{1 + E \cdot B} \tag{2.26}$$

we investigated the multiple peak widths obtained by measuring the ^{152}Eu source for each crystal, fitted the energy dependence of the peak widths with the above equation, and obtained A and B for all crystals.

2.10.3 Position resolution

The resolution of gamma-ray detection position σ_x is approximately 2 mm at RCNP Quad.[37] LBNL P3 is thought to have a similar resolution. Since the

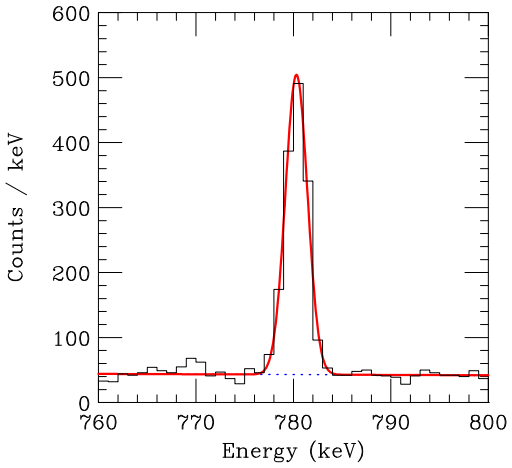

Figure 2.17: The fitting was performed using a Gaussian function + straight line, with the background represented as a straight line (blue dotted line).

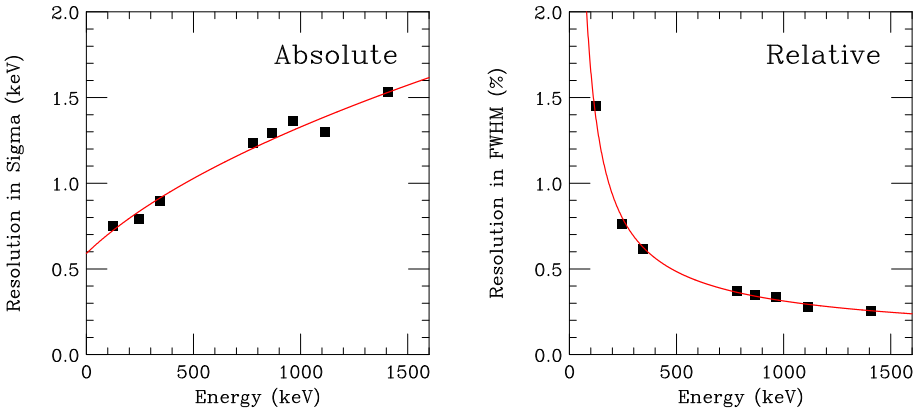

Figure 2.18: An example of the energy dependence of energy resolution. Measured values (black squares) and a curve (red solid line) fitting the measured values with the equation 2.26.

detection position within a segment is unknown for Non-Tracking detectors, if the position resolution is set to half the distance between neighboring segments, it is 11 mm for Miniball and 13 mm for Clover.

Taking these factors into consideration, the angular resolution σ_θ can be calculated from the detector's distance r from the target, as shown in Table 2.4.

Table 2.4: Angular resolutions of each detectors.

	r [mm]	σ_x [mm]	σ_θ [deg]
Miniball	275	11	2.3
Clover	300	13	2.5
RCNP Quad	195	2	0.6
LBNL P3	175	2	0.7

2.10.4 Detection efficiency

The detection efficiency was also obtained using the measurement data of ^{152}Euused for calibration. The relevant measurement information is summarized in the table below.

The number of gamma-ray emissions $N_{\text{emitted}}(E)$ can be calculated by multiplying the total number of decays by the relative intensity $I_\gamma(E)$ for each gamma-ray energy in table 2.3.

$$N_{\text{emitted}}(E) = N_{\text{decay}} \cdot I_\gamma(E) \tag{2.27}$$

The definition of detection efficiency here is "the efficiency with which a detector can detect gamma rays emitted from a target position." This includes various factors such as the detector's intrinsic detection performance, the detector's placement relative to the target position, and the absorption of gamma rays by shielding. The detection efficiency ε is defined as follows:

$$\varepsilon = \frac{N_{\text{Detected}}}{N_{\text{Emitted}}} \tag{2.28}$$

Since this depends on the gamma ray energy E, it is obtained for each energy of the peak of ^{152}Eu. Also, since the detector characteristics and the distance from the target differ between tracking and non-tracking detectors, the efficiency was obtained separately.

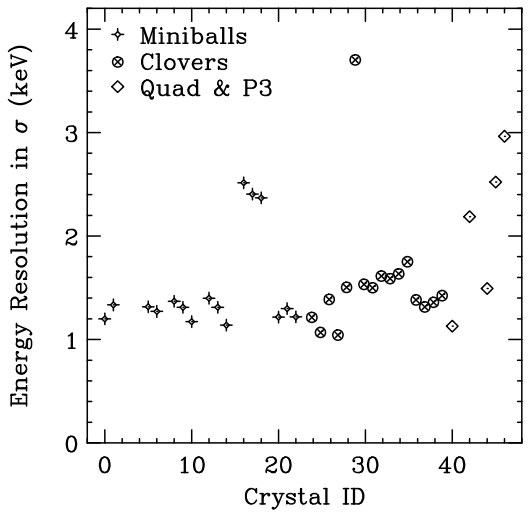

Figure 2.19: Intrinsic energy resolution of each Ge crystal. These values were calculated from the formula (2.26) for $E = 1000$ keV.

Table 2.5: Efficiency measurement summary

Run	Source*1)	Activity [Bq]*2)	Time [sec]*3)	Total Decay
751	^{152}Eu (09-7011)	6134(117)	2021.50	$1.240(24) \times 10^7$
761	^{152}Eu (09-7011)	6129(116)	1819.16	$1.115(21) \times 10^7$
752	^{60}Co (09-7008)	21500(344)	1372.09	$2.950(47) \times 10^7$
759	^{60}Co (09-7008)	21458(343)	1331.94	$2.858(46) \times 10^7$

*1)The number in parentheses in the lower row is the source management number within the RIKEN Nishina Center.

*2)The radioactivity and precision of the source on a specific day can be obtained using [54].

*3)The start/end times in the upper row are visually confirmed as the time the DAQ Start/Stop button was pressed, and the measurement times in the lower row are calculated from the timestamp included in the measurement data. Note that there is no record of the end time of Run 761.

2.11 HiCARI (3) – Simulation of radiation source measurement

2.11.1 Reproduction of the HiCARI array

The simulation was performed using "UCHiCARI", which is based on the Geant4 [55] simulation package UCGretina [56] developed by the GRETINA [44,57] experimental group and is optimized for the HiCARI experiment.

Survey markers were placed on the surfaces of the laboratory equipment, such as the detectors and beam pipes that make up the HiCARI array installed in the laboratory, and the marker position coordinates were obtained by photogrammetry. The HiCARI array was reproduced in the simulation space by comparing it with the detector drawing. The visualization of this is shown in Figure 2.20.

2.11.2 Correction of energy resolution and detection efficiency for each crystal

In section 2.10, the energy resolution and detection efficiency for each crystal were obtained by measurements using a ^{152}Eusource. In the simulation, to confirm the more detailed energy dependence, a virtual gamma-ray source of 80 - 3000 keV was placed at the target position in the beam pipe and a gamma-ray spectrum was created. Adjustments were made for each crystal so that the energy resolution and detection efficiency would reproduce the performance of the actual HiCARI array.

2.11.3 Relative detection efficiency

In the simulation, adjustments were made to reproduce the detection efficiency of the HiCARI array as much as possible, but to evaluate the difference and error

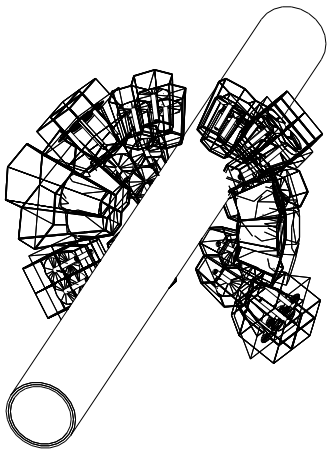

Figure 2.20: The HiCARI array and beam pipes reproduced in the simulation space. Only the crystals in the HiCARI array are shown.

in the detection efficiency with the actual HiCARI array, the detection efficiency of the entire non-tracking detector and the entire tracking detector are compared between reality and simulation. Here, when the experimental value of the detection efficiency is $\mathfrak{E}_{\mathrm{exp}}$ and the simulation value is $\mathfrak{E}_{\mathrm{sim}}$, we determine the relative detection efficiency $\varepsilon_{\mathrm{sim}}$ that satisfies :

$$\mathfrak{E}_{\mathrm{exp}} = \mathfrak{E}_{\mathrm{sim}} \cdot \varepsilon_{\mathrm{sim}} \tag{2.29}$$

For the entire non-tracking detector and the entire tracking detector, the relative detection efficiency $\varepsilon_{\mathrm{sim}}$ was determined using the experimental values of the detection efficiency at four points (779, 964, 1112, 1408 keV) obtained in the measurement of ^{152}Eu.

$$\varepsilon_{\mathrm{sim}}(\text{Non-Tracking}) = 0.96(6) \tag{2.30}$$

$$\varepsilon_{\mathrm{sim}}(\text{Tracking}) = 0.95(9) \tag{2.31}$$

The reason for selecting these four points is that they are important energy regions for the experiments performed in this study, and also because the branching ratio of the decay of ^{152}Eu is large, and a relatively large number of statistics can be obtained.

In addition, the efficiency curve of the simulation corrected by applying the relative detection efficiency $\varepsilon_{\mathrm{sim}}$ is shown in Figure 2.21 overlapped with the experimental value.

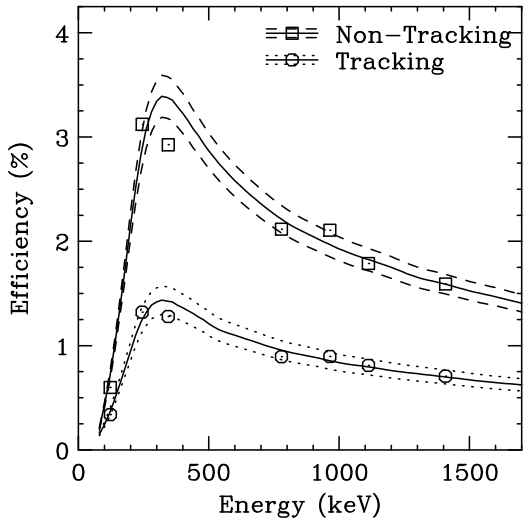

Figure 2.21: Circles and squares are experimental values with a ^{152}Eusource, and the solid line is the detection efficiency by simulation. The simulation is scaled with $\varepsilon_{\mathrm{sim}}$ to reproduce the experimental value, and the error range is shown by the dotted and dashed lines.

Chapter 3

Data Analysis (I)

3.1 List of acquired data and experimental conditions

In this study, data were acquired using four different experimental setups with different beam settings and targets. These are summarized in table 3.1.

The nuclides listed as "secondary beam" in the table are those selected as the main targets for measurement among the various nuclear fragment nuclides produced by injecting the primary beam into the product target at the F0 focal plane, and the magnetic field is set so that these nuclides are aligned with the central trajectory of the beamline. Additionally, the energy value is the energy at the center of the secondary target estimated from measurements and derivation of energy loss. In this thesis, only the experimental data with the Au target was used in the subsequent analysis.

Table 3.1: List of experimental conditions.

Run No.	Primary Beam	Secondary Beam	Target	Time(hour)
005 - 018	^{70}Zn (345 MeV/u)	^{56}Ti (176 MeV/u)	Be	11.7
021 - 037	^{70}Zn (345 MeV/u)	^{56}Ti (164 MeV/u)	Au	12.0
041 - 079	^{70}Zn (345 MeV/u)	^{58}Ti (170 MeV/u)	Au	29.6
085 - 121	^{70}Zn (345 MeV/u)	^{58}Ti (181 MeV/u)	Be	27.8

3.2 Analysis strategy

The experimental purpose of this study is to derive $B(\mathrm{E2})$ for ^{56}Ti and ^{58}Ti, but we first derive the Coulomb excitation cross section required for obtaining $B(\mathrm{E2})$. To derive the Coulomb excitation cross section, three things are required:

- Number of incident beam particles
- Target Thickness
- Number of gamma rays emitted by Coulomb excitation

For the first item, to count the number of incident beam particles, particle identification is performed by analyzing the beamline detector to determine the number of events that should be counted as the number of incident particles. At the same time, in order to reduce uncertainty in the subsequent cross section derivation, events that may contribute to the background are removed and only "events with good properties" are carefully selected here.

For the second item, in this study, the target thickness was obtained from the energy loss of the beam particles. Therefore, this is done simultaneously with the analysis of the beamline detector.

For the third item, the number of gamma rays emitted by Coulomb excitation is counted by analyzing the gamma rays detected by the HiCARI array. To identify the particle that originated the gamma rays and to correct the Doppler shift of the gamma rays, the results are combined with information obtained from the beamline detector.

Both the number of incident beam particles and that of gamma rays need to be corrected for detection efficiency, etc., and this derivation will be performed later. Once these values are gathered, the cross-sectional area can be obtained; the derivation method will be described in section 5.8.

Chapter 4

Data Analysis (II) – Beamline Detectors

4.1 Beamline detector analysis

In this chapter, we begin the analysis of the beamline detectors. Here, the objective is to analyze the motion state of the beam particles from the detector, identify the particles, and count the number of ^{56}Ti and ^{58}Ti incident beams. At the same time, it is also necessary to carefully select only "good condition" events with high beam purity and high transmission rate at the final focal plane F11, and to minimize the uncertainty of the yield in the subsequent gamma ray analysis. Finally, we set cut conditions to leave only good condition events, and count the number of beam particles that satisfy them. To achieve this, we will proceed with the analysis according to the following procedure.

First, in section 4.2, we check the trigger conditions for data acquisition and derive the total beam counts. Next, in section 4.3, we identify particles and select the ^{56}Ti and ^{58}Ti beams. Then, in sections 4.4 - 4.6, we describe the “Good Condition” range setting, the results of its application, and the “Good Condition” beam count. Finally, in sections 4.8 - 4.11, we analyze the beam profile required for subsequent analysis.

4.2 Data acquisition trigger and total beam counts

4.2.1 Trigger signal and data acquisition conditions

The trigger signal is managed by the GTO. The trigger signals input to the GTO are as follows:

- DSF7 : F7 Plastic signal passed through a downscaler
- F7 $\otimes$ F11 : Coincidence of F7 and F11 Plastic signals
- HiCARI : Signal from any detector in the HiCARI array
- Clock : 1000 Hz oscillation signal

These trigger signals are used to generate data acquisition conditions. The data will be collected when one of the following two conditions is met:

- F7 $\otimes$ F11 $\otimes$ HiCARI
- DSF7

This means that data is not acquired on all detected beam particles. The total beam count is obtained by multiplying the DSF7 signal by the downscale factor (DSF).

4.2.2 Downscale factor

When the downscaler is set to a downscale factor of N, it generates a signal once every N times. Let N be called $\mathrm{DSF_{set}}$. However, in reality, the downscale factor may not operate strictly as specified. The actual downscale factor that operates on average across all measurements obtained from the acquired data can be calculated by defining $\mathrm{DSF_{mes}}$ as follows:

$$\mathrm{DSF_{mes}} = \frac{N_{\mathrm{F7\otimes F11\otimes HiCARI}}}{N_{\mathrm{F7\otimes F11\otimes HiCARI\otimes DSF7}}} \tag{4.1}$$

Here, N in the formula is the number of events that satisfy the subscript condition. The $\mathrm{DSF_{mes}}$ obtained in this way is summarized in Table 4.1.

Table 4.1: Derivation of the measured downscaling factor $\mathrm{DSF_{mes}}$.

	^{197}Au(^{56}Ti,^{56}Ti)	^{197}Au(^{58}Ti,^{58}Ti)
$\mathrm{DSF_{set}}$	20	20
$N_{\mathrm{F7\otimes F11\otimes HiCARI}}$	19131921	69596930
$N_{\mathrm{F7\otimes F11\otimes HiCARI\otimes DSF7}}$	985836	3586759
$\mathrm{DSF_{mes}}$	19.4068	19.4038

4.2.3 Total beam counts at F7

Using $\mathrm{DSF_{mes}}$ and the number of triggers for the DSF7 signal, N_{DSF7}, the number of times that F7 Plastic emitted a signal, i.e., the number of beam particles that passed through the F7 focal plane, N_{F7}, can be calculated as follows:

$$N_{\mathrm{F7}} = N_{\mathrm{DSF7}} \cdot \mathrm{DSF_{mes}} \tag{4.2}$$

The resulting N_{F7} is shown in Table 4.2. From now on, the value of $\mathrm{DSF_{mes}}$ will be written as DSF with the subscript omitted.

Table 4.2: N_{F7} is calculated from the number of DSF7 triggers N_{DSF7}. The trigger rate calculated from the measurement time in Table 3.1 is also shown in parentheses.

	^{197}Au(^{56}Ti,^{56}Ti)	^{197}Au(^{58}Ti,^{58}Ti)
N_{DSF7}	13505418	44349237
N_{F7} (Calculated)	2.62097×10^8 (8064 cnt/sec)	8.60546×10^8 (8172 cnt/sec)

4.3 Particle Identification

As mentioned in Section 2.5, the BigRIPS / ZeroDegree detector group can be used to apply the $B\rho$-ΔE-TOF method to obtain the Z and A/Q for each beam particle. Figure 4.1 shows the particle identification results for BigRIPS and ZeroDegree in measurements with the secondary beam center at ^{56}Ti. In this figure, by using only events inside the region obtained by applying restrictions to Z and A/Q, events with identified incident and emitted particles can be obtained.

4.3.1 Background removal

For the background removal method of BigRiPS and ZeroDegree, we referred to the reference [32].

In conclusion, the amount of background that can be removed by this method is already sufficiently small, and the accuracy of particle separation is good, so the results of only the background removal method using PPAC time sum analysis are used in the subsequent analysis.

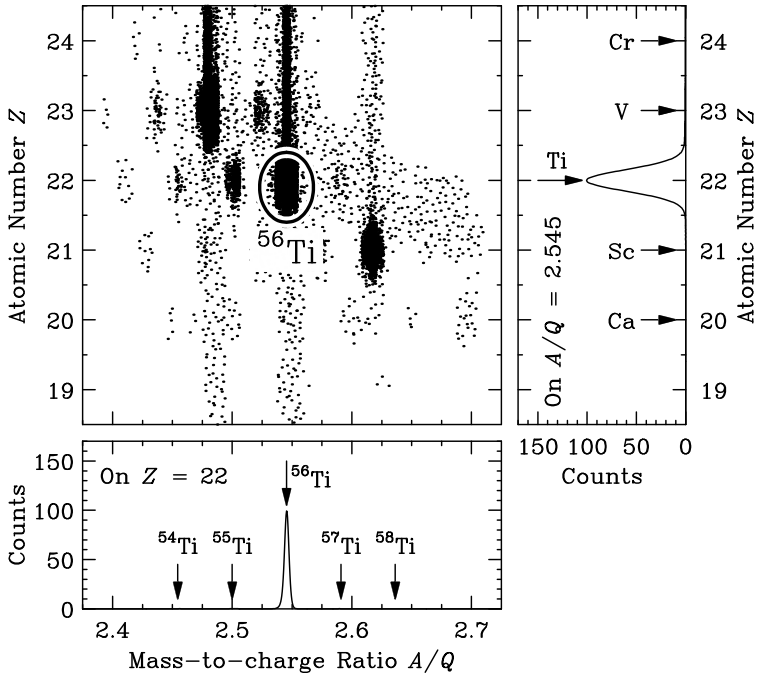

Figure 4.1: Points are plotted by Z and A/Q for each particle in BigRIPS and ZeroDegree. The points surrounded by the ellipse are the beam particles identified as ^{56}Ti. At ZeroDegree, downstream of the secondary target, it can be seen that many types of particles are produced by nuclear reactions.

4.3.2 TOF offset correction for A/Q calibration

In the previous section, we performed particle identification using BigRIPS / ZeroDegree, but before that, we actually performed TOF offset correction to accurately derive A/Q.

TOF measurements have an offset that varies depending on the laboratory environment, and analysis using measurements that deviate from the true TOF due to this offset fluctuation affects the β and A/Q calculated from them. From equation (2.10),

$$A/Q \propto \frac{1}{\beta\gamma} \tag{4.3}$$

and considering that $\beta \propto 1/\mathrm{TOF}$,

$$A/Q \propto \mathrm{TOF} \tag{4.4}$$

holds in the range of $\beta \ll 1$.

From this, the fluctuations of TOF are propagated to A/Q with the same scale.

The TOF offset correction method was to first create a particle identification diagram using a TOF offset value known empirically, check how far the A/Q peak position is from the "correct" position, and then fine-tune the TOF offset value so that the A/Q peak is at the "correct" position.

With this method, there is a risk of misidentifying and matching peaks from

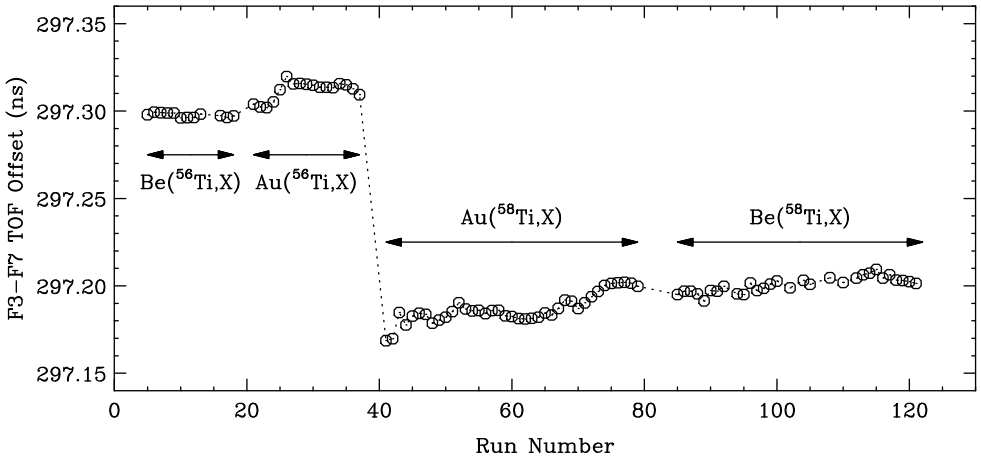

Figure 4.2: The variation of the optimized TOF offset value. The horizontal axis is the run number. Beam switching was performed in Run 40 (changing the central orbit from ^{56}Ti to ^{58}Ti), so there is a discontinuous change before and after. TOF measurements were performed at six locations: F3-F5, F5-F7, F3-F7, F8-F9, F9-F11, and F8-F11, and corrections were performed for each. The offset value shown here is for F3-F7.

different nuclides, but if a mistake is made, the energy of the emitted gamma rays will be different, so it will be possible to notice during subsequent analysis.

The experimental data was acquired in separate runs, which consisted of measurement data for up to one hour, and the TOF offset value was determined for each run. Figure 4.2 shows the fluctuations in the TOF offset value after correction.

4.3.3 Selection of specific particles and particle separation accuracy

For a specific particle, for example, ^{56}Ti, the points in the vicinity of $(A/Q, Z) = (2.55, 22)$ in the particle identification diagram are ^{56}Ti. To determine how far from the center of these points we should include as ^{56}Ti events, we create the Z-axis projection of the points in the vicinity of $A/Q = 2.55$ and the A/Q-axis projection of the points in the vicinity of $Z = 22$, as shown in Figure 4.1. The interval where each is fitted with a Gaussian function and becomes 2σ is treated as ^{56}Ti. The peak width is more than 5σ away from the neighboring nuclei for both A/Q and Z, so the separation accuracy is sufficiently good, and the peaks of the neighboring nuclei are small to begin with. Therefore, the intensity of mixing from the surrounding nuclei is sufficiently weak that the background component can be neglected.

4.3.4 Particle-identified beam counts

Table 4.3: Counts of PI Beam

	^{197}Au(^{56}Ti,^{56}Ti)	^{197}Au(^{58}Ti,^{58}Ti)
$N_{\mathrm{PI}\otimes\mathrm{DSF7}}$	8942401	7139264
N_{PI} (Calculated)	1.7354339×10^8 (5339 cnt/sec)	1.3852885×10^8 (1316 cnt/sec)

4.4 “Good Condition Beam” and acattering angle acceptance (1)

4.4.1 Unavailable beam particles

The number of beam particles is counted using the F7 plastic detector upstream of the target, but it is necessary to consider beam particles that do not reach the F11 plastic detector at the most downstream. This is because particle identification is cut off at the downstream ZeroDegree, and events that could not be identified due to not reaching F11 are counted and treated as "events that did not react" regardless of whether gamma rays are emitted or not. The probability that a beam particle can reach the F11 plastic detector at the most downstream is called acceptance, and the gamma ray yield to be analyzed later must be corrected by acceptance. The main reasons for not reaching F11 are considered to be :

(i) Bad initial beam conditions (position, angle, momentum)
(ii) Large angle scattering at the target

Of these, we took measures against (i) and made the acceptance dependent only on the scattering angle by carefully selecting and using only "beams with good properties" that can always reach F11 in the range where the scattering angle at the target can be considered to be almost 0.

4.4.2 “Good Condition Beam” selection

The quality of the beam was determined by restricting the position coordinates x, y[*1)] on the target and the momentum δ at F5-F7. The investigation of the beam quality performed to determine this and the specific method for determining the restriction range are described in the next section 4.5. Within this restriction range, the transmission rate at the F11 focal plane is 99.6 % or more when the scattering angle at the target can be considered to be almost 0.

*1) x, y on the target are determined by extrapolation from two double PPACs located at the upstream F7 focal plane.

4.5 Kinematical profile of beam particle

4.5.1 Transport efficiencyτ

The condition for acquiring gamma-ray data is that both BR and ZD have ^{56}Ti or ^{58}Ti. In other words, even if the target is excited by Coulomb, events that do not reach the F11 focal plane and cannot be correctly PIed by ZD are counted out. Here, we consider the transmission efficiency τ, which is the efficiency with which nuclei emitted from the target reach the F11 focal plane. First, we define the transmission efficiency τ as the number of nuclei emitted from the target N_{out} and the number of nuclei detected (by correct particle identification) by the ZeroDegree spectrometer N_{det}, as follows:

$$\tau = \frac{N_{\mathrm{det}}}{N_{\mathrm{out}}} \tag{4.5}$$

Here, the ZD detection efficiency τ can be roughly decomposed into the following three components. These are the transport efficiency $\varepsilon_{\mathrm{trans}}$, which is the efficiency by which an emitted particle passes through the ZeroDegree spectrometer to the end and reaches the F11 focal plane; the non-reaction rate $\varepsilon_{\mathrm{noreac}}$, which is the rate at which a particle remains the same nuclide without undergoing a nuclear reaction from the time it passes the target to the F11 focal plane; and the particle identification efficiency $\varepsilon_{\mathrm{PI}}$, which is the efficiency by which the ZD detector operates without problems and correctly identifies particles. The ZD detection efficiency τ is given by these products,

$$\tau = \varepsilon_{\mathrm{trans}} \cdot \varepsilon_{\mathrm{noreac}} \cdot \varepsilon_{\mathrm{PI}} \tag{4.6}$$

Here, the non-reaction rate $\varepsilon_{\mathrm{noreac}}$ is 99 % or more, so it can be considered to be approximately 1. $\varepsilon_{\mathrm{trans}}$ and $\varepsilon_{\mathrm{PI}}$ can be distinguished only by whether or not the F11 focal plane has been reached, and can be expressed as

$$\varepsilon_{\mathrm{trans}} = \frac{N_{\mathrm{F11}}}{N_{\mathrm{out}}},\ \varepsilon_{\mathrm{PI}} = \frac{N_{\mathrm{det}}}{N_{\mathrm{F11}}} \tag{4.7}$$

If the settings of the beamline detector and magnetic field do not change during the experiment, the transport efficiency is basically determined only by the state of motion immediately after extraction. This is called $\varepsilon_{\mathrm{trans}}$. The state of motion immediately after extraction is given as $(x, y, \theta_x, \theta_y, \delta)$, which we will denote as $\varepsilon_{\mathrm{trans}}(x, y, \theta_x, \theta_y, \delta)$. Even if the state of motion immediately after extraction is

good, if a nuclear reaction occurs during the ZD spectrometer and the nuclide changes to another species, it may deviate from the correct orbit and not be able to reach F11. Therefore, the probability that the same nuclide will remain without a nuclear reaction from just after the target to F11 is called $\varepsilon_{\mathrm{noreac}}$. In addition, even if F11 is reached, PI may not be performed correctly due to problems on the ZD detector side. Therefore, if $\varepsilon_{\mathrm{PI}}$ is the percentage of correct PI when there are no problems with particle transport, then τ is:

$$\tau = \varepsilon_{\mathrm{trans}}(x, y, \theta_x, \theta_y, \delta) \cdot \varepsilon_{\mathrm{noreac}} \cdot \varepsilon_{\mathrm{PI}} \tag{4.8}$$

We assume that $\varepsilon_{\mathrm{noreac}}$ and $\varepsilon_{\mathrm{PI}}$ have little dependence on the particle's motion state, and first consider $\varepsilon_{\mathrm{trans}}(x, y, \theta_x, \theta_y, \delta)$.

4.5.2 Momentum acceptance $\varepsilon_{\mathrm{trans}}(\delta)$

If we assume that $\varepsilon_{\mathrm{trans}}(x, y, \theta_x, \theta_y, \delta)$ is independent of each variable, then we can write it as the product of the transport efficiencies for each variable:

$$\varepsilon_{\mathrm{trans}}(x, y, \theta_x, \theta_y, \delta) = \varepsilon(x) \cdot \varepsilon(y) \cdot \varepsilon(\theta_x) \cdot \varepsilon(\theta_y) \cdot \varepsilon(\delta) \tag{4.9}$$

Also, based on the beamline design and magnetic field settings, it should be

$$\varepsilon_{\mathrm{trans}}(0, 0, 0, 0, 0) = 1 \tag{4.10}$$

If equations (4.9) and (4.10) hold, the component of the transport efficiency that depends on the relative momentum δ, $\varepsilon_{\mathrm{trans}}(\delta)$, can be considered as

$$\varepsilon_{\mathrm{trans}}(\delta) = \varepsilon_{\mathrm{trans}}(0, 0, 0, 0, \delta) \tag{4.11}$$

To evaluate this, apply a gate so that $x = 0,\ y = 0,\ \theta_x = 0,\ \theta_y = 0$, and evaluate the rate of transmission at F11 for each momentum δ.

For momentum δ, we use the measurement value $\delta_{\mathrm{F5-F7}}$ before the target. The reason for this is that if we use the measurement value after the target, only events that reach the F9 focal plane after passing the target will be selected, and it will be impossible to evaluate the number of events that have been lost up to that point.

Figure4.3 (a) and (b) show the momentum δ distribution gated so that $x = 0,\ y = 0,\ \theta_x = 0,\ \theta_y = 0$, and the $\varepsilon_{\mathrm{trans}}(\delta)$ obtained from it. In (b), the transmission rate (i.e., $\varepsilon_{\mathrm{trans}}(\delta)$) was calculated by dividing by the number of counts including the F11 Plastic trigger signal in (a). The error was calculated assuming a binomial

distribution, and a Laplace correction[*1)] was performed so that the calculation would be correct even when the number of counts was small. $\varepsilon_{\mathrm{trans}}(\delta)$ was fitted with the following function, which smoothly connects both ends of the window function with an error function (integral of a Gaussian function) to make it easier to handle in later analysis:

$$f(x) = C\left\{\frac{1}{2}\left[1+\mathrm{erf}\left(\frac{x-\mu_L}{\sqrt{2}\,\sigma_L}\right)\right]\cdot\frac{1}{2}\left[1-\mathrm{erf}\left(\frac{x-\mu_R}{\sqrt{2}\,\sigma_R}\right)\right]\right\} \tag{4.12}$$

$$\mathrm{erf}(x) = \frac{2}{\sqrt{\pi}}\int_0^x e^{-t^2}\,dt \quad (-\infty < x < \infty) \tag{4.13}$$

This function will be called the "smoothing window function."

As a result of the fitting, the parameter C, which represents the height scale, should essentially be exactly 1, but in reality it is around 0.99. This is due to the influence of not only $\varepsilon_{\mathrm{trans}}(\delta)$ but also $\varepsilon_{\mathrm{noreac}}$ on the F11 attainment rate, and since this is a component independent of δ, it is scaled so that P_0 is 1 for subsequent analysis. Therefore, $\varepsilon_{\mathrm{trans}}(\delta)$ is expressed in the form

$$\varepsilon_{\mathrm{trans}}(\delta) = \left\{\frac{1}{2}\left[1+\mathrm{erf}\left(\frac{\delta-P_1}{\sqrt{2}\,P_2}\right)\right]\cdot\frac{1}{2}\left[1-\mathrm{erf}\left(\frac{\delta-P_3}{\sqrt{2}\,P_4}\right)\right]\right\} \tag{4.14}$$

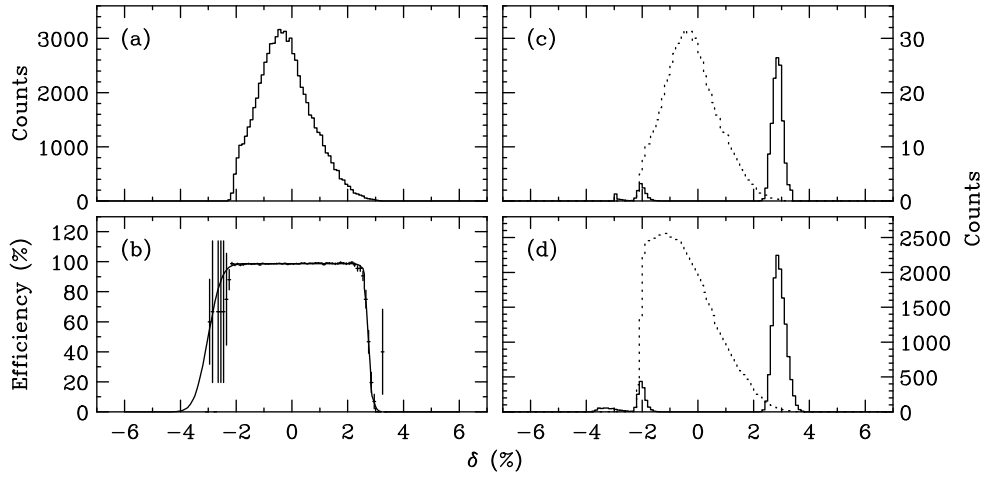

Figure 4.3: (a): Distribution of δ when gating for $x = 0$, $y = 0$, $\theta_x = 0$, $\theta_y = 0$. (b): Measured values of $\varepsilon_{\mathrm{trans}}(\delta)$ are shown as dots with error bars, and fitted with a smoothing window function (4.12). (c): Applying $\varepsilon_{\mathrm{trans}}(\delta)$ to (a) to estimate the number of lost events. The dotted line shows (a) scaled to 1/100. (d): The number of lost events obtained by applying $\varepsilon_{\mathrm{trans}}(\delta)$ to the ungated δ distribution. (a) - (d) all use measurements using a ^{58}Ti beam.

[*1)] One of the correction methods for estimating the error for a binomial distribution with a small sample size n. Let the number of successes k be $k+1$, the number of samples n be $n+2$, and by adding 1 to both the number of successes and the number of failures, we can avoid k/n becoming 1 or 0, and make it possible to estimate the error.

and each parameter is determined by fitting.

Figures 4.3 (c) and (d) show the number of events lost due to the spread of momentum δ, calculated by multiplying (a) by $\varepsilon_{\text{trans}}(\delta)$ defined in equation (4.14).

4.5.3 Position acceptance $\varepsilon_{\text{trans}}(x),\ \varepsilon_{\text{trans}}(y)$

Next, we consider the acceptance of the particle for its position (x, y) on the target. The F8 focal plane is the achromatic focus, and the target is only about 7 mm behind it, so we should mention in advance that the particle distribution is concentrated near $(x, y) = (0, 0)$. The components of the transport efficiency that depend on x, y, the position acceptance $\varepsilon_{\text{trans}}(x),\ \varepsilon_{\text{trans}}(y)$, are defined as

$$\varepsilon_{\text{trans}}(x) = \varepsilon_{\text{trans}}(x, 0, 0, 0, 0) \tag{4.15}$$

$$\varepsilon_{\text{trans}}(y) = \varepsilon_{\text{trans}}(0, y, 0, 0, 0) \tag{4.16}$$

similar to the momentum acceptance $\varepsilon_{\text{trans}}(\delta)$.

4.5.4 Determining the "Good Condition" of $x,\ y,\ \delta$

Among the factors that determine $\varepsilon_{\text{trans}}$, $x,\ y,\ \delta$ are determined only by the particle's motion state upstream, regardless of scattering at the target. Therefore, it is possible to select only events that are in "Good Condition" $x,\ y,\ \delta$ and make $\varepsilon_{\text{trans}}(x) \cdot \varepsilon_{\text{trans}}(y) \cdot \varepsilon_{\text{trans}}(\delta) \sim 100\%$.

To achieve this, in this paper we define "Good Condition" as the case where the following condition is satisfied using the parameters obtained by fitting with the

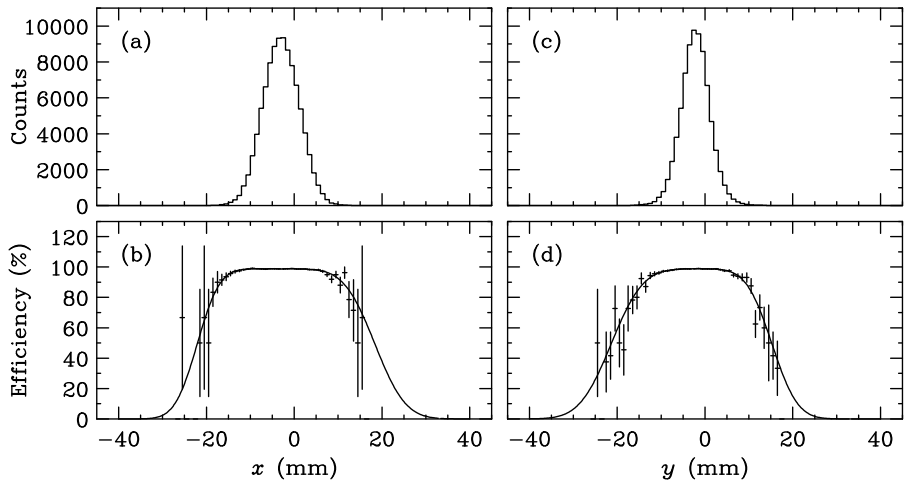

Figure 4.4: (a): Distribution of x when gated so that $y = 0,\ \theta_x = 0,\ \theta_y = 0\ \delta = 0$. (b): Measured values of $\varepsilon_{\text{trans}}(x)$ are shown as points with error bars and fitted with a smoothing window function (4.12). (c): Distribution of y as in (a). (d): $\varepsilon_{\text{trans}}(y)$ was found by fitting as in (b).

equation (4.12):

$$\begin{aligned} &\mu_{Lx} + 2\sigma_{Lx} < x < \mu_{Rx} - 2\sigma_{Rx} \quad \text{AND} \\ &\mu_{Ly} + 2\sigma_{Ly} < y < \mu_{Ry} - 2\sigma_{Ry} \quad \text{AND} \\ &\mu_{L\delta} + 2\sigma_{L\delta} < \delta < \mu_{R\delta} - 2\sigma_{R\delta} \end{aligned} \tag{4.17}$$

Even if the beam is in "Good Condition", the probability that it cannot reach F11 due to $x,\ y,\ \delta$ is at most 0.4 %. Also, when only "Good Condition" beams are used, $\varepsilon_{\text{trans}}$ is almost entirely determined by the remaining $\theta_x,\ \theta_y$, so it can be expressed as $\varepsilon_{\text{trans}}(\theta_x,\ \theta_y)$.

4.5.5 Emission angle acceptance $\varepsilon_{\text{trans}}(\theta_x),\ \varepsilon_{\text{trans}}(\theta_y)$

We also investigated the emission angle acceptance $\varepsilon_{\text{trans}}(\theta_x),\ \varepsilon_{\text{trans}}(\theta_y)$. The results are shown in Figure 4.5.

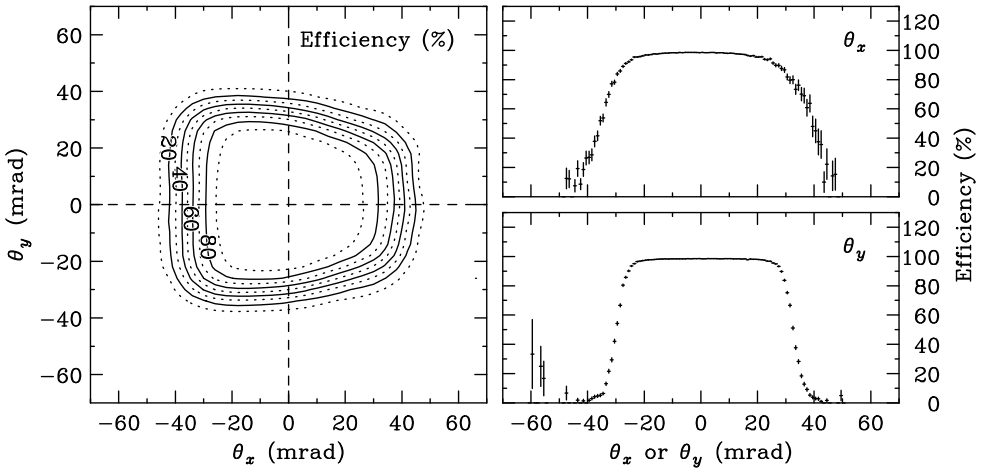

Figure 4.5: Emission angle acceptance $\varepsilon_{\text{trans}}(\theta_x, \theta_y),\ \varepsilon_{\text{trans}}(\theta_x),\ \varepsilon_{\text{trans}}(\theta_y)$. The flat area in the center is 98.4 %

4.6 “Good Condition Beam” and scattering angle acceptance (2)

4.6.1 Scattering angle acceptance $\varepsilon_{\mathrm{trans}}(\theta_{\mathrm{scat}})$ in “Good Condition Beam”

When the incident beam particle is scattered at a large angle by the target, the particle is not transported to the end due to reasons such as hitting the wall of the beam pipe at the downstream ZeroDegree, and particle identification becomes impossible. To know how often this occurs, we obtained the detection efficiency of ZeroDegree with respect to the size of the scattering angle (θ_{scat}), that is, the scattering angle acceptance. There is also a method of using the emission angle (θ_{out}) acceptance for angular acceptance, which depends only on the beamline design, but here we obtained the scattering angle acceptance for convenience in later analysis. In this paper, the acceptance is obtained by using the DSF7 trigger, which indicates the presence of the F7 Plastic signal at the end of BigRIPS, and the F11 trigger, which indicates the F11 Plastic signal at the end of ZeroDegree, and calculating the proportion of events with DSF7 triggers that include the F11 trigger. Three DPPACs at the F8 focal plane are used to measure the scattering angle, and the angular range covered by the F8DPPAC3 behind the target is sufficiently large compared to the angular acceptance of ZeroDegree, so the scattering angle can be derived without any problems even for particle events that do not reach F11. The scattering angle acceptance varies depending on the beam and target conditions, so it was calculated for each setup. As an example, the measurement of a gold target with a ^{56}Ti beam is shown in Figure 4.6.

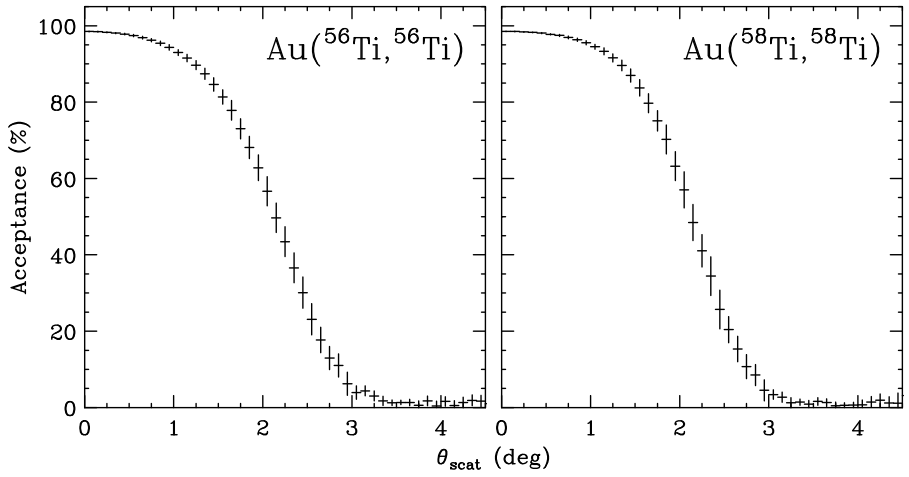

Figure 4.6: Scattering angular acceptance $\varepsilon_{\mathrm{trans}}(\theta_{\mathrm{scat}})$.

4.6.2 "Good Condition Beam" counts

Table 4.4: Counts of G.C. Beam

	^{197}Au(^{56}Ti,^{56}Ti)	^{197}Au(^{58}Ti,^{58}Ti)
$N_{\text{G.C.}\otimes\text{DSF7}}$	6868019	4980718
$N_{\text{G.C.}}$ (Calculated)	13.32863×10^7 (4101 cnt/sec)	9.66448×10^7 (918 cnt/sec)

4.7 Summary of beam counts

Here is a summary of the beam counts we have calculated so far.

Table 4.5: Summary of Beam Counts.

	^{197}Au(^{56}Ti,^{56}Ti)	^{197}Au(^{58}Ti,^{58}Ti)
N_{F7}	2.62097×10^8 (8064 cnt/sec)	8.60546×10^8 (8172 cnt/sec)
N_{PI}	1.7354339×10^8 (5339 cnt/sec)	1.3852885×10^8 (1316 cnt/sec)
$N_{\text{G.C.}}$ ($\equiv N_{\text{beam}}$)	13.32863×10^7 (4101 cnt/sec)	9.66448×10^7 (918 cnt/sec)

In the following analysis, we use only "Good Condition" events and define this number $N_{\text{G.C.}}$ as the beam count N_{beam}.

4.8 Additional analysis of beam profile (1) – Scattering angle

4.8.1 Analysis of position and angle of particle trajectory

In order to later analyze the Doppler shift of gamma rays and obtain the scattering cross section, it is necessary to know the particle trajectory near the target. To achieve this, in this experiment, as shown in Figure 4.7, three double PPACs were installed in front of and behind the target to obtain particle tracks. By analyzing this, the incidence angle θ_{in}, emission angle θ_{out}, and scattering angle θ_{scat} were derived for each event.

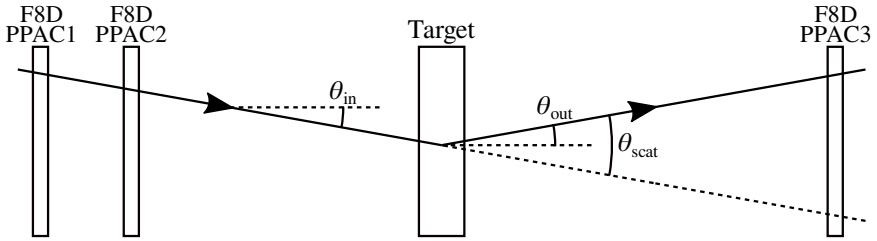

Figure 4.7: Schematic diagram of particle trajectory analysis using PPAC near the target. First, the incident angle θ_{in} is obtained by connecting the (x, y) coordinates obtained from the two upstream units, F8DPPAC1 and F8DPPAC2. By extrapolating this, the particle position on the target can be determined. Then, by connecting this with the (x, y) coordinates of F8DPPAC3 on the downstream side, the particle emission angle θ_{out} and scattering angle θ_{scat} can be obtained.

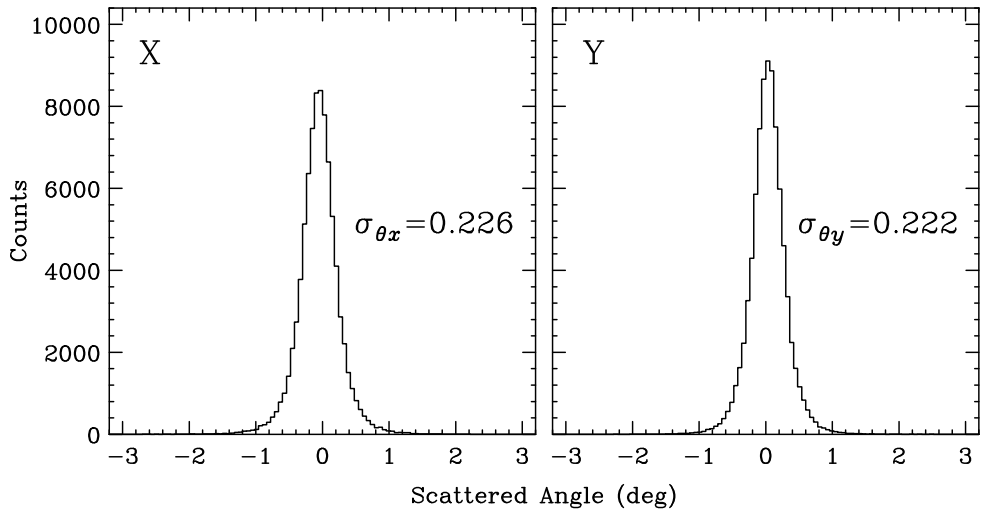

Figure 4.8: Distribution of scattering angles in the x, y directions obtained in measurements without a target.

4.8.2 Evaluation of angular resolution

The angular resolution was evaluated using the measurement results when a beam was emitted without a target. The scattering angle θ_{scat} obtained from the analysis of the three PPACs should essentially be 0 if there was no scattering by a target, and if it has a finite value, it comes from the measurement resolution. Based on this, the spread of the scattering angle distribution without a target was evaluated as the angular resolution. The spread of the scattering angle distribution in each of the x, y directions is shown in Figure4.8.

4.8.3 (Additional information) Conversion of scattering angle to CM system

When calculating the differential scattering cross section, it is convenient for subsequent analysis if the scattering angle θ_{scat} is the angle in the center of mass system, which does not depend on the experimental environment. An example of the correlation between the scattering angle in the laboratory system and the angle in the center of mass system is shown in Figure 4.9.

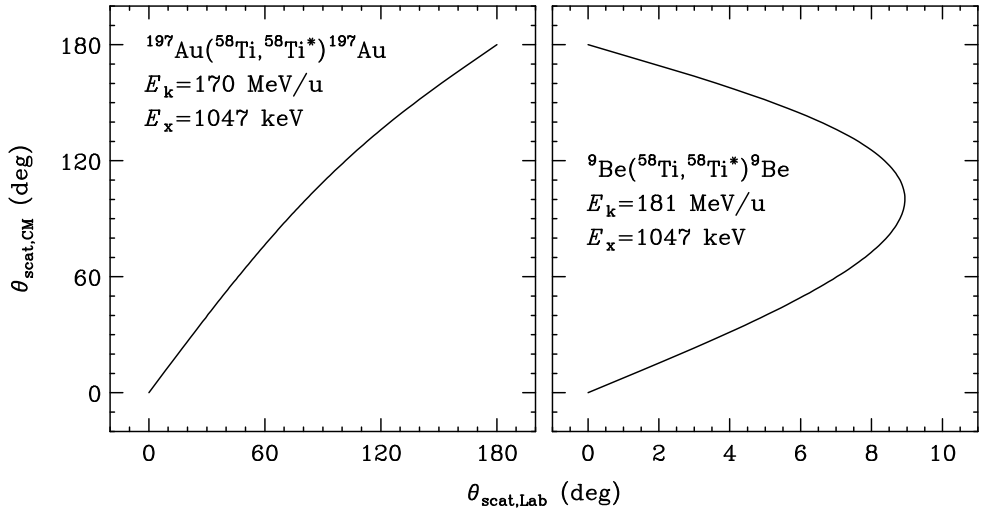

Figure 4.9: The relationship between the scattering angle $\theta_{\mathrm{scat,Lab}}$ in the laboratory system and the scattering angle $\theta_{\mathrm{scat,CM}}$ in the center of mass system. The left figure shows the case where a ^{58}Ti beam is hit on a gold target, and the right figure shows the case where it is hit on a Be target. Differences due to the mass of the target can be seen.

4.9 Additional analysis of beam profile (2) – Velocity β

The beam particle velocity β is obtained from TOF measurements. The particle velocity distributions β_{57} and β_{89} for F5-F7 (upstream of the target) and F8-F9 (downstream of the target) are shown in the upper part of Figure 4.10. These will be used in the analysis of the Doppler shift correction of gamma rays later.

4.9.1 Evaluation of error of β

The measurement error (resolution) of β was calculated from the difference between β_{57} obtained from the TOF between F5-F7 and β_{89} between F8-F9. In measurements without a target, β_{57} and β_{89} should be the same value, except for the effect of slight energy loss due to passing through detector materials such as plastic scintillators. These differences arise from measurement errors in β and

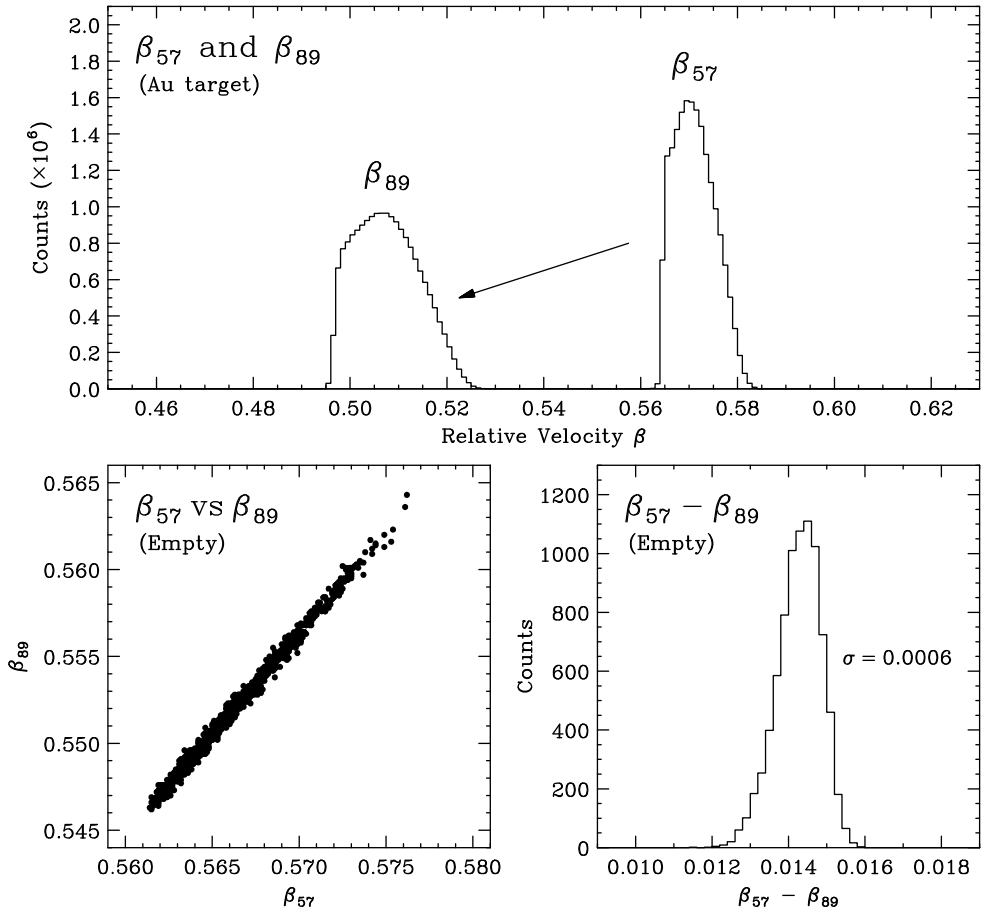

Figure 4.10: Top: β_{57} and β_{89} for a ^{58}Ti beam and a gold target. Passing through the target and beamline detector slows down the beam and broadens the distribution. Left: Correlation between β_{57} and β_{89} in a measurement without a target. Right: Distribution of $\beta_{57} - \beta_{89}$ in the same measurement without a target.

energy fluctuations due to passage through the detector material. In other words, the resolution of β is smaller than the spread of the distribution of the differences. As shown in the bottom right of Figure 4.10, the width σ of the distribution of the difference between β_{57} and β_{89} was 0.0006, which means that the resolution of β is smaller than this.

4.9.2 Change in β near the target

What is important in the analysis is the velocity β_{before} and β_{after} just before and just after the target, and the velocity β_{center} at the center of the target, which is used in the later analysis of Doppler correction. These are obtained by calculating the energy loss at the beamline detector and target from β_{57} and β_{89} obtained from measurements. Figure 4.11 shows the definition positions for β_{57} and β_{89}, as well as the detectors and targets located nearby. β_{before}, β_{after} and β_{center} were calculated using the average values of β_{57} and β_{89}, $\overline{\beta_{57}}$ and $\overline{\beta_{89}}$, using the energy loss calculation tool included in LISE^{++} [58]. These are summarized in Table 4.6.

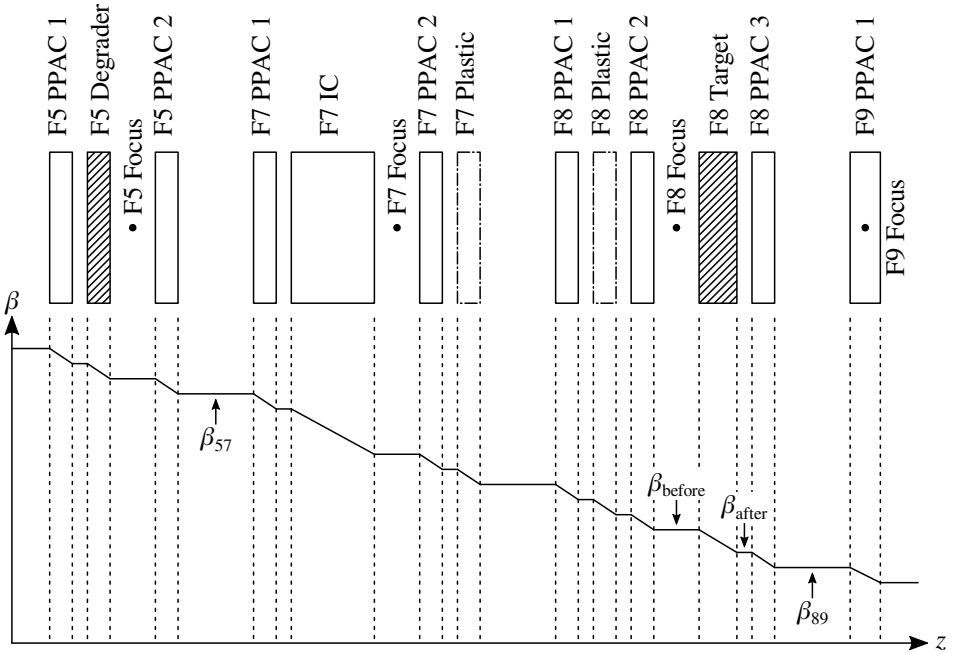

Figure 4.11: Since many detectors are inserted between the target and the β_{57} and β_{89} obtained in the measurements, the velocity just before and just after the target (β_{before}, β_{after}) must be found by calculating the energy loss from β_{57} and β_{89}.

Table 4.6: Measured values of $\overline{\beta_{57}}$ and $\overline{\beta_{89}}$, and calculated values of $\overline{\beta_{\text{before}}}$, $\overline{\beta_{\text{center}}}$, and $\overline{\beta_{\text{after}}}$.

Setup	$\overline{\beta_{57}}$	$\overline{\beta_{\text{before}}}$	$\overline{\beta_{\text{center}}}$	$\overline{\beta_{\text{after}}}$	$\overline{\beta_{89}}$
Au(^{56}Ti,^{56} Ti)	0.5695	0.5546	0.5294	0.5024	0.5023
Au(^{58}Ti,^{58} Ti)	0.5701	0.5560	0.5337	0.5064	0.5060

4.10 Additional analysis of beam profile (3) – Target thickness

Although the target thickness is not a "Beam Profile", in this section we calculate the target thickness from the change in β obtained in the previous section.

The target thickness can be obtained from the change in β up to this point. The gold target used in this study has a nominal thickness of 1 mm, but by measuring the velocity change of the beam particles, we were able to obtain a more accurate (finer digits) thickness. In addition, tools such as calipers and micrometers can be used to measure the thickness, but since gold is a soft metal and there is a risk of it being deformed during measurement, we decided that this method was the best. As shown in Figure 4.11, there are many detectors between β_{57} and β_{89} in addition to the target, so it is necessary to verify the accuracy of the estimate of the energy loss due to them. To do this, we first compared the β_{89} obtained by targetless measurement with the β_{89} obtained by calculation, and confirmed the material thickness of the detector. Since the detector with the greatest energy loss is the ion chamber (Music), the density of the ion chamber was fine-tuned to make the calculated and measured β_{89} match. Then, for measurements with a target, the difference between the calculated and measured β_{89} was calculated while changing the target thickness, to obtain the gold target thickness:

$$d_{\mathrm{tar}}(1\mathrm{mm\ Au}) = 959(11) \quad (\mu\mathrm{m}) \tag{4.18}$$

Here, the error in the target thickness is affected by the uncertainty resulting from the error in the beam particle velocity β, so an error was added to take this into account.

4.11 Additional analysis of beam profile (4) – PI at ZeroDegree

To reduce the background of the gamma-ray spectrum to be analyzed later, a particle discrimination cut is also performed in the ZeroDegree spectrometer downstream of the target. The significance of this is that although previous analyses have shown that the nuclear reactions in the target are negligible compared to the total beam dose, they become a non-negligible background source in terms of their proportion in gamma-ray emission events.

4.11.1 Why should we not include PI at ZeroDegree in "Good Condition" ?

If the scattering angle distribution of Coulomb excitation events is significantly larger than that of non-reaction events, when a cutoff condition is imposed using a detector downstream of the target, Coulomb excitation events may be selectively counted down due to the scattering angle dependence of the detection efficiency, i.e., the scattering angle acceptance $\varepsilon(\theta_{\mathrm{scat}})$. This effect influences the final derived cross-sectional area. Therefore, the cutoff conditions for background reduction should only be used for the detector upstream of the target.

4.11.2 Cutting conditions at ZeroDegree

The cutoff condition for particle identification at ZeroDegree was decided to prioritize capturing as many events as possible with certainty, and to acquire only A/Q within the range of $\pm 3\sigma$. Since particle identification is performed upstream, any particles other than the target nuclei that arrive downstream are produced by nuclear reactions in the target, and the possibility of contamination with nuclides with similar A/Q values and the same Z is extremely low. Therefore, only A/Q was cut. However, this cut may result in genuine events being overlooked (mostly due to PPAC efficiency), and we will make a correction for this in the next section.

4.11.3 Particle identification efficiency after passing the target $\varepsilon_{\mathrm{PI}}$

The particle identification efficiency $\varepsilon_{\mathrm{PI}}$ is the probability that a particle is correctly identified by the ZeroDegree spectrometer under the condition that there is a plastic signal at the F11 focal plane (= a particle has arrived). In other words, it is the ratio of the number of events in which A/Q and Z are within a certain range in the PI diagram at ZeroDegree to the number of counts of the F11 plastic signal. The

analysis results of $\varepsilon_{\mathrm{PI}}$ for ^{56}Ti / ^{58}Ti are as follows:

$$\varepsilon_{\mathrm{PI}}(^{56}\mathrm{Ti}) = 0.9030(79) \tag{4.19}$$

$$\varepsilon_{\mathrm{PI}}(^{58}\mathrm{Ti}) = 0.9055(55) \tag{4.20}$$

Chapter 5

Data Analysis (III) – Gamma-ray Detector

5.1 Analysis of the gamma-ray detector

In this chapter, we begin the analysis of the gamma-ray detector. First, in section 5.2, we integrate the data from the beamline detector and remove the background from the time difference with the F8 plastic scintillator. Next, in section 5.3, we perform Doppler shift correction from the particle velocity and trajectory obtained from the beamline detector and the gamma-ray detection position, and create a gamma-ray spectrum. Then, in section 5.4, we calculate the gamma-ray yield and cross section by comparing with simulations.

5.2 Time cut of gamma ray signal

As mentioned in Section 4.7, the data acquisition condition in this experiment is when the signal from the Ge detector and the signals from the F7 and F11 plastic detectors are measured simultaneously. However, data acquisition can occur by coincidentally receiving environmental radiation in synchronization with the beam particles. If there are many such events, they become a background source that buries and makes invisible the real gamma rays from the beam particles, so it is necessary to reduce them.

The left side of the figure 5.1 is a spectrum of gamma rays obtained with the Ge detector without any correction or condition cut other than energy calibration. The multiple peaks seen here are background from environmental radiation sources. If they are real gamma rays from beam particles, the time difference of the Ge detector based on the signal from the F8 plastic detector will always be constant, so by selecting only the area around the peak of the time distribution shown in the figure on the right, gamma rays from environmental radiation sources can be reduced. In

this study, the time difference distribution was examined for each crystal in the Ge detector, and the gamma-ray background was reduced by analyzing only events that fell within the range of the peak $\pm 3\sigma$. This process cuts off some of the real gamma-ray events. In addition, since the peak does not truly become a Gaussian function, the probability that a real gamma-ray event falls inside the set time window, the time cut efficiency $\varepsilon_{\text{time}}$, was estimated.

As a method, the linear component when fitting with a Gaussian function + straight line was assumed to be the background, and the component above it was assumed to be the real peak component. The integral value in a sufficiently wide range was set to 100 %, and the percentage of the integral value within the time window was determined for each crystal. The time cut efficiency $\varepsilon_{\text{time}}$ of the whole crystal used in the analysis obtained in this way is

$$\varepsilon_{\text{time}} = 0.9651(72) \tag{5.1}$$

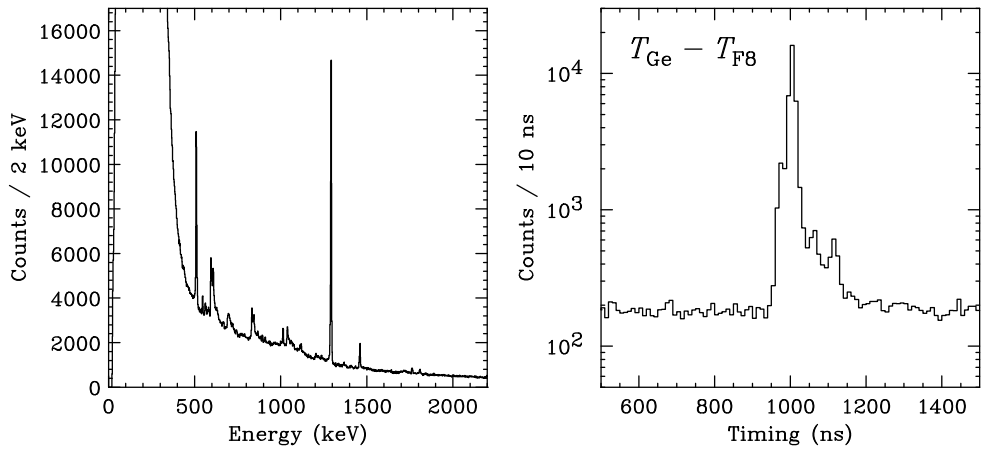

Figure 5.1: Left: Gamma-ray spectrum before time cutting. The multiple peaks seen here are emitted from stationary radiation sources in the laboratory system, so they are all background sources. These sources are thought to be experimental equipment that has been activated by beam irradiation, radon contained in the air, etc. Incidentally, real gamma rays originating from beam particles change energy due to Doppler shift, so they do not produce peaks unless Doppler correction, which will be described later, is performed. Right: Trigger timing of the Ge detector based on the signal from the F8 plastic detector. The peak around 1000 ns is gamma rays originating from beam particles, and the other constant components are environmental background.

5.3 Doppler correction of gamma rays

5.3.1 Policy

As shown in section 2.7.1, the relationship between the energy E_0 of gamma rays emitted from a nucleus in flight and the energy E_{lab} actually detected by a detector installed in a laboratory is

$$\frac{E_{\mathrm{lab}}}{E_0} = \frac{\sqrt{1-\beta^2}}{1-\beta\cos\theta_\gamma} \tag{2.16}$$

As can be seen from this equation, in order to know E_0 accurately, it is necessary to know not only E_{lab}, but also β and θ_γ accurately.

First, for β, we use the velocity β_{57} between F5-F7 and the velocity β_{89} between F8-F9, both of which were calculated from the analysis of TOF and $B\rho$. θ_γ is the angle of the gamma ray emission relative to the direction of the particle's travel. This can be derived by knowing the position where the gamma ray was detected by the Ge detector and the direction of the particle's travel. We will first explain the derivation of β.

5.3.2 Velocity β

As mentioned in section 4.9, the velocity at the center of the target, β_{center}, can be derived from β_{57} and β_{89}. When performing rigorous Doppler correction, it is even better to know the velocity at the time when the gamma rays are truly emitted, β_{Emit}. As shown in Figure 5.2, there is a change in velocity within the target. The difference between the velocity immediately after entering the target ($\sim \beta_{\mathrm{before}}$) and the velocity immediately before leaving the target ($\sim \beta_{\mathrm{after}}$) is approximately 0.9 %. The resulting energy difference after the Doppler shift is larger than the intrinsic energy resolution of the Ge detector. However, since there is no way to know β_{Emit},

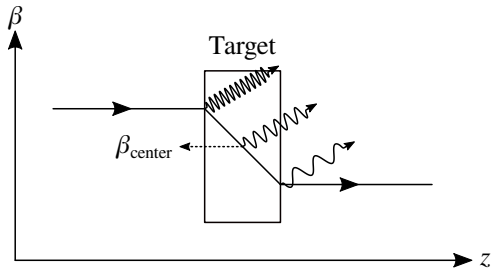

Figure 5.2: When gamma rays are emitted from a nucleus in flight, they slow down due to energy loss in the target, and since β changes depending on the position within the target, the amount of Doppler shift also depends on the position within the target.

we assume that the nuclear reaction (Coulomb excitation reaction) occurs at the target center in all events, and calculate the velocity at the target center β_{center} for each event. In section 4.9, we calculated the average value of β_{center}, but in the analysis in this study, we derive β_{center} for each event. However, since it is difficult to calculate the energy loss for all events, we use the fact that the ratio of β_{89} to β_{center} is almost constant in the range where the fluctuation of β_{89} is not too large. *1) β_{center} for each event can be expressed as follows:

$$\beta_{\text{center}} = \overline{\beta_{\text{center}}} \times \left(1 + \frac{\beta_{89} - \overline{\beta_{89}}}{\overline{\beta_{89}}}\right) \tag{5.2}$$

By using this, we only need to calculate the energy loss of $\overline{\beta_{\text{center}}}$ once at the beginning.

5.3.3 Gamma ray emission angle θ_γ

According to the equation 2.16, the Doppler shift of gamma rays depends on the angle θ_γ of the gamma rays. To obtain θ_γ, the angle between the particle emission direction $\boldsymbol{P}_{\text{par.,out}}$ and the gamma ray emission direction $\boldsymbol{P}_{\gamma,\text{out}}$, that is:

$$\cos\theta_\gamma = \frac{\boldsymbol{P}_{\text{par.,out}} \cdot \boldsymbol{P}_{\gamma,\text{out}}}{P_{\text{par.,out}} P_{\gamma,\text{out}}} \tag{5.3}$$

Of these, $\boldsymbol{P}_{\text{par.,out}}$ is calculated by trajectory analysis using PPAC in the same way as in Section 4.4.2 to derive the particle scattering angle. $\boldsymbol{P}_{\gamma,\text{out}}$ is the vector

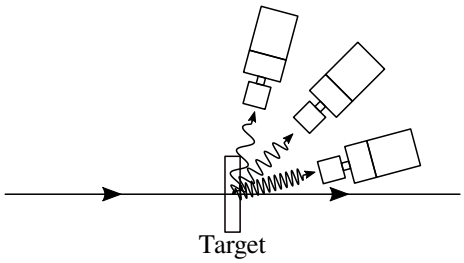

Figure 5.3: According to the equation 2.16, the Doppler shift of a gamma ray depends on the angle of the gamma ray.

*1) The reason for using β_{89} instead of β_{57} is that it is affected by the velocity change associated with momentum transfer due to nuclear reactions. For example, β changes significantly before and after the reaction, especially in reactions where nucleons enter and leave, such as one-proton knockout reactions. Since gamma ray emission always occurs after the reaction, it is appropriate to calculate it from the downstream rate.

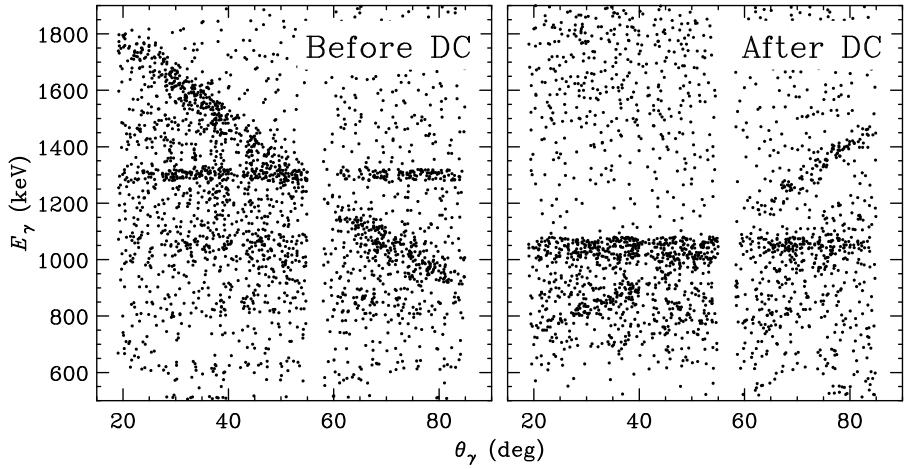

Figure 5.4: Gamma-ray energies of ^{58}Ti as a function of the emission angle θ_γ, shown before (left) and after (right) Doppler-shift correction. The 1047 keV transition from ^{58}Ti, which appears tilted prior to the correction, becomes horizontal after the correction is applied. The background structure observed near 1300 keV before the correction is attributed to the 1294 keV transition from ^{116}In, originating from the ^{115}In(n, γ) reaction.

connecting the target center and the position where the gamma ray was detected by the Ge detector. The detection position of the gamma ray is determined by different methods for tracking detectors and non-tracking detectors. First, we will explain the parts that are common to both tracking and non-tracking detectors. To know the exact detection position, it is necessary to know the exact spatial arrangement of the Ge crystals, which are the sensitive area of the Ge detector. To achieve this, in this experiment, the detector arrangement was measured by photogrammetry. The positions of the Ge crystals in the detector were compared with the drawings of the detector, and by combining these, the arrangement of the Ge crystals in the laboratory coordinate system was obtained. In the case of a tracking detector, the position of the interaction point in the crystal and the energy imparted there can be determined. Generally, gamma rays often undergo several Compton scatterings before being photoelectrically absorbed, and there are often multiple interaction points within a crystal, but the first interaction point is necessary to determine the gamma ray emission direction. Empirically, it is known that the point where the highest energy is deposited is often the first point, so this was adopted in this study. On the other hand, with non-tracking detectors, the position of the interaction point cannot be directly determined, but the Minball and Clover detectors used in this experiment have divided outer electrodes, so it is possible to restrict the interaction position within the crystal depending on which electrode the signal is obtained from. In this analysis, the center of the area covered by the electrode that output the signal

is considered to be the interaction point.

5.3.4 Doppler corrected spectrum

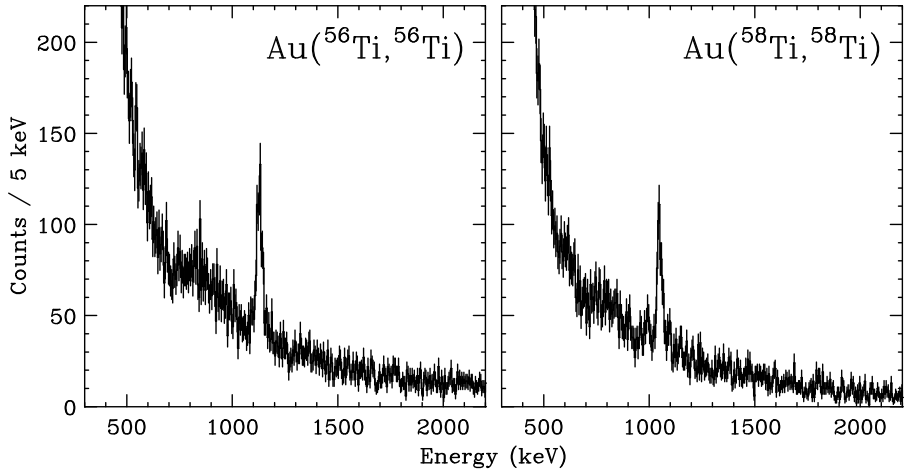

Figure 5.5: Spectra obtained by time cutting and Doppler correction. The left is the measurement result for Au(^{56}Ti,^{56} Ti), The right is the measurement result for Au(^{58}Ti,^{58} Ti).

Figure 5.5 shows the gamma-ray spectrum obtained by applying the time cut described in Section 5.2 and Doppler correction. Sharp peaks can be seen near 1000 keV for both ^{56}Ti and ^{58}Ti. We will consider these to be gamma rays due to $2^+ \rightarrow 0^+$ transitions in the subsequent analysis. The known levels of ^{56}Ti and ^{58}Ti and the level scheme for gamma rays are shown in Figure 5.7.

5.3.5 Scattering angle acceptance correction

Each event is weighted by the inverse of the scattering angle acceptance obtained in section 4.6.1, and the spectrum in Figure 5.5 is redrawn as shown in Figure 5.6. Subsequent yield evaluations will be based on this spectrum.

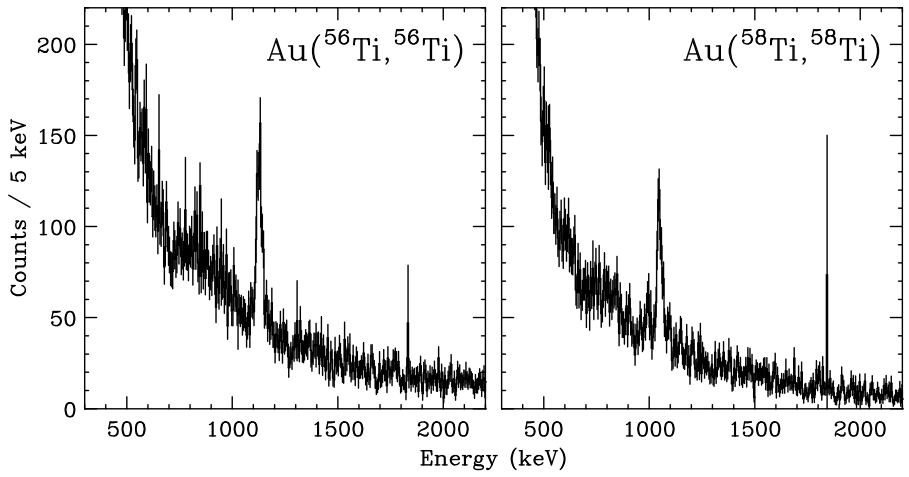

Figure 5.6: Spectra with scattering angle acceptance correction. Both have a thin peak around 1700 keV, but this is produced by a single event scattered at a large angle and multiplied by a very large scattering angle acceptance correction coefficient, and is not a peak with any physical meaning.

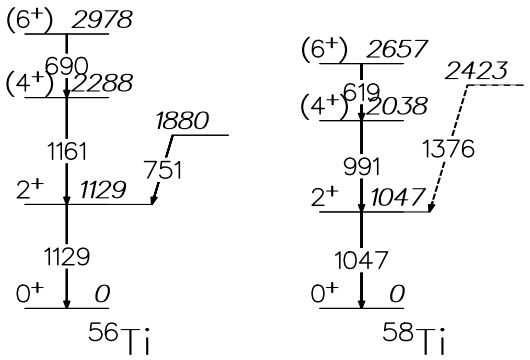

Figure 5.7: ^{56}Ti/^{58}Ti level scheme.

5.4 Evaluation of yield (1)

5.4.1 Method

When counting the yield of gamma rays emitted from stationary nuclei, it is only necessary to correct the number of peaks in the spectrum with the detection efficiency, but in in-beam nuclear spectroscopy experiments, there are more things to consider. Specifically,

- Correction of detection efficiency taking into account the energy before Doppler correction
- Dependence of reaction position (flight velocity) within the target
- Effect of gamma ray decay lifetime

and so on. Of course, it is possible to calculate these by hand, but it is complicated and requires a lot of effort. Therefore, this time, we evaluated the yield by simulation. In the simulation, we reproduced the environment during the experiment, such as the structure of the HiCARI array and the energy distribution of the beam, and reproduced the gamma ray spectrum. The unknown gamma ray energies and lifetimes (within known error ranges) were randomly assigned to best reproduce the experimental results. Finally, the yield was determined from the scale between the gamma ray dose generated in the simulation and the experimental value. It is also possible that the number of $2_1^+ \rightarrow 0_{\mathrm{g.s.}}^+$ transition gamma rays emitted and the number of $0_{\mathrm{g.s.}}^+ \rightarrow 2_1^+$ transitions caused by Coulomb excitation may differ. This is when the gamma ray is excited to an energy level higher than the 2_1^+ level, and then a cascade decay occurs to emit $2_1^+ \rightarrow 0_{\mathrm{g.s.}}^+$ gamma rays. This type of event is called a feeding event. The existence of feeding affects the calculation of the cross section, so it is necessary to estimate it correctly.

5.5 Evaluation of yield (2) – Simulation

5.5.1 Reproduction of beam and target

In section 2.11, the HICARI array was reproduced in a simulation and the detector performance was adjusted. Here, the beam is irradiated to the target in a simulation to generate gamma rays. The velocity distribution of the beam particles generated in the simulation $\{\beta_{\mathrm{before,sim}}\}$*1) is calculated by using the velocity distribution $\{\beta_{57}\}$ of the beam between F5 and F7 to reproduce the actual beam velocity obtained in section 4.9.2,

$$\{\beta_{\mathrm{before,sim}}\} = \{\beta_{57}\} - (\overline{\beta_{57}} - \overline{\beta_{\mathrm{before}}}) \tag{5.4}$$

is given. In addition, the velocity distribution of the particle after passing through the target obtained by simulation, $\{\beta_{\mathrm{after,sim}}\}$, is obtained by adjusting the energy loss at the target so that $\{\beta_{89,\mathrm{sim}}\} = \{\beta_{\mathrm{after,sim}}\} - (\overline{\beta_{\mathrm{after}}} - \overline{\beta_{89}})$, which is approximately the same as $\{\beta_{89}\}$ obtained from the measurement. These are shown in Figure 5.8.

5.5.2 Uncertainty of energy and lifetime

The energy of the 2^+ level of ^{58}Ti is currently listed in the NNDC [21] as 1047(4) keV, with an error of ±4 keV. If the energy fluctuates within this error range, the

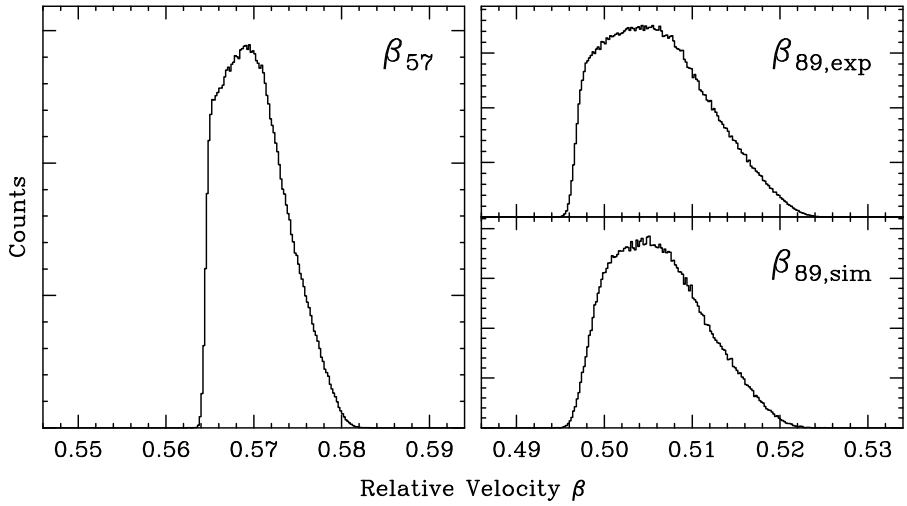

Figure 5.8: A comparison of the $\beta_{89,\mathrm{sim}}$ distribution (bottom right) reproduced by a simulation created by inputting the distribution of measured values of β_{57} (left) and the β_{89} obtained by measurement (top right, denoted as $\beta_{89,\mathrm{exp}}$ in the figure).

*1)The subscript "before" means "before" target injection. It conforms to the notation in section 4.9.2.

peak position of the gamma-ray spectrum will fluctuate. In addition, although there are no observed values at present, when the 2^+ level has a finite lifetime ($\sim$ few ps), gamma-ray emission will occur at a position slightly behind the location where the Coulomb excitation reaction occurred. If the probability of the Coulomb excitation reaction occurring within the target does not depend on the position, the most expected position for gamma-ray emission will transition slightly behind the center of the target. In other words, as shown in Figure 5.2, the average particle velocity β when gamma-ray emission occurs is slower than the velocity β_{center} at the target center, and the gamma-ray energy after the Doppler shift is lower. For this reason, the peak shape of the gamma-ray spectrum can change due to fluctuations in energy and lifetime. Here, since it is necessary to compare the gamma-ray spectrum actually obtained with the simulation to obtain the gamma-ray yield, the energy and lifetime in the simulation were adjusted to best reproduce the spectrum obtained by measurement. Incidentally, there is a method called the Doppler shift method [31] that determines the lifetime from the difference in the Doppler-corrected peak shape, but since it is expected that the error will be very large compared to the method of calculation from the cross section described later, we decided not to include it in this paper.

5.5.3 Angular distribution of gamma-ray emission

Just as the emission angles of the two gamma rays of 1173 keV and 1332 keV emitted from the ^{60}Co gamma-ray source are correlated, the direction of the gamma rays emitted when the beam particles are de-excited has an angular distribution with respect to the beam axis direction. The angular distribution for this experiment was obtained in the appendix D. The result is shown in figure 5.9.

5.5.4 Creating a gamma-ray spectrum

After making these settings, we simulated gamma-ray detection. We created many gamma-ray emission energies and lifetimes that were gradually changed near the values in NNDC [21]. Figure 5.10 shows the final result that best reproduced the experimental values. In addition, from the level scheme of ^{56}Ti and ^{58}Ti shown in Figure 5.7, we also created a simulation for a transition (1161 / 911 keV) that may emit energy close to the gamma ray of $2^+_1 \rightarrow 0^+_{\mathrm{g.s.}}$.

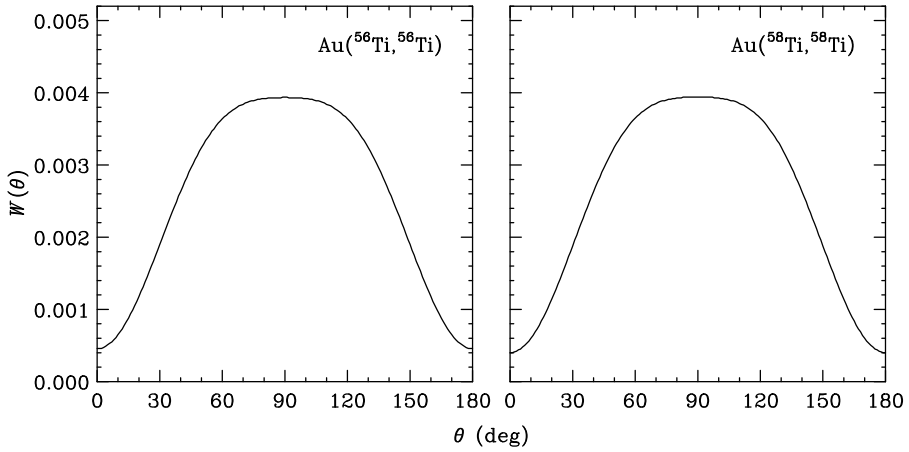

Figure 5.9: Angular distribution $W(\theta)$ calculated under the experimental setup conditions. θ is the angle with respect to the beam axis. The emission amount changes significantly between 0° and 90° for both Au(^{56}Ti,^{56} Ti) and Au(^{58}Ti,^{58} Ti).

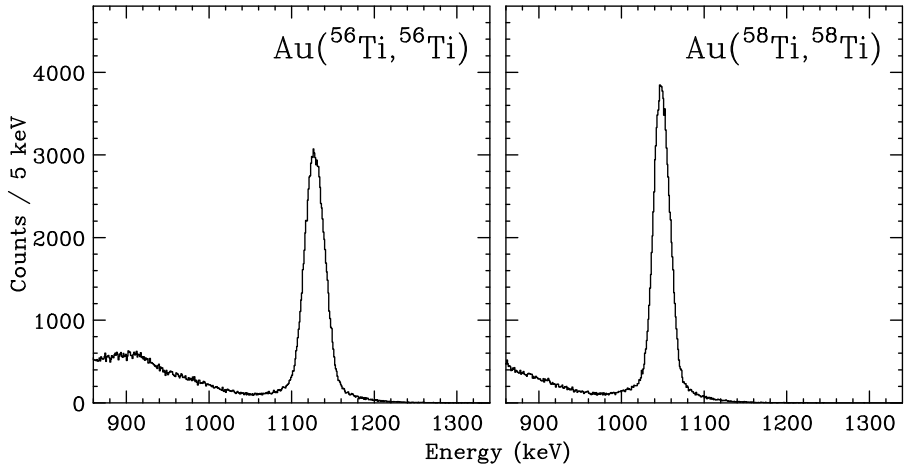

Figure 5.10: A simulated gamma-ray spectrum created to reproduce experimental data.

5.6 Evaluation of yield (3) – Comparison of experimental data and simulation

5.6.1 Fitting function

The gamma-ray spectrum created by simulation is used as a function to fit the gamma-ray spectrum obtained from the experiment. The fitting function is:

$$f_{\mathrm{fit}}(x) = p_0 \cdot f_{\mathrm{main}}(x, \tau_{\mathrm{main}}, E_{\mathrm{main}}) + p_1 \cdot f_{\mathrm{sub}}(x, E_{\mathrm{sub}}) + \exp(p_2 + p_3 x) \qquad (5.5)$$

Here, $f_{\mathrm{main}}(x, \tau_{\mathrm{main}}, E_{\mathrm{main}})$ and $f_{\mathrm{sub}}(x, E_{\mathrm{sub}})$ are functions that represent the gamma-ray spectrum of the simulation created in section 5.5, where the subscript main represents the peak due to the $2^+ \rightarrow 0^+$ transition, which is the focus of this study, and sub represents the peak due to the $(4^+) \rightarrow 2^+$ transition, which may appear near main. We have created a large number of models where the lifetime τ and gamma ray energy E are slightly changed near the values in NNDC [21].

5.6.2 Fitting results and obtained parameters

The experimental data was fitted by simulation.

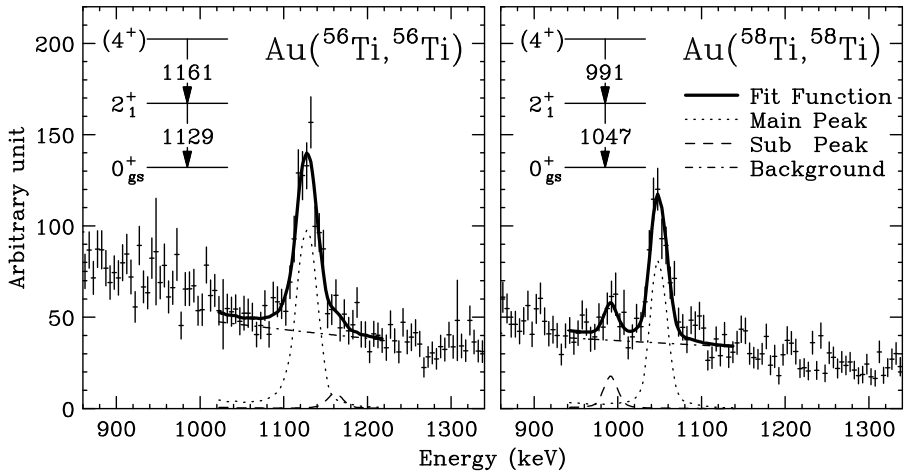

Figure 5.11: The fitting result with the smallest chi-square for the ^{56}Ti/^{58}Ti gamma-ray spectrum.

5.6.3 Determining the central value and error of parameters

The fitting parameters that best reproduce the gamma-ray spectrum vary depending on E, τ. Figure 5.12 shows the change in parameter p_0 when the lifetime τ is changed. In this figure, E is selected for the parameter that produces the smallest χ^2

at each τ. Next, Figure 5.13 shows the lifetimes obtained from theoretical predictions and past experimental values, as well as the range within +1 of the minimum χ^2 obtained by fitting. From this, the maximum possible range of lifetimes was set, and the central value and error of p_0 were determined by convolving p_0 included in that range with its error.

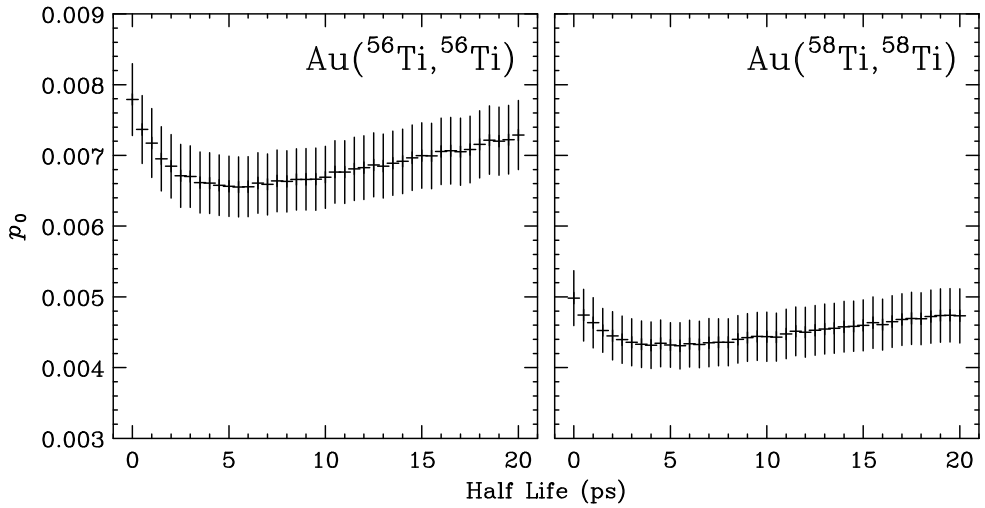

Figure 5.12: Change in fitting parameter p_0 obtained when changing the half-life $T_{1/2}$ of gamma-ray emission in the simulation.

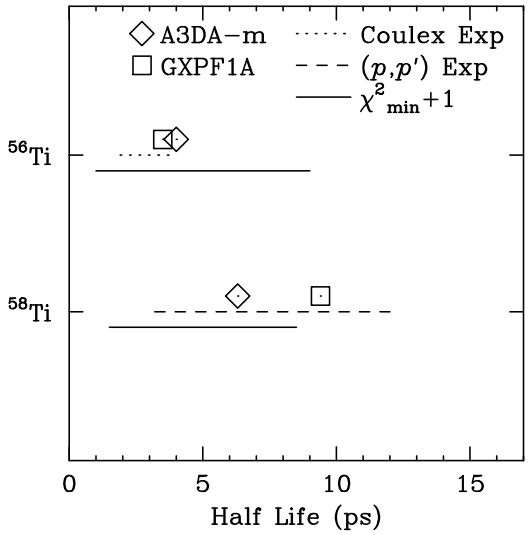

Figure 5.13: For A3DA-m and GXPF1A, the B(E2) values were converted to half-lives using the equation (1.16). The values obtained from Coulomb excitation measurements of ^{56}Ti are from NNDC [21]. The values obtained from (p, p') measurements of ^{58}Ti were calculated in section 1.5.2.

The parameter thus obtained is :

$$p_0(^{56}\mathrm{Ti}) = 0.00669(47) \tag{5.6}$$
$$p_1(^{56}\mathrm{Ti}) = 0.0045(35) \tag{5.7}$$
$$p_0(^{58}\mathrm{Ti}) = 0.00440(34) \tag{5.8}$$
$$p_1(^{58}\mathrm{Ti}) = 0.0099(33) \tag{5.9}$$

5.6.4 Tentative yield obtained from fitting results

To estimate the number of gamma rays actually generated, $N_{\gamma,\mathrm{exp}}$, using the number of gamma rays generated in the simulation, $N_{\gamma,\mathrm{sim}}$, and the fitting parameter p_s, which represents the scale, we can use the following:

$$N_{\gamma,\mathrm{exp}} = p_s \times N_{\gamma,\mathrm{sim}} \tag{5.10}$$

Here, $N_{\gamma,\mathrm{sim}}$ is 10^7 for the main peak (p_0) and 10^6 for the sub-peak (p_1). The yield obtained from this is a "tentative" value that has not been subjected to the various corrections that will be made later, so the subscript "tmp" is added. Taking these factors into account, the gamma-ray yield estimated from the fitting parameters is :

$$N_{\gamma,\mathrm{exp,tmp}}(^{56}\mathrm{Ti}, \mathrm{Main}) = 6.69(47) \times 10^4 \tag{5.11}$$
$$N_{\gamma,\mathrm{exp,tmp}}(^{56}\mathrm{Ti}, \mathrm{Sub}\ ) = 0.45(35) \times 10^4 \tag{5.12}$$
$$N_{\gamma,\mathrm{exp,tmp}}(^{58}\mathrm{Ti}, \mathrm{Main}) = 4.40(34) \times 10^4 \tag{5.13}$$
$$N_{\gamma,\mathrm{exp,tmp}}(^{58}\mathrm{Ti}, \mathrm{Sub}\ ) = 0.99(33) \times 10^4 \tag{5.14}$$

5.7 Evaluation of yield (4) – Yield correction

From this point on, it is self-evident that this is the gamma-ray yield of experimental data, so the subscript exp will be omitted, and $N_{\gamma,\mathrm{exp,tmp}}$ will be written as $N_{\gamma,\mathrm{tmp}}$.

5.7.1 Efficiency correction of Ge detector

In section 2.11.2, efficiency correction was performed for each Ge crystal, but the error in the detection efficiency was reduced by further applying a correction coefficient to the total value of the individual corrections and the actual overall detection efficiency. The yield obtained from the fitting results was corrected using the correction coefficients.

The relative value $\varepsilon_{\mathrm{sim}}$ of the actual detection efficiency to the detection efficiency in the simulation of the tracking detector, obtained in Section 2.11.3, was

$$\varepsilon_{\mathrm{sim}} = 0.95(9) \tag{2.31}$$

5.7.2 Time window cut correction

The data acquisition efficiency $\varepsilon_{\mathrm{time}}$ after the time window cut, obtained in section 5.2, was

$$\varepsilon_{\mathrm{time}} = 0.9651(72) \tag{5.1}$$

5.7.3 Particle identification efficiency correction

As obtained in section 4.11.3, the particle identification efficiency correction $\varepsilon_{\mathrm{PI}}$ at ZeroDegree is

$$\varepsilon_{\mathrm{PI}}(^{56}\mathrm{Ti}) = 0.9030(79) \tag{4.19}$$
$$\varepsilon_{\mathrm{PI}}(^{58}\mathrm{Ti}) = 0.9055(55) \tag{4.20}$$

5.7.4 Corrected gamma-ray yield

To obtain the corrected gamma-ray yield N_γ using the $\varepsilon_{\mathrm{sim}}$ and $\varepsilon_{\mathrm{time}}$ obtained so far,

$$N_\gamma = \frac{1}{\varepsilon_{\mathrm{sim}}} \frac{1}{\varepsilon_{\mathrm{time}}} \frac{1}{\varepsilon_{\mathrm{PI}}} N_{\gamma,\mathrm{tmp}} \tag{5.15}$$

The gamma-ray yield N_γ obtained in this way is

$$N_\gamma(^{56}\mathrm{Ti}, \mathrm{Main}) = 8.08(96) \times 10^4 \quad (5.16)$$

$$N_\gamma(^{56}\mathrm{Ti}, \mathrm{Sub}\ ) = 0.54(43) \times 10^4 \quad (5.17)$$

$$N_\gamma(^{58}\mathrm{Ti}, \mathrm{Main}) = 5.30(65) \times 10^4 \quad (5.18)$$

$$N_\gamma(^{58}\mathrm{Ti}, \mathrm{Sub}\ ) = 1.19(41) \times 10^4 \quad (5.19)$$

5.8 Cross section derivation (1) – Gamma ray emission cross section

5.8.1 General cross section calculation

Generally, any reaction cross section σ_{reac} can be written as follows, using the number of particles N_{beam} incident as a beam and the number of particles that react N_{reac}:

$$\sigma_{\mathrm{reac}} = \frac{N_{\mathrm{reac}}}{N_{\mathrm{beam}}} \cdot \frac{M_{\mathrm{tar}}}{\rho_{\mathrm{tar}} d_{\mathrm{tar}} N_{\mathrm{A}}} \tag{5.20}$$

In the equation, M_{tar}, ρ_{tar}, and d_{tar} are the molar mass, density, and thickness of the target material, respectively. Therefore, the second fractional part on the right-hand side is determined only by the target used, so it is set as a constant

$$C_{\mathrm{tar}} \equiv \frac{M_{\mathrm{tar}}}{\rho_{\mathrm{tar}} d_{\mathrm{tar}} N_{\mathrm{A}}} \tag{5.21}$$

This value has the dimension of area, and its physical meaning is that there is one target particle per area C_{tar}. The thickness of the ^{197}Au target used in the experiment was calculated in section 4.10,

$$d_{\mathrm{tar}} = 959(11)\ [\mu\mathrm{m}] \tag{4.18}$$

and the constants determined by the target material and Avogadro's constant,

$$M_{\mathrm{tar}} = 196.97\ [\mathrm{g/mol}] \tag{5.22}$$

$$\rho_{\mathrm{tar}} = 19.32\ [\mathrm{g/cm^3}] \tag{5.23}$$

$$N_{\mathrm{A}} = 6.02214076 \times 10^{23} \tag{5.24}$$

then,

$$C_{\mathrm{tar}} = 176.5(21)\ [\mathrm{b}] \tag{5.25}$$

can be expressed as follows. Using this, in the experiments using this target in this study, the reaction cross section σ_{reac} is

$$\sigma_{\mathrm{reac}} = \frac{N_{\mathrm{reac}}}{N_{\mathrm{beam}}} C_{\mathrm{tar}} \tag{5.26}$$

5.8.2 Number of incident beam particles N_{beam}

As obtained in Table 4.5, the number of beam particles used was

$$N_{\mathrm{beam}}(^{56}\mathrm{Ti}) = 13.329 \times 10^{7} \tag{5.27}$$

$$N_{\mathrm{beam}}(^{58}\mathrm{Ti}) = 9.664 \times 10^{7} \tag{5.28}$$

5.8.3 Gamma-ray emission cross section

In the formula (5.26) for the reaction cross section σ_{reac}, by replacing σ_{reac} with σ_{γ} and N_{reac} with N_{γ}, by substituting (5.16) - (5.19), (5.27), (5.28), the gamma-ray emission cross section is calculated as

$$\sigma_{\gamma}(^{56}\mathrm{Ti}, \mathrm{Main}) = 107(13)\ [\mathrm{mb}] \tag{5.29}$$

$$\sigma_{\gamma}(^{56}\mathrm{Ti}, \mathrm{Sub}\ ) = 7(6)\ [\mathrm{mb}] \tag{5.30}$$

$$\sigma_{\gamma}(^{58}\mathrm{Ti}, \mathrm{Main}) = 97(12)\ [\mathrm{mb}] \tag{5.31}$$

$$\sigma_{\gamma}(^{58}\mathrm{Ti}, \mathrm{Sub}\ ) = 22(7)\ [\mathrm{mb}] \tag{5.32}$$

5.9 Cross section derivation (2) – Feeding correction

5.9.1 Effect of feeding on Coulomb excitation cross section measurements

In this thesis, we performed an experiment aimed at obtaining the Coulomb excitation cross section to $0^+_{\text{g.s.}} \rightarrow 2^+_1$. However, what was actually measured was the de-excitation gamma-ray emission cross section of $2^+_1 \rightarrow 0^+_{\text{g.s.}}$. It should be noted here that in the presence of "feeding" [*1)], which is the contribution from cascade decay from higher excited levels, $\sigma_{0^+\rightarrow 2^+} < \sigma_{2^+\rightarrow 0^+}$.

As shown in the example in Figure 5.14, if there are three levels, 0^+, 2^+, and 4^+, the gamma decay yield $Y_{2^+\rightarrow 0^+}$ of $2^+ \rightarrow 0^+$ is expressed as the sum of the Coulomb excitation yields $Y_{0^+\rightarrow 2^+}$ and $Y_{0^+\rightarrow 4^+}$ because it contains a cascade decay component. Therefore, in this case, to obtain $Y_{0^+\rightarrow 2^+}$ from the observable, we calculate $Y_{2^+\rightarrow 0^+} - Y_{4^+\rightarrow 2^+}$. The ratio of the level of interest that is created by feeding rather than direct excitation from the ground state, such as $0^+ \rightarrow 4^+ \rightarrow 2^+$, is called the feeding ratio.

5.9.2 Feeding ratio of nuclei near ^{56}Ti / ^{58}Ti

Let us estimate the feeding ratio of nuclei in the vicinity of ^{56}Ti / ^{58}Ti whose excitation levels are well known. Here, we performed calculations for ^{54}Cr and ^{62}Ni. Assume that only E2 transitions due to Coulomb excitation up to 3.5 MeV are considered, and multiple excitation does not occur. Details are given in the appendix E.1. As a result of the calculation, the feeding ratios of ^{54}Cr and ^{62}Ni were found to be 2.4 % and 3.0 %.

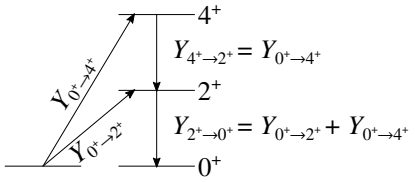

Figure 5.14: The Coulomb excitation yields are $Y_{0^+\rightarrow 2^+}$, $Y_{0^+\rightarrow 4^+}$, and the gamma ray yields are $Y_{4^+\rightarrow 2^+}$, $Y_{2^+\rightarrow 0^+}$. $Y_{2^+\rightarrow 0^+}$ includes a feeding component from the 4^+ level.

[*1)] In most literature on gamma ray metrology, the creation of the excited state of interest by a transition from a higher state is referred to as "feed(ing)".

5.9.3 Feeding ratio of ^{56}Ti / ^{58}Ti

In ^{56}Ti / ^{58}Ti, the spin and parity of many known levels have not been determined, and there are only a few examples of measurements of transition strength between levels, including the one performed in this study, so there is a lack of information necessary to calculate the feeding rate. Here, we consider the Sub peak as a transition that may feed into the 2^+_1 level.

5.9.4 The case when the sub peak fully feeds the main peak

As shown in the left figure, this is the case when the transition of the sub peak feeds into the 2^+_1 level. In this case, to obtain the Coulomb excitation cross section of $0^+_{\text{g.s.}} \rightarrow 2^+_1$, it is necessary to subtract the contribution due to feeding from the gamma-ray emission cross section of $2^+_1 \rightarrow 0^+_{\text{g.s.}}$. Therefore, if the Coulomb excitation cross section of $0^+_{\text{g.s.}} \rightarrow 2^+_1$ is $\sigma_{\text{full-feed}}$, it can be expressed as follows:

$$\sigma_{\text{full-feed}} = \sigma_\gamma(\text{Main}) - \sigma_\gamma(\text{Sub}) \tag{5.33}$$

In this study, the sub peak coincides with the energy of the known gamma-ray transition $(4^+_1) \rightarrow 2^+_1$, so it is most natural to assume this is the case.

However, when calculating the feeding ratio assuming this case, ^{56}Ti / ^{58}Ti are 7.1 % and 22.5 %, respectively, and ^{58}Ti in particular is too different from the neighboring nuclei. This suggests the possibility of a sudden change in the excited level structure, but if this is the case, it may be an unknown transition close to the energy of $(4^+_1) \rightarrow 2^+_1$, and it does not necessarily mean that it feeds to the 2^+_1 level.

5.9.5 The case when the sub peak does not feed the main peak

One possibility when the gamma ray of the sub-peak is an unknown transition is that it is independent of the transition $2^+_1 \rightarrow 0^+_{\text{g.s.}}$ and has no cascade relationship

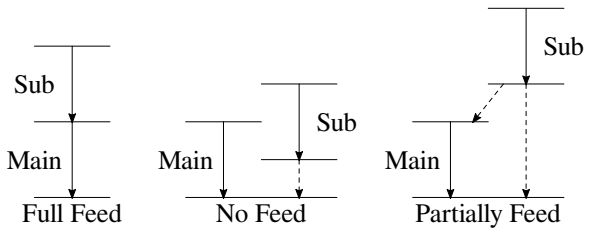

Figure 5.15: Level schemes for Full feed, No feed and Partially feed cases. The schemes for No feed and Partially feed are examples only and may vary in practice.

with it. This is illustrated in the center of Figure 5.15.

In this case, the Coulomb excitation cross section of $0^+_{\text{g.s.}} \rightarrow 2^+_1$, $\sigma_{\text{no-feed}}$, is expressed as follows:

$$\sigma_{\text{no-feed}} = \sigma_\gamma(\text{Main}) \tag{5.34}$$

5.9.6 The case when the sub peak partially feeds the main peak

Another possibility is that some of the gamma-ray transitions of the sub-peak may feed into the 2^+_1 level. The level scheme in which this may occur is shown on the right of Figure 5.15. Another possibility is that the sub-peak overlaps with multiple peaks of close energy.

In this case, the Coulomb excitation cross section $\sigma_{\text{partial-feed}}$ of $0^+_{\text{g.s.}} \rightarrow 2^+_1$ can be expressed as follows, using the Branching ratio B ($0 \leqq B \leqq 1$) :

$$\sigma_{\text{partial-feed}} = \sigma_\gamma(\text{Main}) - B\sigma_\gamma(\text{Sub}) \tag{5.35}$$

Here, there is no way to know the value of B. When $B = 0$ and $B = 1$, they correspond to $\sigma_{\text{no-feed}}$ and $\sigma_{\text{full-feed}}$, respectively. Therefore, if we want to take all possibilities into account, we set the error of B large and do the following:

$$\begin{aligned} \sigma_{\text{max-err}} &= \sigma_\gamma(\text{Main}) - B_{\text{max-err}}\sigma_\gamma(\text{Sub}) \\ B_{\text{max-err}} &= 0.5 \pm 0.5 \end{aligned} \tag{5.36}$$

5.10 Cross section derivation (3) – Coulomb excitation cross section

In the previous section, we introduced three methods for calculating the Coulomb excitation cross section for different feeding rates. The results for each case are shown in Table 5.1.

Table 5.1: Coulomb excitation cross sections derived each feeding ratios.

	^{56}Ti	^{58}Ti
$\sigma_{\text{full-feed}}$ [mb]	100(14)	75(14)
$\sigma_{\text{no-feed}}$ [mb]	107(13)	97(12)
$\sigma_{\text{max-err}}$ [mb]	104(14)	86(17)

From here on, we will basically use $\sigma_{\text{max-err}}$, which includes all feeding cases, and set $\sigma_{\text{coulex}} \equiv \sigma_{\text{max-err}}$.

Chapter 6

Evaluating the analysis results

6.1 Derivation of $B(\mathrm{E2})$ from σ_{coulex} (1)

6.1.1 Policy

In principle, $B(\mathrm{E2})$ can be obtained from the Coulomb excitation cross section using the relationship shown in formula (B.4), but it is not easy to calculate by hand, especially the part to obtain the virtual photon number N_γ. Therefore, we use the distorted wave Born approximation (DWBA) calculation code Fresco [59,60].

6.1.2 DWBA

The distorted wave Born approximation (DWBA) is a method used in scattering theory that is suitable for describing complex scattering systems. It is an improvement over the simple Born approximation (plane wave Born approximation) to handle cases where the target or scatterer has a strong potential. Details are given in the appendix F. In the measurements using the gold target in this study, the velocity of the incident nuclei is fast, so atomic nuclei may collide with each other. Thus, although the contribution from Coulomb excitation is dominant, excitation from inelastic scattering may also occur. Taking this into account, it should be noted that the measured cross section is the sum of both Coulomb excitation and inelastic scattering.

6.2 DWBA calculation code "Fresco"

6.2.1 Overview

By inputting the optical potential and nuclear reaction characteristics, the expected total cross section and differential scattering cross section for each scattering angle can be calculated. Here, we aim to obtain the value of $B(\mathrm{E2})$ by appropriately providing characteristics related to $B(\mathrm{E2})$ and adjusting them to reproduce the Coulomb excitation cross section from the experimental results.

6.2.2 Input parameter values

For the Fresco calculations, we used the nuclear deformation length δ_{N} and the reduced matrix element $M(\mathrm{E2})$ as variables to find a combination that would reproduce the Coulomb excitation cross section from the experimental results. In addition, we appropriately input various necessary values, such as the optical potential required for the calculation and the beam energy during the experiment.

6.2.3 Results

The cross sections of 2^+ excitation in Au(^{56}Ti,^{56} Ti) and Au(^{58}Ti,^{58} Ti) obtained by setting δ_{N} and $M(\mathrm{E2})$ in the appropriate range are shown in figure 6.1. The Coulomb excitation cross sections (see Table 5.1) obtained experimentally are superimposed in the figure.

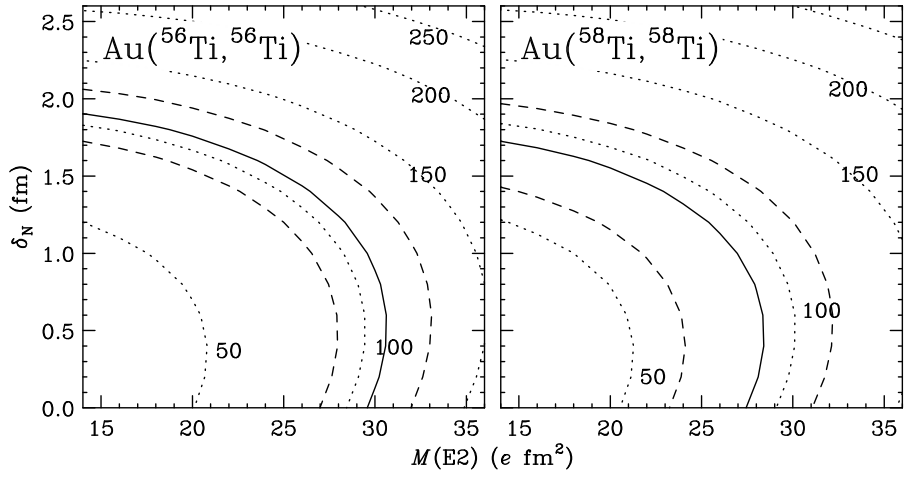

Figure 6.1: The cross section calculated by Fresco is overlaid on the experimental cross section. The experimental results are shown with a solid line representing the center value and a dashed line representing the error range.

6.3 Derivation of $B(\mathrm{E2})$ from σ_{coulex} (2)

6.3.1 Relationship between $M(\mathrm{E2})$, $B(\mathrm{E2})$ and δ_N

In appendix A,

$$B(\mathrm{E2}; 0^+ \rightarrow 2^+) = \beta_2^2 \left(\frac{3}{4\pi} Z e R_0^2 \right)^2 \tag{A.8}$$

$$\delta = \beta_2 R_0 \tag{A.9}$$

In addition, the relationship between the reduced matrix elements $\langle j_f || M_L^{(\mathrm{E})} || j_i \rangle \equiv M(\mathrm{E2})$ and $B(\mathrm{E2})$ for the $0^+ \rightarrow 2^+$ transition is: *1)

$$B(\mathrm{E2}; 0^+ \rightarrow 2^+) = |M(\mathrm{E2})|^2 \tag{6.1}$$

From these, the following relationship holds between δ and $M(\mathrm{E2})$:

$$\delta = \frac{4\pi}{3ZR} M(E2) \tag{6.2}$$

Here, it should be noted that the deformation length δ is a quantity related by the reduced electric quadrupole transition probability $B(\mathrm{E2})$, which is a deformation that is effective for electromagnetic interactions, that is, a deformation that focuses only on the proton distribution. The input in Fresco is the deformation length δ_{N} of the entire nucleus, including both protons and neutrons, and in this analysis, we consider $\delta = \delta_{\mathrm{N}}$, which is actually almost equal for most nuclei.

This relation also includes the nuclear radius R. Here, R is the nuclear radius when the atomic nucleus is considered to be a uniformly distributed sphere. R can generally be described by the nuclear radius formula (H.2), but its uncertainty will be discussed in the next section.

6.3.2 Estimation of nuclear radius R

In Fresco, the nucleus is treated as a uniformly charged sphere, and calculations are performed using the nuclear radius R obtained by decomposing the input δ_{N}.

Now, when using the relationship between δ_{N} and $M(\mathrm{E2})$ in equation (6.2), an accurate nuclear radius R is required.

In the appendix H, the nuclear radius R for ^{56}Ti and ^{58}Ti is estimated.

$$R(^{56}\mathrm{Ti}) = 4.94(37)\ [\mathrm{fm}] \tag{H.14}$$

*1) See AppendixG.

$$R(^{58}\mathrm{Ti}) = 5.04(49)\ [\mathrm{fm}] \tag{H.15}$$

6.4 Derivation of $B(\mathrm{E2})$ from σ_{coulex} (3)

6.4.1 Determining $B(\mathrm{E2})$ using the nuclear radius R

The relationship between δ_{N} and $M(\mathrm{E2})$ obtained by substituting the nuclear radii (H.14) and (H.15) obtained in the analysis in section 6.3.2 into equation (6.2) is shown in Figure 6.2, superimposed on the figure 6.1 obtained in section 6.2.3. The experimental Coulomb excitation cross section and the range of $(M(\mathrm{E2}), \delta_{\mathrm{N}})$ limited by the nuclear radius are shaded in black. From the black areas in this figure, we obtain the following for each $M(\mathrm{E2})$ values. Converting these to $B(\mathrm{E2})$ using equation (G.2), the values are summarized in Table 6.1.

Table 6.1: Obtained $B(\mathrm{E2})$ values.

	$B_{\mathrm{no-feed}}(\mathrm{E2})\uparrow$		$B_{\mathrm{full-feed}}(\mathrm{E2})\uparrow$		$B_{\mathrm{max-err}}(\mathrm{E2})\uparrow$	
	$[e^2\mathrm{fm}^4]$	[W.u.]	$[e^2\mathrm{fm}^4]$	[W.u.]	$[e^2\mathrm{fm}^4]$	[W.u.]
^{56}Ti	822 (88)	12.9 (14)	768 (93)	12.1 (15)	799 (93)	12.6 (15)
^{58}Ti	779 (90)	11.7 (14)	599 (96)	9.0 (15)	688 (116)	10.3 (18)

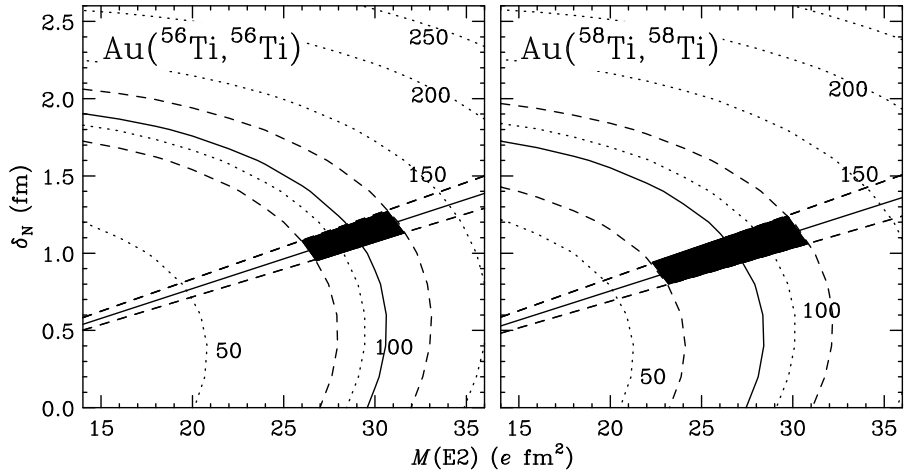

Figure 6.2: The experimental results and the limiting range due to the nuclear radius are superimposed on the Fresco calculation results shown in Figure 6.1. As with the experimental results for the cross section, the nuclear radius is also shown with a solid line representing the center value and a dashed line representing the error range.

Chapter 7

Discussion and conclusions

7.1 Comparison with previous experimental and theoretical B(E2)

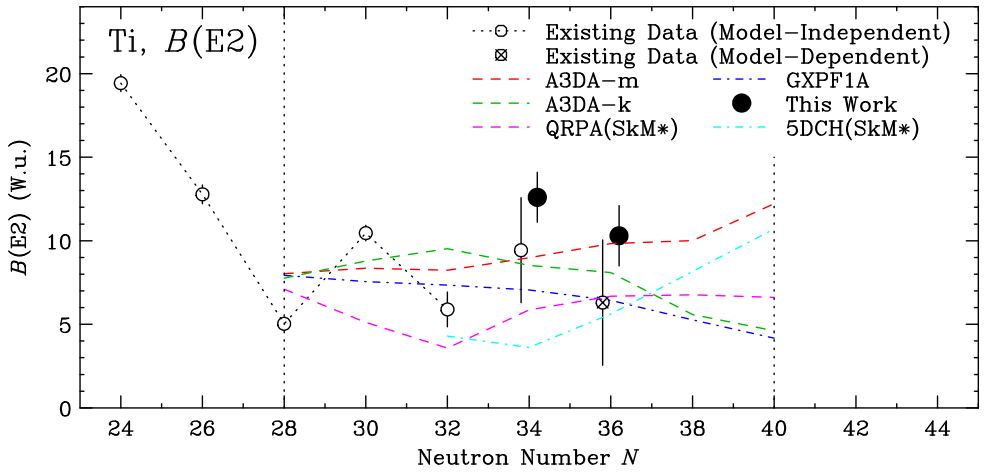

Figure 7.1: Experimental and theoretical B(E2) values for Ti isotopes. The experimental values obtained in this work are shown as filled circles.

7.1.1 Comparison with previous experimental values

The B(E2) values obtained in this work are presented in Fig. 7.1 as filled circles, together with the values obtained in previous works. For the case of ^{56}Ti (N = 34), the previous experimental value was obtained from Coulomb excitation at NSCL. The present result lies close to the upper limit of the earlier measurement and is consistent with it within the experimental uncertainties. For ^{58}Ti (N = 36), the earlier value was deduced from (p, p') scattering at RIKEN. In that experiment, the deformation length δ was measured rather than the B(E2) value itself, and the B(E2) strength is converted to the B(E2) value using Eq. (A.9), assuming that the

δ values are the same for protons and neutrons. The value obtained in the present work is also located near the upper limit of the previous result and agrees with it within the uncertainties. It should be emphasized that the uncertainties of the present measurements are reduced to about half of those in earlier studies. In particular, the error bar for $N = 34$ has been significantly reduced, clearly showing that its $B(\mathrm{E2})$ value is substantially larger than that of $N = 32$.

7.1.2 Comparison with shell model calculations

In Fig. 7.1, we show the results of the shell-model calculations with GXPF1A and A3DA-m, as well as the results of the A3DA-k calculation. In order to examine the effect of the tensor component on the $N = 40$ magicity, the A3DA-k calculation is based on A3DA-m but excludes the tensor component. By excluding the tensor component, the calculation keeps the energy difference between the $\nu f_{5/2}$ and $\nu g_{9/2}$ orbitals at $N = 40$ large, i.e., the shell gap at Ni ($Z = 28$) is maintained down to Ca ($Z = 20$). Among these three shell-model calculations, A3DA-m shows the best agreement with our experimental data.

As shown in Fig. 1.7, previously measured $B(\mathrm{E2})$ values in Fe and Cr isotopes were also well reproduced by A3DA-m. Although the A3DA-k calculations are not shown in this figure, they generally underestimate these values due to the absence of the tensor-force effect that reduces the shell gap. Our present results for Ti isotopes thus follow the same systematic trend as A3DA-m, further confirming the robustness of this model description.

7.1.3 Comparison with Self-consistent QRPA models based on Skyrme EDF

Both the QRPA (SkM*) and 5DCH (SkM*) calculations deviate from the experimental values obtained for ^{56}Ti and ^{58}Ti in this work by more than approximately twice the experimental uncertainties. Notably, the 5DCH (SkM*) results tend to approach those of the A3DA-m calculation for $N \geqq 38$, which highlights the potential interest in obtaining additional experimental data for comparison with the 5DCH (SkM*) predictions.

7.2 Interpreting A3DA-m agreement across three shell-model calculations

In this study, the experimental results were compared with three shell-model calculations, namely GXPF1A, A3DA-m, and A3DA-k. It was found that A3DA-m provides the best agreement, particularly for ^{58}Ti. The essential features of these

interactions can be summarized as follows:

- GXPF1A: restricted to the pf-shell model space
- A3DA-m: extended model space including the pf-shell and the $g_{9/2}$ orbital
- A3DA-k: same model space as A3DA-m but without the tensor force

The calculated $B(\mathrm{E2})$ values obtained from these three models begin to diverge for nuclei beyond $N \sim 36$. In the following discussion, we focus on the evolution of the $N = 40$ shell gap and the neutron excitations across this gap in order to interpret these differences.

7.2.1 Evolution of the $N = 40$ shell gap

To investigate the evolution of the $N = 40$ shell gap, the effective single-particle energies (ESPEs) obtained with the A3DA-m and A3DA-k interactions are shown in Fig. 7.2. Since the GXPF1A interaction does not include orbitals above the $g_{9/2}$ shell, the $N = 40$ shell gap is effectively treated as infinitely large in this framework.

A comparison between A3DA-m and A3DA-k reveals distinct behaviors in the $f_{5/2}$ and $g_{9/2}$ orbitals, which are strongly affected by the tensor force. In the A3DA-m calculation, these two orbitals approach each other as the proton number Z decreases. Notably, for $Z \lesssim 24$, where the $p_{1/2}$ and $f_{5/2}$ orbitals invert, the $N = 40$ shell gap shrinks rapidly. In contrast, the A3DA-k results exhibit a rather different trend. Here, the separation between the $f_{5/2}$ and $g_{9/2}$ orbitals remains nearly unchanged, and the $p_{1/2}$ orbital does not show a marked change relative to the $f_{5/2}$. Consequently, the

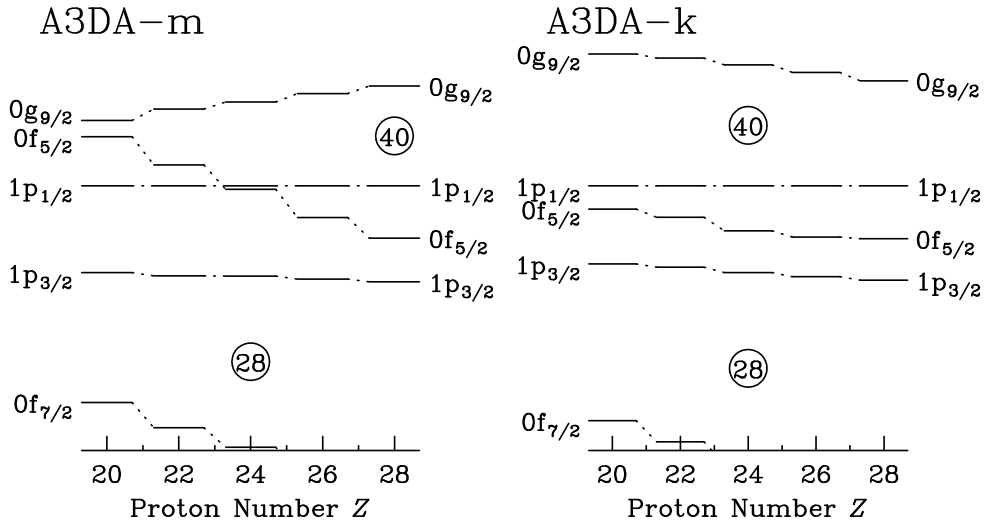

Figure 7.2: The evolution of the neutron effective single-particle energies (ESPEs) as a function of proton number is shown for the two A3DA models. In both cases, the values correspond to the $N = 40$ isotones and are given relative to the $1p_{1/2}$ orbital.

$N = 40$ shell gap does not shrink toward smaller Z, which is consistent with the situation expected in the absence of the strong tensor-force effect that characterizes A3DA-m.

7.2.2 Neutron excitations across $N = 40$ shell gap

Figure 7.3 shows the calculated expectation values of the neutron occupation number in the $g_{9/2}$ orbital for Ti and Ni isotopes, obtained with both the A3DA-m and A3DA-k interactions. Since the $g_{9/2}$ orbital is the first orbital located above the $N = 40$ shell gap, these values can be interpreted as the number of neutrons excited across the $N = 40$ gap.

For comparison, it should be noted that the GXPF1A interaction does not include the $g_{9/2}$ orbital in its model space. Consequently, if such an occupation number were evaluated within GXPF1A, it would trivially remain zero.

In the case of A3DA-k, the results for Ti and Ni are nearly identical. For $N \leq 40$, the occupation remains below one, indicating that excitations into the $g_{9/2}$ orbital are suppressed by the $N = 40$ shell gap and that filling of this orbital does not begin until the neutron number exceeds 40.

By contrast, the A3DA-m results show a clear difference between Ti and Ni. While Ni exhibits nearly the same behavior as in A3DA-k, the Ti isotopes display a rapid increase in $g_{9/2}$ occupation starting around $N = 34$, and the expectation value

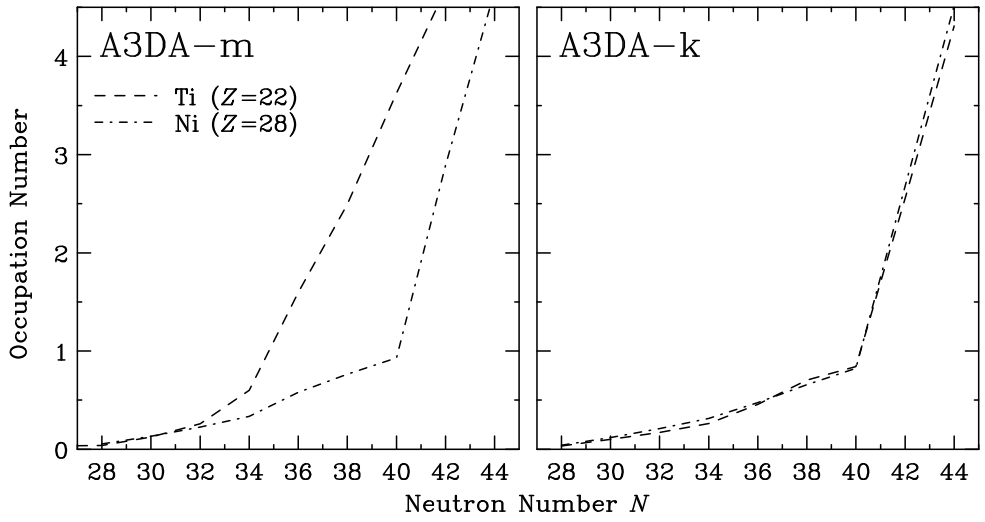

Figure 7.3: The evolution of the neutron $0g_{9/2}$ orbital occupation numbers as a function of neutron number is shown for the two A3DA models. In both calculations, Ni isotopes exhibit values below unity for $N \leq 40$. In contrast, for Ti isotopes within the A3DA-m model, the occupation number already exceeds unity at $N = 36$. For A3DA-k, however, the Ti isotopes follow nearly the same trend as Ni, with the two curves essentially overlapping.

already exceeds one at $N = 36$. This suggests that, in Ti isotopes, the hindrance of excitations into the $g_{9/2}$ orbital due to the $N = 40$ shell gap is significantly weakened, allowing neutrons to exicite to this orbital more easily.

The agreement of the A3DA-m calculation with experimental data for ^{58}Ti further supports this interpretation, suggesting that excitations across the $N = 40$ shell gap are already active in this nucleus. In contrast to Ni isotopes, where the $N = 40$ shell gap effectively suppresses excitations into the $g_{9/2}$ orbital and thus exhibits a magicity, Ti isotopes demonstrate a clear weakening of this nature.

7.3 Summary

In this thesis, the evolution of nuclear collectivity around $N = 40$ has been investigated through measurements of $B(\mathrm{E2})$ in neutron-rich Ti isotopes. The aims were (i) to examine whether the $N = 40$ shell gap in ^{58}Ti acts to hinder nucleon excitations across the gap into the $g_{9/2}$ orbital and above, thereby reflecting a magic-like nature, and (ii) to clarify the mechanism driving enhanced collectivity around ^{64}Cr. The experiment was performed at the RIBF facility of RIKEN using intermediate-energy Coulomb excitation on a gold target, which enabled extraction of $B(\mathrm{E2})$ values with significantly improved precision and reduced model dependence compared with previous studies.

The new results for ^{56}Ti and ^{58}Ti yield $B(\mathrm{E2}; 0^+ \rightarrow 2^+)$ values of 799(93) and 688(116) $e^2\mathrm{fm}^4$, (12.6(15) and 10.3(18) W.u.) respectively. These values are consistent with previous studies but with uncertainties reduced by about half. Together with the smaller value of 357(63) $e^2\mathrm{fm}^4$ (5.9(10) W.u.) known for ^{54}Ti, the present measurements indicate a clear trend of increasing quadrupole collectivity toward $N = 40$. These results provide clear experimental indications of the onset of collectivity in this region, in agreement with theoretical predictions that incorporate the effect of the tensor force.

Comparison with theoretical models shows that the A3DA-m shell-model calculation, which includes the tensor force and the $g_{9/2}$ orbital, reproduces the data best. In contrast, GXPF1A (restricted to the pf shell) and A3DA-k (without the tensor force) fail to capture the observed trends. The results support the picture that the tensor force reduces the $N = 40$ shell gap in Ti isotopes, allowing neutrons to occupy the $g_{9/2}$ orbital already at $N = 36$. Thus, while ^{68}Ni retains a clear $N = 40$ magicity, this is strongly weakened in ^{58}Ti.

This interpretation is consistent with the enhanced collectivity observed in Fe and Cr isotopes around $N = 40$. The tensor-force–driven reduction of the $N = 40$

shell gap provides a unified explanation for the increasing quadrupole collectivity observed in Ti, Cr, and Fe isotopes around $N = 40$. The present measurements of Ti isotopes have helped clarify the underlying mechanism responsible for this enhanced collectivity in Fe and Cr.

The present work highlights the importance of tensor-force effects in shell evolution and establishes Ti isotopes as a key testing ground for the $N = 40$ region. Future measurements of ^{62}Ti, and ultimately of ^{60}Ca, are crucial for testing whether the $N = 40$ shell gap becomes very small as predicted by some models, or remains sizable as suggested by others, thereby providing decisive insights into the interplay between shell structure and collectivity.

In summary, precise new $B(\mathrm{E2})$ values for ^{56,58}Ti have been obtained, demonstrating that the $N = 40$ shell closure weakens markedly toward lower Z. This finding explains the onset of strong collectivity near ^{64}Cr and advances our understanding of magic-number breaking in neutron-rich nuclei.

Appendix A

Deformation quantities β_2 and δ

The deformation parameter β_2 for the quadrupole deformation is defined by the coefficient when expressing the shape of the nuclear surface as a linear sum of spherical harmonic functions $Y_{lm}(\theta, \phi)$. Written in a generalized form, this is expressed as follows,

$$R(\theta, \phi) = R_0 \left[1 + \sum_{lm} \alpha_{lm} Y_{lm}(\theta, \phi) \right] \tag{A.1}$$

using the nuclear radius R_0 and the coefficient α_{lm}. [*1)] In the case of $l = 2$,

$$R(\theta, \phi) = R_0 \{ 1 + a_{20} Y_{20}(\theta, \phi) + a_{22} [Y_{22}(\theta, \phi) + Y_{2-2}(\theta, \phi)] \} \tag{A.2}$$

can be expanded as follows,

$$a_{20} \equiv \beta_2 \cos\gamma \tag{A.3}$$

$$a_{22} \equiv \frac{1}{\sqrt{2}} \beta_2 \sin\gamma \tag{A.4}$$

and, if $\gamma = 0$, $a_{20} = \beta$, $a_{22} = 0$, so :

$$R(\theta, \phi) = R_0 [1 + \beta_2 \, Y_{20}(\theta, \phi)] \tag{A.5}$$

Also,

$$Y_{20}(\theta, \phi) = \sqrt{\frac{5}{16\pi}} (3\cos^2\theta - 1) \tag{A.6}$$

[*1)] See textbook [61] p250, equation (31.9), etc.

so the equation (A.5) is :

$$R(\theta) = R_0 \left[1 + \sqrt{\frac{5}{16\pi}}\, \beta_2 (3\cos^2\theta - 1) \right] \tag{A.7}$$

In addition, the relationship between $B(\mathrm{E2})$ and the degree of deformation β_2 is expressed as follows: *1)

$$B(\mathrm{E2}; 0^+ \rightarrow 2^+) = \beta_2^2 \left(\frac{3}{4\pi} Z e R_0^2 \right)^2 \tag{A.8}$$

The deformation length δ is defined as follows:

$$\delta = \beta_2 R_0 \tag{A.9}$$

It can be obtained by measuring the inelastic scattering cross section.

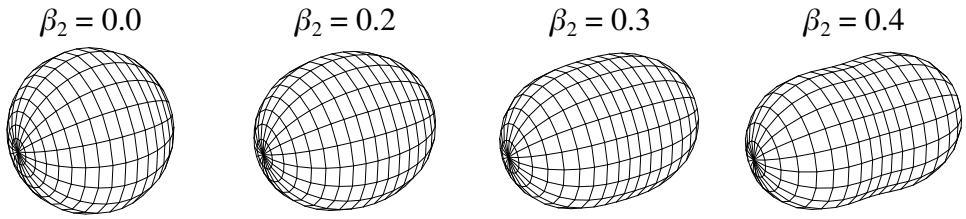

Figure A.1: The deformation parameter β_2 is varied from 0.0 to 0.4, and the deformation parameter is drawn in three dimensions. Most of the deformed kernels have a deformation parameter of about β_2 = 0.2 - 0.3, and the superdeformed kernels, whose major axis to minor axis ratio is 2:1, have a deformation parameter of $\beta_2 \sim 0.6$.

*1) See textbook [61] p252, equation (31.19), etc.

Appendix B

Virtual photon number in Coulex

The Coulomb excitation cross section σ of $0^+ \rightarrow 2^+$ can be written as follows by substituting $\pi\lambda$ = E2 from [62] :

$$\sigma = \int \frac{1}{E_x} n_{\mathrm{E2}}(E_x)\, \sigma_\gamma^{\mathrm{E2}}(E_x)\, dE_x \tag{B.1}$$

Differentiating both sides of this with respect to the excitation energy E_x, we get :

$$\frac{d\sigma}{dE_x} = \frac{1}{E_x} n_{\mathrm{E2}}(E_x)\, \sigma_\gamma^{\mathrm{E2}}(E_x) \tag{B.2}$$

In addition, the optical absorption cross section $\sigma_\gamma^{\mathrm{E2}}(E_x)$ is given by [62] as follows:

$$\sigma_\gamma^{\mathrm{E2}}(E_x) = \frac{(2\pi)^3(2+1)}{2\left[(2\cdot 2+1)!!\right]^2} \left(\frac{E_x}{\hbar c}\right)^{2\cdot 2-1} \frac{dB(\mathrm{E2}; E_x)}{dE_x} \tag{B.3}$$

Therefore, by substituting this, and taking the coefficient that does not depend on E_x as C, and integrating both sides with respect to E_x, we get :

$$\sigma = C\, n_{\mathrm{E2}}(E_x)\, E_x^2\, B(\mathrm{E2}; E_x) \tag{B.4}$$

Here, $\sigma_\gamma^{\mathrm{E2}}(E_x)$ is the optical absorption cross section. Also, when considering the excitation cross section to a specific 2^+ excitation level where $E_x = E_0$, it can be replaced with $B(\mathrm{E2}; E_x) \rightarrow \delta(E_x - E_0)B(\mathrm{E2})$, from which we can say :

$$\sigma \propto n_{\mathrm{E2}}(E_x) \cdot E_x^2 \cdot B(\mathrm{E2}) \tag{B.5}$$

The number of virtual photons n_{E2} generated by Coulomb excitation accompanied

by the E2 transition is given by equation (2.5.5c) in [63]:

$$n_{\mathrm{E2}}(\omega) = \frac{2}{\pi} Z_1^2 \alpha \left(\frac{c}{v}\right)^4 \times \left[2\left(1 - \frac{v^2}{c^2}\right) K_1^2 + \xi \left(2 - \frac{v^2}{c^2}\right)^2 K_0 K_1 - \frac{\xi^2 v^4}{2c^4}\left(K_1^2 - K_0^2\right)\right] \tag{B.6}$$

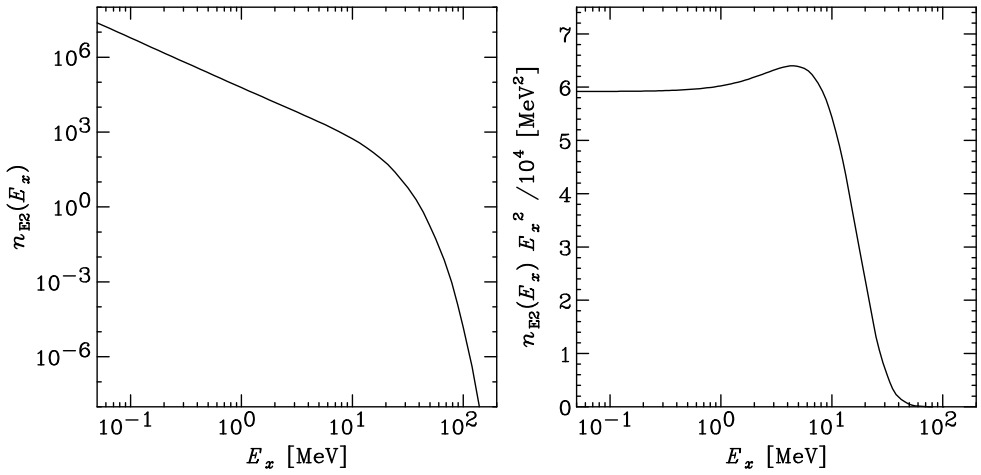

Figure B.1: Energy dependence of the number of virtual photons (left) and its multiplication by the square of the excitation energy E_x (right). It is almost constant in the range below $E_x \sim 10$ MeV.

Appendix C

Beam transport matrix

As an example, the beam transport matrix between the F3 and F5 focal planes can be written as follows:

$$\begin{pmatrix} x_5 \\ a_5 \\ \delta_{35} \end{pmatrix} = \begin{pmatrix} (x|x) & (x|a) & (x|\delta) \\ (a|x) & (a|a) & (a|\delta) \\ 0 & 0 & 1 \end{pmatrix} \begin{pmatrix} x_3 \\ a_3 \\ \delta_{35} \end{pmatrix} \tag{C.1}$$

The third-order square matrix in this equation is called the "first-order transport matrix." The matrix elements $(x|x)$, $(x|a)$... are determined by the materials such as magnets and detectors installed in the beamline, and are constants unless the experimental setup is changed.

As a very simplified example, if there were no material or magnetic field between F3 and F5, the equation (C.1) would be:

$$\begin{pmatrix} x_5 \\ a_5 \\ \delta_{35} \end{pmatrix} = \begin{pmatrix} 1 & 0 & (x|\delta) \\ 0 & 1 & 0 \\ 0 & 0 & 1 \end{pmatrix} \begin{pmatrix} x_3 \\ a_3 \\ \delta_{35} \end{pmatrix} \tag{C.2}$$

When we solve this, then:

$$x_5 = (x|\delta) \cdot \delta_{35} + x_5 \tag{C.3}$$

$$a_5 = a_3 \tag{C.4}$$

What this means is that a particle that arrives at F3 at a finite angle will continue to F5 without changing its angle, and the amount of displacement it experiences while reaching F5 is proportional to δ_{35}, with the coefficient $(x|\delta)$.

Appendix D

Angular distribution of gamma rays

It is well known that the emission angles of two gamma rays, 1173 keV and 1332 keV, emitted from a ^{60}Co gamma ray source are correlated. This is because the direction of the angular momentum of the excited state has a non-isotropic distribution with respect to the quantization axis. In experiments using beams accelerated by an accelerator, the quantization axis is aligned perpendicular to the beam direction. Therefore, the direction of the gamma rays emitted when the beam particles excited by interaction with the target are de-excited may have an angular distribution with respect to the beam axis direction. In general, the angular distribution $W(\theta)$ of gamma-ray emission at an angle θ with respect to the quantization axis can be expressed as a linear sum of Legendre functions $P_k(\cos\theta)$ [64],

$$W(\theta) = \sum_k a_k P_k(\cos\theta) \tag{D.1}$$

Here, a_k is expressed by using the "Population parameter" $P(m)$ as follows:

$$\begin{aligned} a_k &= \frac{-1}{4\pi}\langle \lambda\ 1\ \lambda\ -1|k\ 0\rangle \\ &\times \sum_{m_i,\mu}(-)^{\mu}\langle \lambda\ \mu\ \lambda\ -\mu|k\ 0\rangle\ |\langle j_i\ m_i\ \lambda\ \mu|j_f\ m_f\rangle|^2\ P(m_i) \end{aligned} \tag{D.2}$$

$P(m)$ is the probability that the state with magnetic quantum number m is occupied, and can be estimated by the semiclassical theory of Coulomb excitation [65].

In addition, $\langle j_1\ m_1\ j_2\ m_2|j_3\ m_3\rangle$ in the formula is the Clebsch-Gordan coefficient. m_i, m_f are the magnetic quantum numbers of the initial and final states, respectively. For the $2^+ \rightarrow 0^+$ transition, $m_i = -2, -1, 0, 1, 2$, and $m_f = 0$. j_i, j_f are the angular momentum of the initial and final states, and similarly, $j_i = 2$, $j_f = 0$. Also, μ, k are $\mu = -m_i$, and $k = 0, 2, 4$, according to the Clebsch-Gordan coefficient convention.

From this, in the case of $2^+ \rightarrow 0^+$ transition is:

$$W(\theta) = a_0 P_0(\cos\theta) + a_2 P_2(\cos\theta) + a_4 P_4(\cos\theta) \quad \text{(D.3)}$$

$$a_k = \frac{-1}{4\pi}\langle 2\ 1\ 2\ -1|k\ 0\rangle \times \sum_{m_i=-2}^{2} (-)^{-m_i}\langle 2-m_i\ 2\ m_i|k\ 0\rangle\ |\langle 2\ m_i\ 2\ -m_i|0\ 0\rangle|^2\ P(m_i) \quad \text{(D.4)}$$

The results of calculating $P(m_i)$ according to the experimental conditions are summarized in Table D.1. Figure 5.9 shows $W(\theta)$ calculated using these $P(m_i)$. The UCHiCARI simulation code makes it possible to reproduce the angular distribution of gamma rays emitted during the experiment by inputting the values of a_0, a_2, a_4.

Table D.1: Calculation results for $P(m_i)$. The 2^+ excitation energies are 1.129 MeV (^{56}Ti) and 1.047 MeV (^{58}Ti) according to NNDC [21]. The calculation code used was [66].

	Au(^{56}Ti,^{56} Ti) 164 MeV/u	Au(^{58}Ti,^{58} Ti) 170 MeV/u
$m_i = 2$	0.46586057	0.47002961
$m_i = 1$	0.02867217	0.02531471
$m_i = 0$	0.01093452	0.00931136
$m_i = -1$	0.02867217	0.02531471
$m_i = -2$	0.46586057	0.47002961

Appendix E

A note on feeding ratio

E.1 Feeding ratio of nearby nuclei: $^{56/58}$Ti

The number of events excited from 0^+ to 2^+ by Coulomb excitation is required to obtain the Coulomb excitation cross section. The gamma-ray peak yield, obtained above, is the number of gamma rays de-excited from 2^+ to 0^+. This includes not only events excited from 0^+ to 2^+ by Coulomb excitation, but also events excited to higher levels by other excitation processes such as inelastic scattering, resulting in the creation of the 2^+ state by cascade decay.

E.2 Example of when the Sub peak does not feed

E.2.1 Transition involving unknown levels

Although it is unlikely, we cannot deny the possibility that the gamma-ray transition of the sub-peak is not in a cascade relationship with the first 2^+ to 0^+ transition. If this is the case, as shown in Figure 3, gamma-ray emission could be (i) a gamma-ray emission associated with a transition from an unknown level to the ground level, or (ii) a gamma-ray emission associated with a transition from an unknown level to another unknown level.

E.2.2 Contamination of other nuclei

It is possible that these are gamma rays from other nuclei mixed into the beam, but particle identification has determined that the contamination of other nuclei is less than 1 %, and to reproduce the magnitude of the peak, a transition with a huge transition probability of more than several hundred times that of ^{58}Ti would be necessary, but since the level structures of nearby nuclei and the transition

probabilities between levels are relatively similar, this is unlikely in reality.

Appendix F

DWBA

The distorted wave Born approximation (DWBA) is a method used in scattering theory that is suitable for describing complex scattering systems. It is an improvement of the simple Born approximation (plane wave Born approximation) to handle cases where the target or scatterer has a strong potential. In general, the scattering differential cross section of the $\mathrm{X(a,b)Y}$ reaction can be written as follows, from equation (31.1) in the textbook [61]:

$$\frac{\mathrm{d}\sigma}{\mathrm{d}\Omega} = \frac{M_{\mathrm{aX}} M_{\mathrm{bY}}}{(2\pi\hbar^2)^2} \frac{k_b}{k_a} |T|^2 \tag{F.1}$$

Here, T is a value called the transition matrix element. M is the reduced mass, and k is the wave number. In the case of the plane wave Born approximation, the transition matrix element T is given by [61] (31.2):

$$T = \int \mathrm{e}^{-i\boldsymbol{k}_{\mathrm{b}}\cdot\boldsymbol{r}} \langle \mathrm{Y}|V|\mathrm{X}\rangle \mathrm{e}^{i\boldsymbol{k}_{\mathrm{a}}\cdot\boldsymbol{r}} \,\mathrm{d}\boldsymbol{r} \tag{F.2}$$

In PWBA, the wave distortion when two particles approach each other is ignored, and the incident wave $\exp(i\boldsymbol{k}_{\mathrm{a}} \cdot \boldsymbol{r})$ and the outgoing wave $\exp(i\boldsymbol{k}_{\mathrm{b}} \cdot \boldsymbol{r})$ are represented only as plane waves. On the other hand, in DWBA, the transition matrix element T is calculated by using the waves distorted by the optical potential $U(\boldsymbol{r})$, $\psi_{\mathrm{aX}}(\boldsymbol{k}_{\mathrm{a}}, \boldsymbol{r})$ and $\psi_{\mathrm{bY}}(\boldsymbol{k}_{\mathrm{b}}, \boldsymbol{r})$, based on equation (31.3) in the textbook [61] :

$$T = \int \psi^*_{\mathrm{bY}}(\boldsymbol{k}_{\mathrm{b}}, \boldsymbol{r}) \langle \mathrm{Y}|V|\mathrm{X}\rangle \psi_{\mathrm{aX}}(\boldsymbol{k}_{\mathrm{a}}, \boldsymbol{r}) \,\mathrm{d}\boldsymbol{r} \tag{F.3}$$

Using this, the differential cross section for inelastic scattering, $\mathrm{X(a,a')X'}$ reac-

tion, can be written as follows, according to equation (31.16) in the textbook [61]:

$$\frac{\mathrm{d}\sigma}{\mathrm{d}\Omega} = \frac{M_{\mathrm{aX}}^2}{(2\pi\hbar^2)^2}\frac{k_{\mathrm{a}'}}{k_{\mathrm{a}}}\frac{\beta_l^2}{2l+1}\left|\int \psi^*_{\mathrm{a}'\mathrm{X}'}\left(R_0\frac{\mathrm{d}U}{\mathrm{d}R_0}\right)Y_l^{m*}(\theta,\phi)\psi_{\mathrm{aX}}\,\mathrm{d}r\right|^2 \tag{F.4}$$

If we consider excitation to $0^+ \rightarrow 2^+$, since $l = 2$, the product of β_l^2 and R_0^2 in equation (F.4) is the deformation length δ^2 from equation (A.9). From this, we can see that the deformation length δ can be obtained from measuring the cross section of inelastic scattering.

In the case of pure Coulomb excitation, where the incident nucleus is slow enough that it does not collide with the target nucleus, page 146 of the textbook [67] states:

$$\frac{\mathrm{d}\sigma}{\mathrm{d}\Omega} = \frac{1}{(2J_\alpha+1)(2J_0+1)}\frac{M^2 v_b}{4\pi^2\hbar^4 v_\alpha}\left|\langle\beta||Q^{(l_0)}||\alpha\rangle\right|^2\sum_m\left|R_{l_0}^m\right|^2 \tag{F.5}$$

In the case of E2 transitions, $l_0 = 2$, and in this case, although the notation is different, $\langle\beta||Q^{(l_0)}||\alpha\rangle$ is equal to the reduced matrix element $M(E2)$. From this, $B(\mathrm{E2})$ can be obtained from the relationship between the measurement of the Coulomb excitation cross section and equation (6.2).

However, in the measurements using a gold target in this study, the velocity of the incident nucleus is fast, so atomic nuclei may collide with each other. Therefore, although the contribution from Coulomb excitation is dominant, excitation by inelastic scattering may also occur. Taking this into consideration, it is important to note that the measured cross section is the sum of both Coulomb excitation and inelastic scattering.

Appendix G

Reduced matrix elements M(E2)

In general, the reduced transition probability $B(\mathrm{E}L; j_i \rightarrow j_f)$ and the reduced matrix elements $\langle j_f || M_L^{(\mathrm{E})} || j_i \rangle$ have the following relationship:。

$$B(\mathrm{E}L; j_i \rightarrow j_f) = (2j_i + 1)^{-1} |\langle j_f || M_L^{(\mathrm{E})} || j_i \rangle|^2 \tag{G.1}$$

Therefore, $B(\mathrm{E2}; 0^+ \rightarrow 2^+)$ is,

$$\begin{aligned} B(\mathrm{E2}; 0^+ \rightarrow 2^+) &= (2 \cdot 0 + 1)^{-1} |\langle 2^+ || M_2^{(\mathrm{E})} || 0^+ \rangle|^2 \\ &= |\langle 2^+ || M_2^{(\mathrm{E})} || 0^+ \rangle|^2 \\ &= |M(E2)|^2 \end{aligned} \tag{G.2}$$

In this paper, we use $M(E2)$ as an abbreviation for $\langle 2^+ || M_2^{(\mathrm{E})} || 0^+ \rangle$.

Appendix H

Estimation of the nuclear radius *R*

H.1 Definition of nuclear radius *R*

Types of radii with different geometric sizes

- Radius of uniform density distribution R_U
- Half-maximum radius of the Fermi function distribution that incorporates the "diffuseness" of the nuclear surface R_F
- Mean squared charge radii $< r^2 >$

and others. Of these, the value measured experimentally is often $< r^2 >$. If we assume that the atomic nuclei are truly uniformly distributed, the relationship between R_U and $< r^2 >$ can be written as follows:

$$R_U = \sqrt{\frac{5}{3} < r^2 >} \tag{H.1}$$

The nuclear radius required for Fresco calculations is R_U, which will be used in subsequent calculations, so from this point on in this paper we will use $R \equiv R_U$. In addition, the radius of the nucleus can be determined by

- Charge distribution
- Nucleon (proton/neutron) distribution: point distribution of each nucleon
- (proton/neutron) nuclear matter distribution: includes effects due to the size of the nucleon itself

and so on. Of these, charge distribution is the most widely measured, and the measurement results are compiled in the database [68]. Figure H.1 plots a list of nuclear radius data published in [68].

In addition, because the density of the nucleus is saturated, the number of nucleons is proportional to the volume, textbooks such as [11] state that the number of nucleons A is used as

$$R \sim 1.2 \times A^{1/3} \tag{H.2}$$

In fact, in the left figure of Figure H.1, each measurement point appears to be on a straight line. The equation obtained by fitting these points with a straight line is

$$R = 1.103 \times A^{1/3} + 0.640 \equiv R_0(A) \tag{H.3}$$

and the R obtained using this equation is defined as $R_0(A)$.

H.2 Extension of the charge radius database to the neutron-rich region

Equation (H.3) holds well for stable nuclei, but the more unstable the nuclei are from the stable line, the more likely they are to deviate from $R_0(A)$. Figure H.2 shows the charge radius data [68] near Ti plotted for each isotope, overlaid with equation (H.3).

Now, let us evaluate the distance from the stability line and the deviation of the

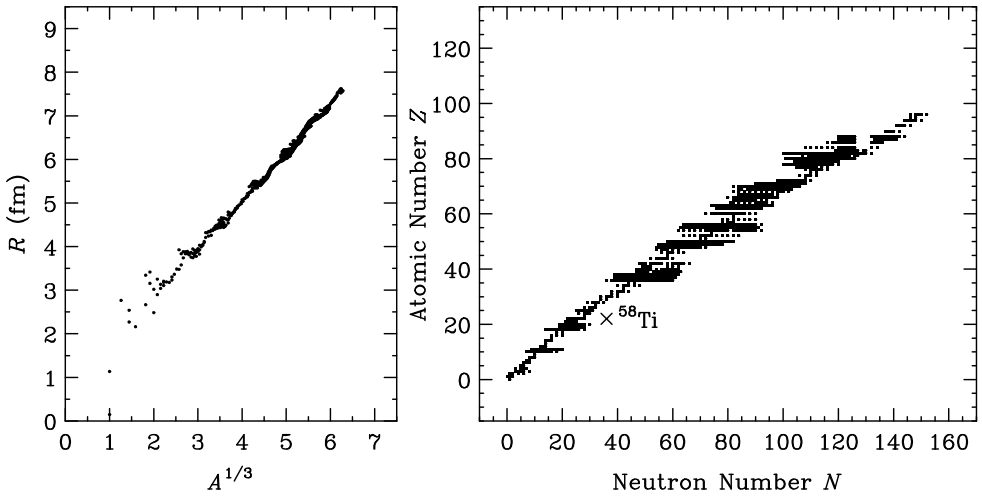

Figure H.1: Left: The experimental data for the mean square charge radius published in "The table of experimental nuclear charge radii" was converted to a uniform density distribution radius using the formula (H.1), and plotted with $A^{1/3}$ as the horizontal axis. The relational equation (H.3) obtained by fitting this distribution with a straight line is shown in the figure. Right: A list of the nuclides used as data points in the figure on the left. There is no radius data for ^{58}Ti, which is the focus of this study.

nuclear radius from $R_0(A)$.

If the most stable number of neutrons in a certain isotope is $N_s(Z)$, the distance from the stability line can be expressed as the difference in the number of neutrons from the stability line :

$$\Delta N \equiv N - N_s(Z) \tag{H.4}$$

Similarly, the deviation of the nuclear radius from $R_0(A)$ is defined as :

$$\Delta R \equiv R - R_0(A) \tag{H.5}$$

Here, to find $N_s(Z)$, we use a method to find the isobar with the smallest mass derived from the Weizsäcker-Bethe mass formula. The Weizsäcker-Bethe mass formula is a semi-empirical formula that reproduces the mass obtained by experiment, and is expressed as follows:

$$\begin{aligned} Mc^2 = (NM_n + ZM_p)c^2 - a_v A + a_s A^{2/3} + a_c Z^2 A^{-1/3} \\ + a_a (N-Z)^2 A^{-1} + \delta \end{aligned} \tag{H.6}$$

Here, the subscripted a has a specific value determined by experiment.

Next, to obtain the lightest (= most stable) isobar, the number of nucleons A is kept constant and we calculate :

$$\left.\frac{\partial M}{\partial Z}\right|_{A=\text{const}} = 0 \tag{H.7}$$

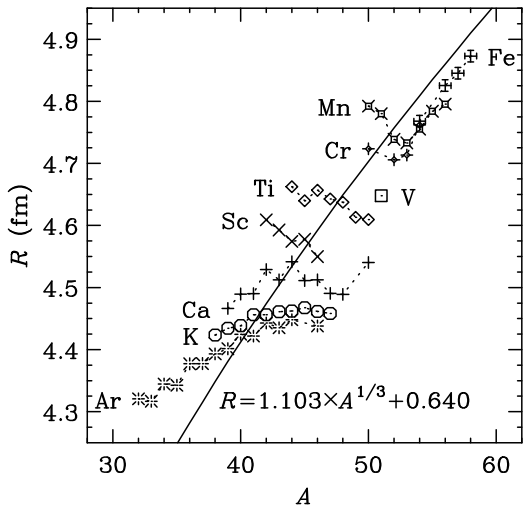

Figure H.2: Nuclear radius data near Ti. Looking at each isotope, the relationship in formula (H.3) does not hold, and on the neutron-rich side the values tend to be smaller than those in formula (H.3).

Of course, here $A = Z + N$. By substituting the numerical values, we obtain the most stable number of protons Z when the number of nucleons is A, i.e.,

$$Z_s(A) = \frac{A}{2.00 + 0.015A^{2/3}} \tag{H.8}$$

By calculating this relationship numerically using a computer, the most stable number of neutrons $N_s(Z)$ can be obtained.

This can be used to calculate ΔN, and the distribution of ΔN correlated with ΔR obtained from the nuclear radius database and the formula (H.3) is shown as small black circles in Figure H.3.

If we approximate this distribution with a linear line and extrapolate to find R for ^{56}Ti and ^{58}Ti, and call this $R_1(^AZ)$, we get:

$$R_1(^{56}\mathrm{Ti}) = 4.69(12)\ [\mathrm{fm}] \tag{H.9}$$

$$R_1(^{58}\mathrm{Ti}) = 4.70(15)\ [\mathrm{fm}] \tag{H.10}$$

H.3 Prediction using Ca nuclear material radii after $N = 28$

The nuclear radii of ^{56}Ti and ^{58}Ti obtained in the previous subsection were both predicted to be smaller than R_0. Here is an example of a prediction that can obtain a nuclear radius larger than R_0 using a different method. In a study of neutron skin in Ca isotopes, it has been reported that the nuclear material radius increases sharply after $N = 28$ [69]. The results of this research are overlaid with the charge radius database [68] and the formula (H.3) in Figure H.4.

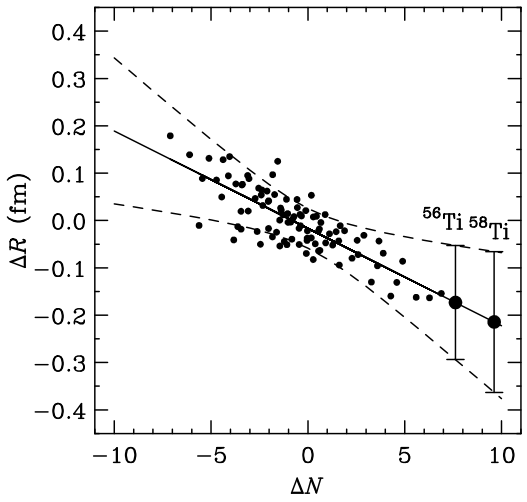

Figure H.3: The relationship between ΔN and ΔR in the range $Z = 12$ to 32 around the Ti isotope $Z = 22$.

The most stable neutron number $N_s(\mathrm{Ca})$ of Ca calculated from formula (H.8) is 23.7, but it has been shown that in the range of $N < 28$, including around that number, both the nuclear material radius and the charge radius are almost constant at $R \sim 4.5$ [fm].

Therefore, when N is larger than $N_s(\mathrm{Ca})$, the measured value is smaller than R_0 (shown by the dashed line in the figure) obtained from formula (H.3). On the other hand, in the range of $N > 28$, as is the subject of this paper, the nuclear material radius increases rapidly, exceeding R_0 at $N = 31$. Here, it is explained that $N = 28$ is the neutron magic number, and this increase occurs as the nuclear structure changes when there are more neutrons than that.

Ca and Ti are likely to show similar properties, with only a difference of two protons Z. To quantify the behavior of the nuclear matter radius of Ca after $N > 28$, fitting was performed with

$$R = p_0(N - 29.5) + p_1 \tag{H.11}$$

This is shown by the solid line in the figure. The reason for using $(N - 29.5)$ is to set the center of the four points as the reference position for the offset, so that the error in p_0 can be correctly estimated.

We will use this tendency to predict the nuclear radii of ^{56}Ti and ^{58}Ti. For Ca, the nuclear matter radius and the charge radius are roughly the same size in the range of $N < 28$, so we assume the same for Ti. By coincidence, the nuclear radii for Ti published in [68] are up to $N = 28$, so we extrapolated the unmeasured region beyond $N = 28$ by assuming that it increases with the same slope as the fitted result

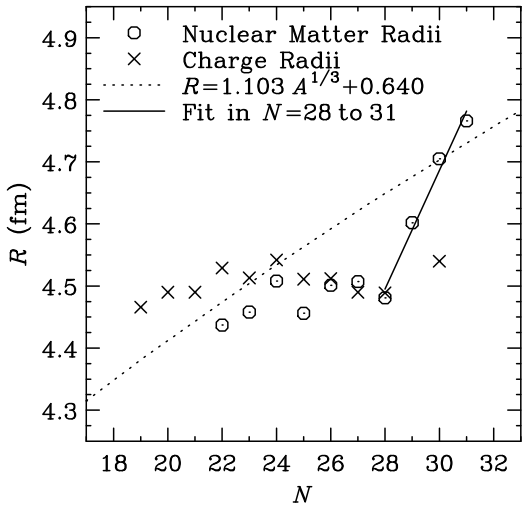

Figure H.4: Ca nuclear matter radius

for Ca. This is shown in Figure H.5. In addition, the nuclear radii of ^{56}Ti and ^{58}Ti obtained by this extrapolation are defined as R_2,

$$R_2(^{56}\mathrm{Ti}) = 5.18(12)\ [\mathrm{fm}] \tag{H.12}$$

$$R_2(^{58}\mathrm{Ti}) = 5.38(15)\ [\mathrm{fm}] \tag{H.13}$$

Finally, we have predicted the nuclear radii R_1 and R_2 using two different methods. Considering that both are possible, we determine the center value and error of the nuclear radius to cover both error ranges.

$$R(^{56}\mathrm{Ti}) = 4.94(37)\ [\mathrm{fm}] \tag{H.14}$$

$$R(^{58}\mathrm{Ti}) = 5.04(49)\ [\mathrm{fm}] \tag{H.15}$$

This is used as the nuclear radius of ^{56}Ti and ^{58}Ti in this paper for subsequent calculations.

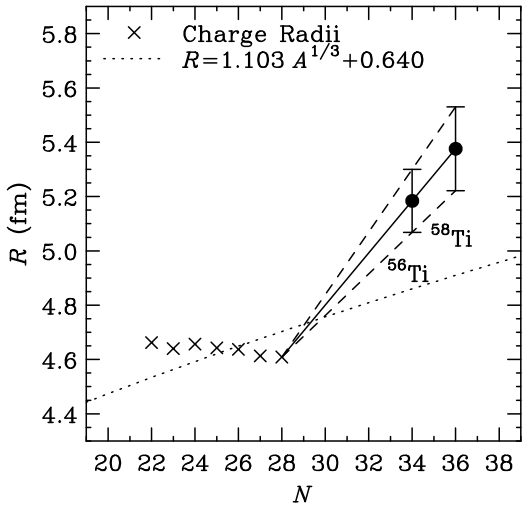

Figure H.5: Radius of Ti nucleus

References

[1] T. Motobayashi, Y. Ikeda, K. Ieki, M. Inoue, N. Iwasa, T. Kikuchi, M. Kurokawa, S. Moriya, S. Ogawa, H. Murakami, S. Shimoura, Y. Yanagisawa, T. Nakamura, Y. Watanabe, M. Ishihara, T. Teranishi, H. Okuno, R. Casten, Large deformation of the very neutron-rich nucleus ^{32}Mg from intermediate-energy Coulomb excitation, Physics Letters B 346 (1-2) (1995) 9–14.
URL https://doi.org/10.1016/0370-2693(95)00012-A

[2] A. Ozawa, T. Kobayashi, T. Suzuki, K. Yoshida, I. Tanihata, New Magic Number, $N = 16$, near the Neutron Drip Line, Phys. Rev. Lett. 84 (2000) 5493–5495.
URL https://doi.org/10.1103/PhysRevLett.84.5493

[3] S. Chen, J. Lee, P. Doornenbal, A. Obertelli, C. Barbieri, Y. Chazono, P. Navrátil, K. Ogata, T. Otsuka, F. Raimondi, V. Somà, Y. Utsuno, K. Yoshida, H. Baba, F. Browne, D. Calvet, F. Château, N. Chiga, A. Corsi, M. L. Cortés, A. Delbart, J.-M. Gheller, A. Giganon, A. Gillibert, C. Hilaire, T. Isobe, J. Kahlbow, T. Kobayashi, Y. Kubota, V. Lapoux, H. N. Liu, T. Motobayashi, I. Murray, H. Otsu, V. Panin, N. Paul, W. Rodriguez, H. Sakurai, M. Sasano, D. Steppenbeck, L. Stuhl, Y. L. Sun, Y. Togano, T. Uesaka, K. Wimmer, K. Yoneda, N. Achouri, O. Aktas, T. Aumann, L. X. Chung, F. Flavigny, S. Franchoo, I. Gašparić, R.-B. Gerst, J. Gibelin, K. I. Hahn, D. Kim, T. Koiwai, Y. Kondo, P. Koseoglou, C. Lehr, B. D. Linh, T. Lokotko, M. MacCormick, K. Moschner, T. Nakamura, S. Y. Park, D. Rossi, E. Sahin, D. Sohler, P.-A. Söderström, S. Takeuchi, H. Törnqvist, V. Vaquero, V. Wagner, S. Wang, V. Werner, X. Xu, H. Yamada, D. Yan, Z. Yang, M. Yasuda, L. Zanetti, Quasifree Neutron Knockout from ^{54}Ca Corroborates Arising $N = 34$ Neutron Magic Number, Phys. Rev. Lett. 123 (2019) 142501.
URL https://doi.org/10.1103/PhysRevLett.123.142501

[4] T. Otsuka, T. Suzuki, R. Fujimoto, H. Grawe, Y. Akaishi, Evolution of Nuclear Shells due to the Tensor Force, Phys. Rev. Lett. 95 (2005) 232502.
URL https://doi.org/10.1103/PhysRevLett.95.232502

[5] M. G. Mayer, On Closed Shells in Nuclei, Phys. Rev. 74 (1948) 235–239.
URL https://doi.org/10.1103/PhysRev.74.235

[6] M. G. Mayer, On Closed Shells in Nuclei. II, Phys. Rev. 75 (1949) 1969–1970.
URL https://doi.org/10.1103/PhysRev.75.1969

[7] M. G. Mayer, Nuclear Configurations in the Spin-Orbit Coupling Model. I. Empirical Evidence, Phys. Rev. 78 (1950) 16–21.
URL https://doi.org/10.1103/PhysRev.78.16

[8] M. G. Mayer, Nuclear Configurations in the Spin-Orbit Coupling Model. II. Theoretical Considerations, Phys. Rev. 78 (1950) 22–23.
URL https://doi.org/10.1103/PhysRev.78.22

[9] O. Haxel, J. H. D. Jensen, H. E. Suess, On the "Magic Numbers" in Nuclear Structure, Phys. Rev. 75 (1949) 1766–1766.
URL https://doi.org/10.1103/PhysRev.75.1766.2

[10] M. Mayer, J. Jensen, Elementary Theory of Nuclear Shell Structure, Structure of matter series, John-Wiley and Sons, Inc., New York, 1955.

[11] 杉本健三, 村岡光男, 原子核物理学, 共立出版, 1988.

[12] Y. Avishai, First 0^+ Excited State of ^{16}O in the α-Particle Model of Light Nuclei, Phys. Rev. C 6 (1972) 677–679.
URL https://doi.org/10.1103/PhysRevC.6.677

[13] B. Sørensen, Static quadrupole moment of the collective octupole vibration in ^{208}Pb, Physics Letters B 35 (2) (1971) 101–104.
URL https://doi.org/10.1016/0370-2693(71)90229-2

[14] M. Bernas, P. Dessagne, M. Langevin, J. Payet, F. Pougheon, P. Roussel, Magic features of ^{68}Ni, Physics Letters B 113 (4) (1982) 279–282.
URL https://doi.org/10.1016/0370-2693(82)90039-9

[15] R. Lombard, D. Mas, Shell effects at Z or $N = 40$: The example of ^{68}Ni, Physics Letters B 120 (1) (1983) 23–26.
URL https://doi.org/10.1016/0370-2693(83)90614-7

[16] R. Broda, B. Fornal, W. Królas, T. Pawlat, D. Bazzacco, S. Lunardi, C. Rossi-Alvarez, R. Menegazzo, G. de Angelis, P. Bednarczyk, J. Rico, D. De Acuña, P. J. Daly, R. H. Mayer, M. Sferrazza, H. Grawe, K. H. Maier, R. Schubart, $N = 40$ Neutron Subshell Closure in the ^{68}Ni Nucleus, Phys. Rev. Lett. 74 (1995) 868–871.
URL https://doi.org/10.1103/PhysRevLett.74.868

[17] R. Grzywacz, R. Béraud, C. Borcea, A. Emsallem, M. Glogowski, H. Grawe, D. Guillemaud-Mueller, M. Hjorth-Jensen, M. Houry, M. Lewitowicz, A. C. Mueller, A. Nowak, A. Płochocki, M. Pfützner, K. Rykaczewski, M. G. Saint-Laurent, J. E. Sauvestre, M. Schaefer, O. Sorlin, J. Szerypo, W. Trinder, S. Viteritti, J. Winfield, New Island of μs Isomers in Neutron-Rich Nuclei around the $Z = 28$ and $N = 40$ Shell Closures, Phys. Rev. Lett. 81 (1998) 766–769.
URL https://doi.org/10.1103/PhysRevLett.81.766

[18] W. F. Mueller, B. Bruyneel, S. Franchoo, M. Huyse, J. Kurpeta, K. Kruglov, Y. Kudryavtsev, N. V. S. V. Prasad, R. Raabe, I. Reusen, P. Van Duppen, J. Van Roosbroeck, L. Vermeeren, L. Weissman, Z. Janas, M. Karny, T. Kszczot, A. Płochocki, K.-L. Kratz, B. Pfeiffer, H. Grawe, U. Köster, P. Thirolf, W. B. Walters, β decay of ^{66}Co, ^{68}Co, and ^{70}Co, Phys. Rev. C 61 (2000) 054308.
URL https://doi.org/10.1103/PhysRevC.61.054308

[19] T. Ishii, M. Asai, A. Makishima, I. Hossain, P. Kleinheinz, M. Ogawa, M. Matsuda, S. Ichikawa, Gamma-ray spectroscopy of the neutron-rich Ni region through heavy-ion deep-inelastic collisions , Eur. Phys. J. A 13 (1) (2002).
URL https://doi.org/10.1140/epja1339-04

[20] L. Ekström, J. Lyttkens-Linden, Nuclear data sheets for $A = 90$, Nuclear Data Sheets 67 (4) (1992) 579–691.
URL https://doi.org/10.1016/0090-3752(92)80027-H

[21] National Nuclear Data Center.
URL https://www.nndc.bnl.gov/

[22] D.-C. Dinca, R. V. F. Janssens, A. Gade, D. Bazin, R. Broda, B. A. Brown, C. M. Campbell, M. P. Carpenter, P. Chowdhury, J. M. Cook, A. N. Deacon, B. Fornal, S. J. Freeman, T. Glasmacher, M. Honma, F. G. Kondev, J.-L. Lecouey, S. N. Liddick, P. F. Mantica, W. F. Mueller, H. Olliver, T. Otsuka, J. R. Terry, B. A. Tomlin, K. Yoneda, Reduced transition probabilities to the first 2^+ state in ^{52,54,56}Ti and development of shell closures at $N = 32, 34$, Phys.

Rev. C 71 (2005) 041302.
URL https://doi.org/10.1103/PhysRevC.71.041302

[23] H. Suzuki, N. Aoi, E. Takeshita, S. Takeuchi, S. Ota, H. Baba, S. Bishop, T. Fukui, Y. Hashimoto, E. Ideguchi, K. Ieki, N. Imai, M. Ishihara, H. Iwasaki, S. Kanno, Y. Kondo, T. Kubo, K. Kurita, K. Kusaka, T. Minemura, T. Motobayashi, T. Nakabayashi, T. Nakamura, T. Nakao, M. Niikura, T. Okumura, T. K. Ohnishi, H. J. Ong, H. Sakurai, S. Shimoura, R. Sugo, D. Suzuki, M. K. Suzuki, M. Tamaki, K. Tanaka, Y. Togano, K. Yamada, Collectivity of neutron-rich Ti isotopes, Physical Review C 88 (2) (2013) 024326.
URL https://doi.org/10.1103/PhysRevC.88.024326

[24] M. Honma, T. Otsuka, B. A. Brown, T. Mizusaki, New effective interaction for pf-shell nuclei and its implications for the stability of the $N = Z = 28$ closed core, Phys. Rev. C 69 (2004) 034335.
URL https://doi.org/10.1103/PhysRevC.69.034335

[25] M. Honma, T. Otsuka, B. Brown, T. Mizusaki, Shell-model description of neutron-rich pf-shell nuclei with a new effective interaction GXPF 1, The European Physical Journal A-Hadrons and Nuclei 25 (2005) 499–502.
URL https://doi.org/10.1140/epjad/i2005-06-032-2

[26] Y. Tsunoda, T. Otsuka, N. Shimizu, M. Honma, Y. Utsuno, Novel shape evolution in exotic Ni isotopes and configuration-dependent shell structure, Physical Review C 89 (3) (2014) 031301.
URL https://doi.org/10.1103/PhysRevC.89.031301

[27] M. Honma, et al., unpublished.

[28] N. Shimizu, T. Abe, Y. Tsunoda, Y. Utsuno, T. Yoshida, T. Mizusaki, M. Honma, T. Otsuka, New-generation Monte Carlo shell model for the K computer era, Progress of Theoretical and Experimental Physics 2012 (1) (2012) 01A205.
URL https://doi.org/10.1093/ptep/pts012

[29] K. Yoshida, Skyrme-QRPA calculations for low-lying excitation modes in deformed neutron-rich nuclei, The European Physical Journal A 42 (3) (2009) 583–590.
URL https://doi.org/10.1140/epja/i2008-10742-y

[30] K. Washiyama, N. Hinohara, T. Nakatsukasa, Five-dimensional collective Hamiltonian with improved inertial functions, Phys. Rev. C 109 (2024) L051301.
URL https://doi.org/10.1103/PhysRevC.109.L051301

[31] T. K. Alexander, J. S. Forster, Lifetime Measurements of Excited Nuclear Levels by Doppler-Shift Methods, Springer US, Boston, MA, 1978, pp. 197–331.
URL https://doi.org/10.1007/978-1-4757-4401-9_3

[32] N. Fukuda, T. Kubo, T. Ohnishi, N. Inabe, H. Takeda, D. Kameda, H. Suzuki, Identification and separation of radioactive isotope beams by the BigRIPS separator at the RIKEN RI Beam Factory, Nuclear Instruments and Methods in Physics Research Section B: Beam Interactions with Materials and Atoms 317 (2013) 323–332.
URL https://doi.org/10.1016/j.nimb.2013.08.048

[33] H. Kumagai, T. Ohnishi, N. Fukuda, H. Takeda, D. Kameda, N. Inabe, K. Yoshida, T. Kubo, Development of Parallel Plate Avalanche Counter (PPAC) for BigRIPS fragment separator, Nuclear Instruments and Methods in Physics Research Section B: Beam Interactions with Materials and Atoms 317 (2013) 717–727.
URL https://doi.org/10.1016/j.nimb.2013.08.050

[34] P. Carnelli, S. Almaraz-Calderon, K. Rehm, M. Albers, M. Alcorta, P. Bertone, B. Digiovine, H. Esbensen, J. Fernández Niello, D. Henderson, C. Jiang, J. Lai, S. Marley, O. Nusair, T. Palchan-Hazan, R. Pardo, M. Paul, C. Ugalde, Multi-Sampling Ionization Chamber (MUSIC) for measurements of fusion reactions with radioactive beams, Nuclear Instruments and Methods in Physics Research Section A: Accelerators, Spectrometers, Detectors and Associated Equipment 799 (2015) 197–202.
URL https://doi.org/10.1016/j.nima.2015.07.030

[35] K. Kimura, T. Izumikawa, R. Koyama, T. Ohnishi, T. Ohtsubo, A. Ozawa, W. Shinozaki, T. Suzuki, M. Takahashi, I. Tanihata, T. Yamaguchi, Y. Yamaguchi, High-rate particle identification of high-energy heavy ions using a tilted electrode gas ionization chamber, Nuclear Instruments and Methods in Physics Research Section A: Accelerators, Spectrometers, Detectors and Associated Equipment 538 (1) (2005) 608–614.
URL https://doi.org/10.1016/j.nima.2004.08.100

[36] K. Wimmer, P. Doornenbal, N. Aoi, H. Baba, F. Browne, C. Campbell, H. Crawford, H. D. Witte, C. Fransen, H. Hess, S. Iwazaki, J. Kim, A. Kohda, T. Koiwai, B. Mauss, B. Moon, T. Parry, P. Reiter, D. Suzuki, R. Taniuchi, S. Thiel, Y. Yamamoto, HiCARI: High-resolution Cluster Array at RIBF, RIKEN Accelerator Progress Report 54 (2021) S27.
URL https://www.nishina.riken.jp/researcher/APR/APR054/pdf/RIKEN_APR54.pdf#page=49

[37] A. Kohda, Y. Yamamoto, N. Aoi, E. Ideguchi, M. K. Raju, H. T. Hoang, T. T. Pham, T. Shima, S. Miyamoto, T. Shizuma, N. Imai, J. W. Hwang, K. Wimmer, P. Doornenbal, M. L. Cortes, HiCARI: High-resolution Cluster Array at RIBF, CNS Annual Report 2018 (2020) 47.
URL https://www.cns.s.u-tokyo.ac.jp/archive/annual/ann18.pdf#page=65

[38] N. Warr, J. Van de Walle, M. Albers, F. Ames, B. Bastin, C. Bauer, V. Bildstein, A. Blazhev, S. Bönig, N. Bree, B. Bruyneel, P. A. Butler, J. Cederkäll, E. Clément, T. E. Cocolios, T. Davinson, H. De Witte, P. Delahaye, D. D. DiJulio, J. Diriken, J. Eberth, A. Ekström, J. Elseviers, S. Emhofer, D. V. Fedorov, V. N. Fedosseev, S. Franchoo, C. Fransen, L. P. Gaffney, J. Gerl, G. Georgiev, R. Gernhäuser, T. Grahn, D. Habs, H. Hess, A. M. Hurst, M. Huyse, O. Ivanov, J. Iwanicki, D. G. Jenkins, J. Jolie, N. Kesteloot, O. Kester, U. Köster, M. Krauth, T. Kröll, R. Krücken, M. Lauer, J. Leske, K. P. Lieb, R. Lutter, L. Maier, B. A. Marsh, D. Mücher, M. Münch, O. Niedermaier, J. Pakarinen, M. Pantea, G. Pascovici, N. Patronis, D. Pauwels, A. Petts, N. Pietralla, R. Raabe, E. Rapisarda, P. Reiter, A. Richter, O. Schaile, M. Scheck, H. Scheit, G. Schrieder, D. Schwalm, M. Seidlitz, M. Seliverstov, T. Sieber, H. Simon, K.-H. Speidel, C. Stahl, I. Stefanescu, P. G. Thirolf, H.-G. Thomas, M. Thürauf, P. Van Duppen, D. Voulot, R. Wadsworth, G. Walter, D. Weißhaar, F. Wenander, A. Wiens, K. Wimmer, B. H. Wolf, P. J. Woods, K. Wrzosek-Lipska, K. O. Zell, The Miniball spectrometer, The European Physical Journal A 49 (3) (2013) 40.
URL https://doi.org/10.1140/epja/i2013-13040-9

[39] G. Duchêne, F. Beck, P. Twin, G. de France, D. Curien, L. Han, C. Beausang, M. Bentley, P. Nolan, J. Simpson, The Clover: a new generation of composite Ge detectors, Nuclear Instruments and Methods in Physics Research Section A: Accelerators, Spectrometers, Detectors and Associated Equipment 432 (1)

(1999) 90–110.
URL https://doi.org/10.1016/S0168-9002(99)00277-6

[40] I. Y. Lee, Gamma-ray tracking detectors, Nuclear Instruments and Methods in Physics Research Section A: Accelerators, Spectrometers, Detectors and Associated Equipment 422 (1) (1999) 195–200.
URL https://doi.org/10.1016/S0168-9002(98)01093-6

[41] S. Takeuchi, T. Motobayashi, Y. Togano, M. Matsushita, N. Aoi, K. Demichi, H. Hasegawa, H. Murakami, DALI2: A NaI(Tl) detector array for measurements of γ rays from fast nuclei, Nuclear Instruments and Methods in Physics Research Section A: Accelerators, Spectrometers, Detectors and Associated Equipment 763 (2014) 596–603.
URL https://doi.org/10.1016/j.nima.2014.06.087

[42] P. Reiter, N. Warr, Nuclear structure studies with re-accelerated beams at REX-and HIE-ISOLDE, Progress in Particle and Nuclear Physics 113 (2020) 103767.
URL https://doi.org/10.1016/j.ppnp.2020.103767

[43] P.M. Jones and L. Wei and F.A. Beck and P.A. Butler and T. Byrski and G. Duchêne and G. de France and F. Hannachi and G.D. Jones and B. Kharraja, Calibration of the new composite "clover" detector as a Compton polarimeter for the EUROGAM array, Nuclear Instruments and Methods in Physics Research Section A: Accelerators, Spectrometers, Detectors and Associated Equipment 362 (2) (1995) 556–560.
URL https://doi.org/10.1016/0168-9002(95)00246-4

[44] S. Paschalis, I. Lee, A. Macchiavelli, C. Campbell, M. Cromaz, S. Gros, J. Pavan, J. Qian, R. Clark, H. Crawford, D. Doering, P. Fallon, C. Lionberger, T. Loew, M. Petri, T. Stezelberger, S. Zimmermann, D. Radford, K. Lagergren, D. Weisshaar, R. Winkler, T. Glasmacher, J. Anderson, C. Beausang, The performance of the Gamma-Ray Energy Tracking In-beam Nuclear Array GRETINA, Nuclear Instruments and Methods in Physics Research Section A: Accelerators, Spectrometers, Detectors and Associated Equipment 709 (2013) 44–55.
URL https://doi.org/10.1016/j.nima.2013.01.009

[45] RIBFDAQ.
URL https://ribf.riken.jp/RIBFDAQ/

[46] H. Baba, S. Takeuchi, K. Yamada, Y. Sakamoto, K. Ieki, S. Shimoura, Present status of data acquisition system ‘ BabarlDAQ ’ for nuclear physics experiments, RIKEN Accelerator Progress Report 37 (2004) 187.
URL https://www.nishina.riken.jp/researcher/APR/Document/ProgressReport_vol_37.pdf#page=195

[47] H. Baba, T. Ichihara, T. Ohnishi, S. Takeuchi, K. Yoshida, Y. Watanabe, S. Ota, S. Shimoura, The new DAQ system in RIKEN RIBF, in: 2008 IEEE Nuclear Science Symposium Conference Record, 2008, pp. 1384–1386.
URL https://doi.org/10.1109/NSSMIC.2008.4774674

[48] H. Baba, T. Ichihara, T. Ohnishi, S. Takeuchi, K. Yoshida, Y. Watanabe, S. Ota, S. Shimoura, New data acquisition system for the RIKEN Radioactive Isotope Beam Factory, Nuclear Instruments and Methods in Physics Research Section A: Accelerators, Spectrometers, Detectors and Associated Equipment 616 (1) (2010) 65–68.
URL https://doi.org/10.1016/j.nima.2010.02.120

[49] H. Baba, T. Ichihara, T. Isobe, C. Houarner, C. Maugeais, B. Raine, F. Saillant, G. Wittwer, N. Kurz, H. Schaffner, R. Gernhäuser, S. Anvar, D. Calvet, F. Château, E. Pollacco, DAQ coupling in RIKEN RIBF, in: 2014 19th IEEE-NPSS Real Time Conference, 2014, pp. 1–5.
URL https://doi.org/10.1109/RTC.2014.7097436

[50] J. T. Anderson, M. Albers, M. Alcorta, C. Campbell, M. P. Carpenter, C. J. Chiara, M. Cromaz, H. M. David, D. Doering, D. T. Doherty, C. R. Hoffman, R. V. F. Janssens, J. Joseph, T. L. Khoo, A. Kreps, T. Lauritsen, I. Y. Lee, C. Lionberger, C. J. Lister, T. Madden, M. B. Oberling, A. M. Rogers, D. Seweryniak, P. Wilt, S. Zhu, S. Zimmermann, A digital data acquisition system for the detectors at gammasphere, in: 2012 IEEE Nuclear Science Symposium and Medical Imaging Conference Record (NSS/MIC), 2012, pp. 1536–1540.
URL https://doi.org/10.1109/NSSMIC.2012.6551368

[51] M. Cromaz, V. Riot, P. Fallon, S. Gros, B. Holmes, I. Lee, A. Macchiavelli, C. Vu, H. Yaver, S. Zimmermann, A digital signal processing module for gamma-ray tracking detectors, Nuclear Instruments and Methods in Physics Research Section A: Accelerators, Spectrometers, Detectors and Associated Equipment 597 (2) (2008) 233–237.
URL https://doi.org/10.1016/j.nima.2008.07.137

[52] H. Baba, F. Browne, P. Doornenbal, B. Mauss, B. Moon, D. Suzuki, N. Aoi, S. Iwazaki, A. Kohda, Y. Yamamoto, T. Koiwai, R. Taniuchi, K. Wimmer, for the HiCARI Collaboration, Computer server and network for HiCARI experiments, RIKEN Accelerator Progress Report 54 (2021) 102.
URL https://www.nishina.riken.jp/researcher/APR/APR054/pdf/RIKEN_APR54.pdf#page=178

[53] J. T. Anderson, Multi-purpose γ-Ray Interface to Auxiliary Detectors (MyRIAD) User Manual (2015).
URL https://doi.org/10.2172/1177968

[54] Sources – SUNFLOWER Collaboration website.
URL https://www.nishina.riken.jp/collaboration/SUNFLOWER/misc/util/sources.php

[55] S. Agostinelli, J. Allison, K. Amako, J. Apostolakis, H. Araujo, P. Arce, M. Asai, D. Axen, S. Banerjee, G. Barrand, F. Behner, L. Bellagamba, J. Boudreau, L. Broglia, A. Brunengo, H. Burkhardt, S. Chauvie, J. Chuma, R. Chytracek, G. Cooperman, G. Cosmo, P. Degtyarenko, A. Dell'Acqua, G. Depaola, D. Dietrich, R. Enami, A. Feliciello, C. Ferguson, H. Fesefeldt, G. Folger, F. Foppiano, A. Forti, S. Garelli, S. Giani, R. Giannitrapani, D. Gibin, J. Gómez Cadenas, I. González, G. Gracia Abril, G. Greeniaus, W. Greiner, V. Grichine, A. Grossheim, S. Guatelli, P. Gumplinger, R. Hamatsu, K. Hashimoto, H. Hasui, A. Heikkinen, A. Howard, V. Ivanchenko, A. Johnson, F. Jones, J. Kallenbach, N. Kanaya, M. Kawabata, Y. Kawabata, M. Kawaguti, S. Kelner, P. Kent, A. Kimura, T. Kodama, R. Kokoulin, M. Kossov, H. Kurashige, E. Lamanna, T. Lampén, V. Lara, V. Lefebure, F. Lei, M. Liendl, W. Lockman, F. Longo, S. Magni, M. Maire, E. Medernach, K. Minamimoto, P. Mora de Freitas, Y. Morita, K. Murakami, M. Nagamatu, R. Nartallo, P. Nieminen, T. Nishimura, K. Ohtsubo, M. Okamura, S. O'Neale, Y. Oohata, K. Paech, J. Perl, A. Pfeiffer, M. Pia, F. Ranjard, A. Rybin, S. Sadilov, E. Di Salvo, G. Santin, T. Sasaki, N. Savvas, Y. Sawada, S. Scherer, S. Sei, V. Sirotenko, D. Smith, N. Starkov, H. Stoecker, J. Sulkimo, M. Takahata, S. Tanaka, E. Tcherniaev, E. Safai Tehrani, M. Tropeano, P. Truscott, H. Uno, L. Urban, P. Urban, M. Verderi, A. Walkden, W. Wander, H. Weber, J. Wellisch, T. Wenaus, D. Williams, D. Wright, T. Yamada, H. Yoshida, D. Zschiesche, Geant4—a simulation toolkit, Nuclear Instruments and Methods in Physics Research Section A: Accelerators, Spectrometers, Detectors and Associated

Equipment 506 (3) (2003) 250–303.
URL https://doi.org/10.1016/S0168-9002(03)01368-8

[56] L. Riley, D. Weisshaar, H. Crawford, M. Agiorgousis, C. Campbell, M. Cromaz, P. Fallon, A. Gade, S. Gregory, E. Haldeman, L. Jarvis, E. Lawson-John, B. Roberts, B. Sadler, C. Stine, UCGretina geant4 simulation of the GRETINA Gamma-Ray Energy Tracking Array, Nuclear Instruments and Methods in Physics Research Section A: Accelerators, Spectrometers, Detectors and Associated Equipment 1003 (2021) 165305.
URL https://doi.org/10.1016/j.nima.2021.165305

[57] D. Weisshaar, D. Bazin, P. Bender, C. Campbell, F. Recchia, V. Bader, T. Baugher, J. Belarge, M. Carpenter, H. Crawford, M. Cromaz, B. Elman, P. Fallon, A. Forney, A. Gade, J. Harker, N. Kobayashi, C. Langer, T. Lauritsen, I. Lee, A. Lemasson, B. Longfellow, E. Lunderberg, A. Macchiavelli, K. Miki, S. Momiyama, S. Noji, D. Radford, M. Scott, J. Sethi, S. Stroberg, C. Sullivan, R. Titus, A. Wiens, S. Williams, K. Wimmer, S. Zhu, The performance of the γ -ray tracking array GRETINA for γ -ray spectroscopy with fast beams of rare isotopes, Nuclear Instruments and Methods in Physics Research Section A: Accelerators, Spectrometers, Detectors and Associated Equipment 847 (2017) 187–198.
URL https://doi.org/10.1016/j.nima.2016.12.001

[58] O. Tarasov, D. Bazin, LISE++: Radioactive beam production with in-flight separators, Nuclear Instruments and Methods in Physics Research Section B: Beam Interactions with Materials and Atoms 266 (19) (2008) 4657–4664.
URL https://doi.org/10.1016/j.nimb.2008.05.110

[59] I. J. Thompson, Coupled reaction channels calculations in nuclear physics, Computer Physics Reports 7 (4) (1988) 167–212.
URL https://doi.org/10.1016/0167-7977(88)90005-6

[60] I. Thompson, Fresco.
URL https://www.fresco.org.uk/

[61] 八木浩輔, 原子核物理学, 朝倉書店, 1971.

[62] C. A. Bertulani, A. Sustich, Multipole response of ^{11}Li, Phys. Rev. C 46 (1992) 2340–2343.
URL https://doi.org/10.1103/PhysRevC.46.2340

[63] C. A. Bertulani, G. Baur, Electromagnetic processes in relativistic heavy ion collisions, Physics Reports 163 (5) (1988) 299–408.
URL https://doi.org/10.1016/0370-1573(88)90142-1

[64] H. Morinaga, T. Yamazaki, In-beam gamma-ray spectroscopy, North-Holland, Netherlands, 1976.

[65] A. Winther, K. Alder, Relativistic coulomb excitation, Nuclear Physics A 319 (3) (1979) 518–532.
URL https://doi.org/10.1016/0375-9474(79)90528-1

[66] K. Wimmer, Coulex.
URL https://github.com/wimmer-k/Coulex

[67] A. メシア, メシア量子力学 3, 東京図書, 1972.

[68] I. Angeli, K. Marinova, Table of experimental nuclear ground state charge radii: An update, Atomic Data and Nuclear Data Tables 99 (1) (2013) 69–95.
URL https://doi.org/10.1016/j.adt.2011.12.006

[69] M. Tanaka, M. Takechi, A. Homma, M. Fukuda, D. Nishimura, T. Suzuki, Y. Tanaka, T. Moriguchi, D. S. Ahn, A. Aimaganbetov, M. Amano, H. Arakawa, S. Bagchi, K.-H. Behr, N. Burtebayev, K. Chikaato, H. Du, S. Ebata, T. Fujii, N. Fukuda, H. Geissel, T. Hori, W. Horiuchi, S. Hoshino, R. Igosawa, A. Ikeda, N. Inabe, K. Inomata, K. Itahashi, T. Izumikawa, D. Kamioka, N. Kanda, I. Kato, I. Kenzhina, Z. Korkulu, Y. Kuk, K. Kusaka, K. Matsuta, M. Mihara, E. Miyata, D. Nagae, S. Nakamura, M. Nassurlla, K. Nishimuro, K. Nishizuka, K. Ohnishi, M. Ohtake, T. Ohtsubo, S. Omika, H. J. Ong, A. Ozawa, A. Prochazka, H. Sakurai, C. Scheidenberger, Y. Shimizu, T. Sugihara, T. Sumikama, H. Suzuki, S. Suzuki, H. Takeda, Y. K. Tanaka, I. Tanihata, T. Wada, K. Wakayama, S. Yagi, T. Yamaguchi, R. Yanagihara, Y. Yanagisawa, K. Yoshida, T. K. Zholdybayev, Swelling of Doubly Magic ^{48}Ca Core in Ca Isotopes beyond $N = 28$, Phys. Rev. Lett. 124 (2020) 102501.
URL https://doi.org/10.1103/PhysRevLett.124.102501

謝辞 (Acknowledgments)

本研究を遂行するにあたり、多くの方々よりご指導、ご助言、ご支援を賜りました。ここに深く感謝の意を表します。

まず初めに、指導教員である青井考教授には、研究テーマの選定から実験計画の立案、データ解析に至るまで、多大なるご指導と温かいご支援を賜りました。教授の的確な助言と非常に厳しいご指導は、本研究を進める上で大きな支えとなりました。修士課程から数えて八年以上にわたりご指導いただいたことに、心より御礼申し上げます。

次に、井手口栄治准教授、Kathrin Wimmer 博士、山本康嵩博士には、実験の準備や測定、データ整理、さらに得られた成果の解釈に至るまで、研究遂行に関わるあらゆる面で多大なご協力をいただきました。ここに厚く御礼申し上げます。

さらに、理研での実験においてご協力いただいた Pieter Doornenbal 博士、鈴木大介博士、小岩井拓真博士、岩崎聖子さん、馬場秀忠博士、Frank Browne 博士、Jiseok Kim さん、小池武志准教授、Benoit Mauss 博士、水野るり惠博士、Byul Moon 博士、新倉潤博士、Thanh Tung Pham 博士、櫻井博儀教授、谷内稜博士、ならびに加速器・検出器を運用してくださったスタッフの皆様には、実験の遂行に関する技術的支援とご尽力を賜りました。深く感謝申し上げます。

また、合計五回にわたる再審査にお付き合いいただいた五人委員の民井淳教授、野海博之教授、吉田賢市准教授、そして最終審査において主査をお引き受けくださった川畑貴裕教授には、厳しくも建設的なご助言と温かい励ましを賜りました。ここに厚く御礼申し上げます。

さらに、研究面のみならず日常のあらゆる相談に乗っていただいた核物理研究センター博士後期課程の同期である森田泰之君、須藤高志君、また研究室でのお茶会仲間である坂口治隆さん、古野達也さん、井上梓さん、村田求基さん、遠藤史隆君、Zhang Ji Chao さんには、日々の交流を通じて心の支えとなっていただきました。ここに感謝の意を表します。

最後に、日常生活において常に支えてくれた家族や友人に心から感謝いたします。皆様の温かな支えがあったからこそ、本研究を最後までやり遂げることができました。

改めまして、本研究にご協力いただいたすべての方々に深甚なる感謝を申し上げます。